Spring 2004

Experimental Investigation of a Rubidium-Argon Dual Species Magneto-Optical Trap

Hauke Christian Busch
Old Dominion University

EXPERIMENTAL INVESTIGATION OF A RUBIDIUM-ARGON DUAL SPECIES MAGNETO-OPTICAL TRAP

by

Hauke Christian Busch
M.S. May 2001, Old Dominion University
Ph.D. May 1994, University of Colorado at Boulder
M.S. May 1991, University of Colorado at Boulder
B.S. May 1990, Gonzaga University

A Thesis Submitted to the Faculty of
Old Dominion University in Partial Fulfillment of the
Requirement for the Degree of

DOCTOR OF PHILOSOPHY

PHYSICS

OLD DOMINION UNIVERSITY
May 2004

Approved by:

Charles I. Sukenik (Director)

Kenneth G. Brown (Member)

Mark D. Havey (Member)

Charles E. Hyde-Wright (Member)

Colm T. Whelan (Member)

ABSTRACT

EXPERIMENTAL INVESTIGATION OF A RUBIDIUM-ARGON DUAL SPECIES MAGNETO-OPTICAL TRAP

Hauke Christian Busch
Old Dominion University, 2004
Director: Dr. Charles I. Sukenik

The first simultaneous cooling and confinement of two different atomic species from opposite sides of the periodic table in a dual magneto optical trap (DMOT) has been accomplished. The alkali-metal ^{85}Rb and the noble gas ^{40}Ar* have been simultaneously confined, characterized, and interspecies interaction parameters have been measured. The DMOT confined $1.2\text{x}10^{6}$ ^{85}Rb atoms at a density of $1\text{x}10^{10}/\text{cm}^3$ and $1.4\text{x}10^{6}$ ^{40}Ar* atoms with a density of $1.2\text{x}10^{10}/\text{cm}^3$. A collisional loss rate coefficient for Rb-Ar* has been determined to be $\gamma_{Rb-Ar} = (4.8 \pm 1.6)\text{x}10^{-11}\text{cm}^3/\text{s}$. A typical reduction of 3% of the florescence of the trapped ^{85}Rb was observed when the ^{40}Ar* trap was present. The loss of atoms from the dual trap is presumed to be caused by radiative escape and ionization losses, for an ^{40}Ar* MOT it is due to Penning and associative ionization losses. An Ar* PI/AI ionization ratio of 6.7±3.6 was determined, which makes the Penning ionization rate the dominant loss mechanism. The ionization rate was obtained with a SRS RGA200 mass spectrum analyzer specifically modified to work in conjunction with an ion optical field plate setup to collect the ions expelled from the MOT. The ^{85}Rb was trapped with a 780 nm diode laser while the ^{40}Ar* was slowed and trapped with a 811 nm Ti:sapphire laser, which was specifically modified to be locked to within 1 MHz of the atomic transition with a linewidth of ~1 MHz. The metastable state ^{40}Ar* was produced with a rf driven resonating cavity discharge which produced an atomic beam with an

angular flux density of $4x10^{14}$ atoms $s^{-1}sr^{-1}$.

This thesis is dedicated to my wife
Jacqueline
and our son
Christian Fletcher.

ACKNOWLEDGMENTS

The research and writing of this thesis has profited from the support of a number of people. I am especially grateful to Charles Sukenik for providing admirable guidance and support through my graduate career. It is no exaggeration to say he has been an exceptional mentor to me. He has made excellent suggestions for additions and revisions, which have significantly improved this thesis.

In additional to Charles Sukenik I would also like to acknowledge and thank my committee members: Kenneth Brown, Mark Havey, Charles Hyde-Wright, and Colm Whelan for lending their expertise and review. I am also in debt to Mark Havey for his initial guidance into Atomic Physics.

Finally, I would like to express my gratitude to my wife Jacqueline for making the necessary sacrifices to help me through graduate school.

TABLE OF CONTENTS

Page

LIST OF TABLES

LIST OF FIGURES

CHAPTER I

INTRODUCTION

The advent of the Magneto Optical Trap (MOT) by Raab et al [1], has allowed for the confinement and study of atomic samples at temperatures never before obtained. This simple confinement of just one species has now grown into a new field of physics with numerous applications beyond physics such as chemistry, biology and medicine [2-4]. In general there are two types of experiments conducted on traps, one that is purely scientific in nature, and one that has direct practical applications.

Studies centered around scientific applications have focused initially on cooling a single species to ultracold temperatures (< 1 mK), trapping it, and then characterizing its collision properties inside a MOT [5]. The next phase evolved into the photoassociation of an atomic sample into diatomic molecules from trapped atoms [6], to the study of parity violation of a sample of atoms confined in a MOT [7, 8], and to cooling a sample of trapped atoms into a Bose-Einstein condensate [9-11]. During these new developments it became apparent that to attain Bose-Einstein condensates or degenerate Fermi Gases sometimes multiple cooling techniques had to be employed, one of them being sympathetic or evaporative cooling. Sympathetic cooling uses either two distinct species of atoms simultaneously confined in a MOT or a mixture of the same atom at two different internal states. The two different atoms are then in thermal contact with each other allowing one atom to cool the other, in this manner an atomic species, which could

---

This thesis conforms to the format of Physical Review Letters.

not easily be cooled to Bose-Einstein condensate temperatures using optical methods before, was now able to be cooled into a Bose-Einstein condensate or degenerate Fermi Gas [5]. Furthermore, the study of diatomic molecular photoassociation moved from homonuclear to that of heteronuclear molecular interactions. The homonuclear dimer consisted of the alkali-metal atoms group, while the heteronuclear dimer was a blend of two alkali-metal atoms [12-16]. The study of an atomic sample from different groups of the periodic table, or namely the production of a heteronuclear dimer of an alkali-metal and a noble gas has not yet been done [17].

On the more direct practical applications side, research focuses on using atom traps to: build more precise atomic clocks [18-19], perform atomic lithography [20], build the atom laser [21], perfect atomic optics, and create additional new innovations [22]. One of the most novel innovations relevant to atomic physics will most likely be the development of the quantum computer. It is believed that a 1-D trap loaded with ultracold polar diatomic molecules, where the molecular dipole moment is used as a computational bit, can possibly be the first operational quantum computer. For the realization of the quantum computer to take place, the production of ultracold molecules from dual species traps has to be mastered. Due to the rate-limiting Frank-Condon factor the formation of ultra cold heteronuclear type species seems to be more favorable than homo-nuclear species [23]. While homonuclear dual-alkali type traps have been built and studied there is limited experimental information available on interspecies heteronuclear interactions.

This thesis focuses on the first simultaneous confinement of the alkali-metal ^{85}Rb and metastable noble gas ^{40}Ar atoms in a MOT at ultracold temperatures. Since little

information is available on the ultra cold collisional interaction of these species, this work will set the first baseline for the interaction parameters. Those parameters are of fundamental importance since they set the starting point for future work in photoassociative spectroscopy of the RbAr* complex (* designates the atom is in a metastable state, the metastable state is considered the temporary ground state of the atom for trapping purposes), of molecule production, and that of a Bose-Einstein condensate. Photoassociative spectroscopy uses additional laser light, to that of the trap laser beams, to form bound molecular states from two ground state atoms. This technique should yield information yet unknown about the RbAr* long range complex such as molecular energy levels and the coupling between different molecular states, short range van der Waals ($V(R) \sim C_6/R^6$) metastable ground state potentials, and ionization properties. This type of information would be necessary to determine the suitability of the alkali-noble gas heteronuclear molecule for quantum computation and theoretical verification for unknown potential curves and collisional parameters.

1.1 BACKGROUND

Laser spectroscopic investigations of alkali-noble gas van der Waals molecules have already been carried out in thermal beams and in cells [24-33]. Through these investigations, improvements in laser sources have lead to an increase in accuracy in high-resolution molecular spectroscopy. With the application of Doppler-free techniques and higher light intensity lasers, molecular structures like hyperfine splitting and weak molecular transitions could now be resolved with higher accuracy. This improvement in

experimental techniques helped to correlate exciting theoretical work in alkali and alkali-noble gas systems [34-40].

The development of the MOT in the mid 1980's made it possible to cool and confine a sample of atomic vapor into the ultra cold regime. With decreasing temperature, the collisional times between two atoms started to exceed the excited state-lifetimes, thus allowing for energy transfer between atoms and multiple photons during an encounter. Furthermore, the de Broglie wavelength increases with decreasing temperature and becomes comparable to the length of the atom-atom interaction distance and the wavelength of trap cooling light. In addition, the spectral Doppler width is almost zero at average MOT operating temperatures. The MOT represented the starting point to produce quantum degenerate gases and the formation of ultracold molecules. Applications and motivations of initial research on the formation of cold molecules were spectroscopy, manipulation of molecules, cold collisions, nucleation and metastability, Bose-Einstein condensation of molecules, degenerate Fermi gases of molecules, and the molecular laser [41, 42].

Ultracold molecules are produced in a MOT from a sample of cold atoms, which approach each other, usually on a ground state potential. The atoms will then absorb a photon, from an external laser source, and couple into an excited bound molecular state. This process is known as photoassociation, Fig.1.1. If the molecular product is a molecular ion then it is called photoassociative ionization. If the two atoms approaching each other are homonuclear then an excited state resonant dipole-dipole ($V(R) \sim C_3/R^3$) interaction results (Note: This is for a S-P collision, if a S-S collision takes place this would be a van der Waals interaction and for P-P collision this results into a quadrupole-

quadrupole interaction). On the other hand, if both atoms are heteronuclear then they will couple into a short range van der Waals molecule ($V(R) \sim C_6/R^6$). Having different potentials, homonuclear and heteronuclear interactions also differ in their molecular properties. Homonuclear alkali-metal dimers like Li_2, Na_2, K_2, Rb_2, and Cs_2 have successfully been photoassociated and studied. Some heteronuclear alkali molecules have also been formed such as KRb and RbCs, and the $NaCs^+$ and $RbCs^+$ ions. As for the noble gas side, photoassociative spectra have only been observed in He*. Metastable noble gas atoms differ from alkali systems in that they have an initially large amount of internal energy due to their metastable state and therefore have a larger probability to Penning ionize during photoassociative spectroscopy thereby yielding a large linewidth compared to that of the vibrational spacing of the molecule. A brief summary of the molecular work done with MOTs and their references is given in Table 1.1.

Theoretical work on ultracold collisions started with the Gallagher and Pritchard model, which proposed a simple, classic model that focused on fine-structure collisions and radiative escape trap loss [80]. Julienne and Vigué further expanded the model and added effects for more realistic molecular modeling [81]. Additional models were developed which eventually helped in the verification of experimental results in ultracold molecular production [82-86]. Several relevant theoretical references are listed in Table 1.1, denoted by theoretical. The following publications that are also listed in Table 1.1, are both experimental and theoretical: [49, 55, 59, 76]. To date no heteronuclear alkali-noble gas system theoretical work exists for highly excited states, thus giving no basis for comparative work or experimental verification.

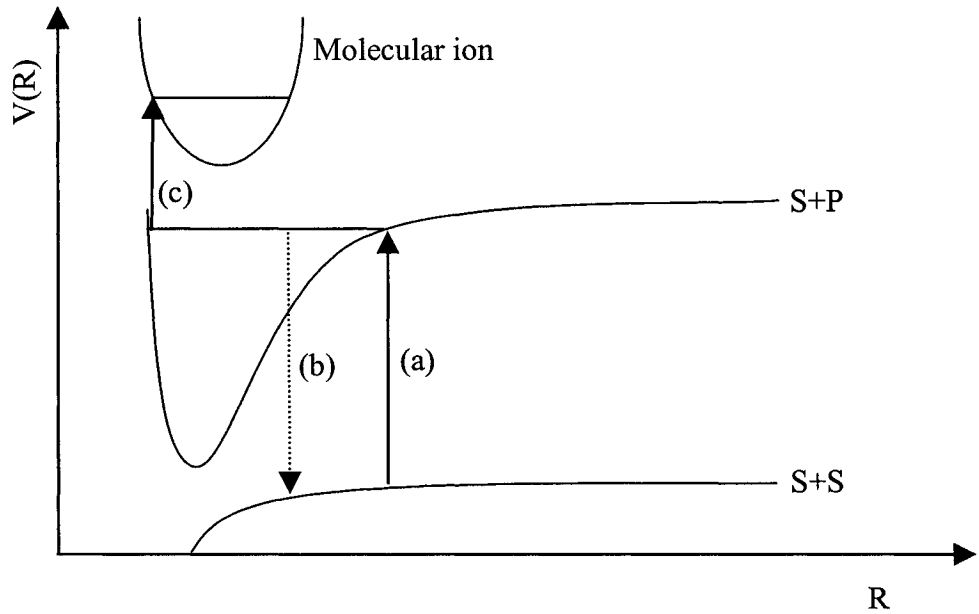

FIG. 1.1. Photoassociation of two ground state atoms into a molecule during a collision in the S+S state. A photon (a) is absorbed and the atoms couple into an excited bound molecular state, S+P. The spontaneous emission of a photon (b) back to ground state is possible; the kinetic energy released during this incidence is a source of trap loss. The absorption of a second photon (c) can lead to photoassociative ionization.

TABLE 1.1. Summary of ultracold molecules produced by photoionization in a MOT.

Molecule produced	Reference	Notes
H_2	[43]	Ultra cold but not in MOT, spin polarized sample
Li_2	[44, 45]	s-wave scattering length, radiative lifetime
	[46, 47]	Long-range states $^6Li_2$, $^7Li_2$/ heteronuclear $^6Li_2$, $^7Li_2$
	[87-89]	Theoretical $^7Li_2$
Na_2	[48, 49]	Associative Ionization Ultra cold hybrid trap
	[50-57]	Lifetime & retardation inter. Hyperfine effects
	[90, 91]	Theoretical
K_2	[58-64]	Hunds case (a) and (c) also radiative lifetime
Rb_2	[65-70]	(FORT)
	[71, 72]	Two color photoassociative ionization
	[92]	Theoretical
Cs_2	[73-76]	Photoassociation and Spectroscopy
Ca_2	[77]	Photoassociation of first alkaline earth
KRb	[78]	Heteronuclear diatomic molecules
	[86]	Theoretical (also Rb-Cs, K-Cs, Rb-Na)
$NaCs^+$	[16]	Heteronuclear photoassociative ionization
RbCs	[93]	Polar molecules via photoassociation
$RbCs^+$	[94]	Mixed Rb/Cs MOT and photoassociation
$He(2^3S)$	[80]	Noble gas photoassociation spectroscopy

It was proposed that ultracold molecules can also be formed from cold atoms, which are cooled down into a Bose-Einstein condensate, and then coherently converted into molecules [95-98]. The possibility of attaining Bose-Einstein condensation and degenerate Fermi Gases has led to more work being done on dual-species traps. To produce these quantum degenerate gases it is sometimes necessary to use sympathetic cooling, which requires that more than one species be confined simultaneously in the trap. Due to the Pauli exclusion principle elastic collisions are absent during ultracold temperatures ($T \rightarrow 0$). Elastic collisions are those in which the quantum state of the atoms does not change and are generally considered as good collisions, while inelastic collisions cause the quantum state of the atoms to change, resulting in heating the atoms and causing trap loss. It is therefore necessary to have as large a ratio of elastic to inelastic collisions as possible for sympathetic cooling to be effective. Because of that it is essential to know the collisional loss rate parameters of the two interacting species. Therefore, the majority of the initial experiments focused on determining collisional loss rate constants for interspecies interactions and quantifying trap interspecies parameters, such as dual species trap densities and the number of atoms confined. The first experiments of dual species traps were initially conducted with two different isotopes of the same alkali-metal atom. Experiments then expanded to include different dual alkali-metal atomic combinations.

Due to the difficulty in building dual species traps, and the added complexity of trapping a noble gas, no dual alkali-noble gas trap has been built prior to this work. In addition, there is no theoretical work available to guide experimentation. This thesis will represent a baseline of the first alkali-noble gas trap interaction parameters. The main

scope of this thesis is the determination of the first dual alkali-noble (^{85}Rb-^{40}Ar*) gas collisional loss rate constants and baseline trap parameters. A summary of dual species traps and their references is given in Table 1.2.

1.2 THE ULTRACOLD RbAr MOLECULE

The long-term goal of this work is to produce ground state RbAr molecules at ultracold temperatures, Fig. 1.2. Several possible approaches can be pursued for molecule production. The scheme most likely to be successful is to photoassociate atoms in the MOT into RbAr molecules. The photoassociation channel consists of exciting colliding Rb and Ar* atoms in the MOT into Rydberg states which decay to ground state molecules. The molecules once formed will be confined in a far off resonance trap (FORT) for further study.

The majority of work in ultracold physics has been done primarily on atoms. The production of the RbAr molecule would set the groundwork for ultracold heteronuclear molecular physics. Photoassociative spectroscopy of molecules will allow for the probing of free-bound transitions with high resolution in determining the energy levels and dissociation energies of excited and ground state molecules. Photoassociative spectroscopy will also allow for investigating states, which are not accessible by conventional spectroscopy, and for isolating effects due to hyperfine structure. The physical information gained from those experiments can then be used for comparison with molecular structure calculations for long-range molecules and to determine s-wave scattering lengths. The s-wave scattering length is of importance for calculating elastic

TABLE 1.2. Summary of dual-species MOTs built and their applications.

Dual species	Reference	Application
^{7}Li-^{6}Li	[106, 107]	Bose Condensate immersed in a Fermi Sea
(Boson-Fermion)	[109, 110]	Step toward quantum degenerate gases, sympathetic
Li-Cs	[108]	Optical traps for quantum gases
^{133}Cs-^{7}Li	[116-118]	Sympathetic cooling, trap characterization
^{23}Na-^{6}Li	[105]	Quantum degenerate Bose and Fermi Gases
Na-Li	[115]	Sympathetic cooling, trap characterization
Na-K	[120, 121]	Trap characterization, hyperfine changing collisions
Na-^{87}Rb & Na-^{85}Rb	[122, 123]	Trap characterization, hyperfine changing collisions
Na-Cs	[124]	Trap characterization
^{40}K-^{87}Rb	[100, 125]	Fermi-Bose quantum gases, Trap characterization
^{41}K-^{87}Rb	[101-103]	Superfluid, Collapse of a Degenerate Fermi gas
^{39}K-^{85}Rb, K-Rb	[119, 126]	Trap characterization, all isotopic trap characterize
^{87}Rb | F=1, m=-1>-	[104]	Two overlapping Bose-Einstein Condensate
^{87}Rb | F=2, m=2>		Sympathetic cooling
^{84}Rb-^{87}Rb	[111]	Step toward sympathetic cooling Fermi-Boson
^{85}Rb-^{87}Rb	[112, 113]	Sympathetic cooling, trap characterization
^{85}Rb-^{40}Ar	[17, this	Trap characterization, can lead to alternate noble gas
	work]	BEC and RbAr* molecule production
^{85}Rb-^{133}Cs, ^{87}Rb-^{133}Cs	[127]	Trap characterization
^{172}Yb, ^{174}Yb, ^{176}Yb,	[99]	(FORT) Fermion-boson mixture
^{171}Yb, ^{173}Yb	[114]	Simultaneous trapping & characterization

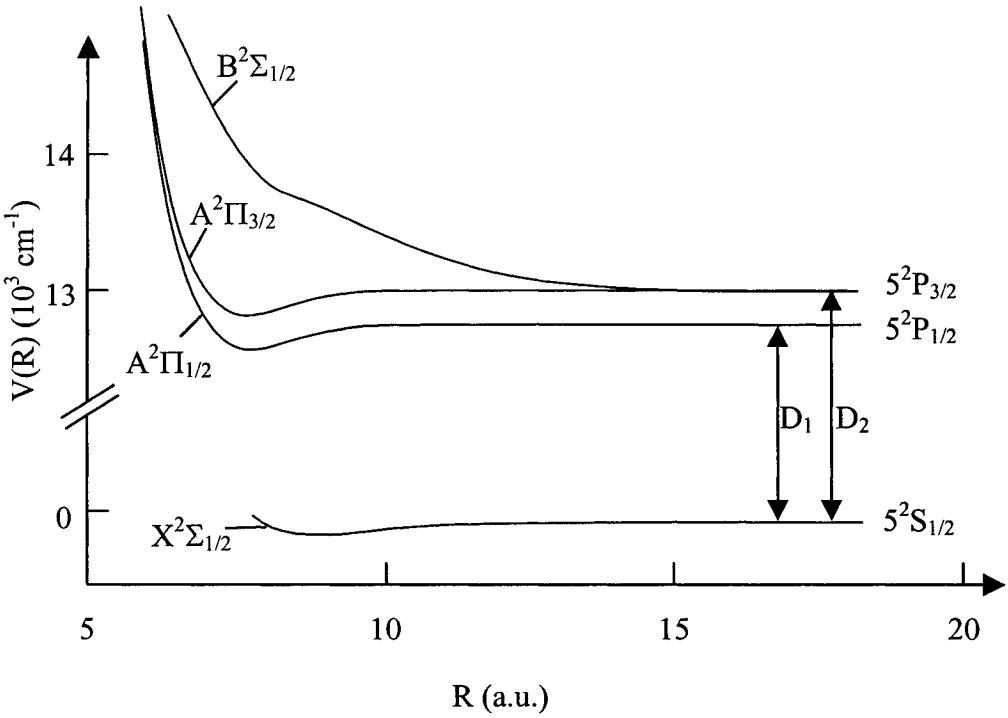

FIG. 1.2. Schematic of the lowest potential curves of the RbAr molecule [128].

scattering rates in evaporative cooling, which leads to Bose-Einstein condensates. What's more, the information gathered can be used for the determination of the accuracy of frequency standards for atomic clocks, to determine radiative lifetimes with high precision, to study predissociation, the resonant energy transfer between ultracold Rydberg atoms, and to observe Feshbach resonances.

Before studying ground state RbAr, studies of excited state "quasi-molecules" of (RbAr)*, formed during collisions in the MOT will be performed. The first experiments planned with the RbAr molecules are to study the physics of

1.) Interactions of unlike atoms (Rb and Ar*) at ultracold temperatures.

2.) Heteronuclear ionization processes, ionization potential, and interactions in general at ultracold temperatures. (This should yield surprising results since our preliminary results suggest low ionization rates.)

3.) Assessing the feasibility of ultracold molecular production.

4.) Exploring collision dynamics and determining molecular structure of the excited states- which is presently unknown.

The initial experiments are designed to focus on understanding the physics of ultracold molecular production, but this could eventually lead into a tool for future physical studies and other important applications. Ultracold molecular production could further research in ultra-high resolution spectroscopy, molecular collision dynamics, atom-molecule and molecule-ion interactions, precision measurements of fundamental symmetries, molecular optics, and novel molecular beam production.

Quantum computation is a possible application of ultracold heteronuclear molecules formed in a MOT. Current computers are expected to reach their maximum performance by the year 2020; the next possible advent in technology could be the quantum computer. Quantum computers have the ability to perform calculations with exponentially fewer steps than present day computers, resulting in a probable speed increase over present day computer systems. It has been proposed by DeMille [23] that a 1-D trap could hold individual molecules with the aid of an electric field gradient that would allow the spectroscopic addressing of each site. Loading the 1-D trap with ultracold molecules allows for a weak trapping potential and should result in long

decoherence times for the system. Each site would contain a diatomic molecule, whose electric dipole moment is oriented along or against an external electric field, which is considered its qubit. Bits would be coupled via the electric dipole-dipole interaction [23]. A MOT would be an excellent starting point in creating ultracold diatomic molecules by photoassociation. Previous research focused on creating bi-alkali molecules as was shown in Table 1.1. The production of ultracold heteronuclear molecules are considered more favorable for the quantum computer since there is a better match between their ground- and excited-state potential curves. Until now only homonuclear alkali systems have been considered, as they are thought to be the most experimentally convenient to build. With the building of the dual alkali-noble gas MOT the possibility of a RbAr molecule can now be considered. The ultracold heteronuclear RbAr molecule confined in a FORT could be suitable candidate for such an application.

Another possible physics application of the RbAr molecule might be the study of parity violation effects. Kozlov et. al. [129] proposed that the magnitudes of the possible space parity as well as the nonconservation of both space and time-reversal effects could be observed in diatomic van der Waals molecules. In diatomic heteronuclear molecules the space and space, time –odd electron-nucleon interaction mixes the rotational levels belonging to the same electronic term; those effects would be four to five times stronger than that in atoms. A suitable van der Waals molecule to study parity violations was suggested to be of the CsXe type. Those molecules have an unpaired electron and have been more experimentally accessible. This type of molecule has been formed during supersonic expansion of a noble gas containing a small mixture of alkali-metal atoms. The molecule is formed during the adiabatic cooling process. This type of production of

the CsXe molecule raises the question of the magnitude of the parity violation effects in a van der Waals molecule. The production of the ultracold RbAr van der Waals molecule would give the first opportunity to study parity violation in a MOT/FORT system setup. The MOT could again be used to photoassociate the RbAr molecules, which then would be confined in a FORT for further study. The FORT possesses the ability to confine these molecules in the ground state at translational and rotational temperatures of several mK or less, thus making it possible for further research into fundamental symmetries in nature.

CHAPTER II

THEORETICAL BACKGROUND

The ability to simultaneously cool two atomic species, from opposite sides of the periodic table, and confine them at ultracold temperatures, requires several experimental innovations and the understanding of some basic physical concepts. Thanks to the development of the laser and the invention of the magneto-optical trap (MOT) it is possible to trap and cool an alkali-metal and a noble gas atom simultaneously [2-4]. The MOT uses a combination of magnetic field gradients and circularly polarized counter propagating laser light to cool and trap neutral atoms. This type of trap makes it ideal to trap both ^{85}Rb and ^{40}Ar* (*=metastable atom) simultaneously [130]. Furthermore, since the trapping of ^{40}Ar* atoms requires a Zeeman slower to decelerate them so that they can be captured by the MOT, the same theoretical physical principle which apply to a MOT can also be used for a Zeeman slower.

2.1 THE PRINCIPLES OF LIGHT FORCES IN A MOT

The fundamental principle in laser cooling and trapping is that when a light beam scatters off an object an exchange of energy and momentum takes place creating a force upon it. There are two types of light forces that can act on an atom, the spontaneous force, sometimes also referred to as the radiation-pressure or scattering force, and the dipole force.

The spontaneous light force, responsible for cooling the atom, occurs when a photon of light is absorbed and subsequently emitted by an atom and a transfer of momentum takes place. With each photon the atom absorbs a quantum of momentum $\hbar\vec{k}$ is transferred to the atom in the direction of the photon (where $\hbar$ is the Plank constant and $\vec{k}$ is the wave vector of the photon). The emission of the photon from the atom takes place spontaneously and in a random direction. Over many absorption cycles the net emission force averages to zero. Therefore, the net force on the atom is from the direction of the absorbing photons [5]. The method of the spontaneous force is depicted in Fig. 2.1.

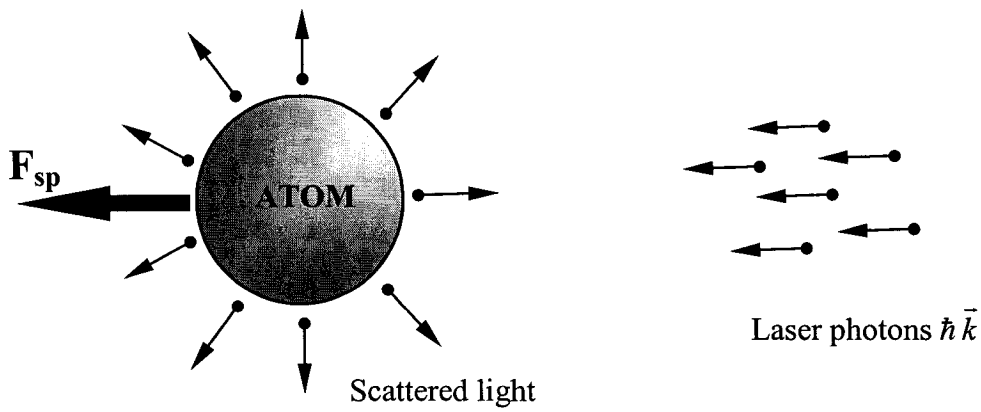

FIG. 2.1. Example of atom cooling with laser light. Laser light is coming from the right and is getting scattered off the atom. Since the scattered light's net momentum averages to zero, the net force on the atom is in the direction of the laser light.

The principle behind the spontaneous force, as used in laser cooling, is that the atom can only absorb a photon that is in resonance with an electronic transition within the atom. For this to take place the laser light has to be tuned to the right frequency of the

transition, but since atoms are generally not at rest, the frequency has to be Doppler shifted for the atom to see it. When the laser frequency is below the atomic resonance frequency the atom will scatter photons at a higher rate when moving toward the laser than when moving away from the laser. The spontaneous force is velocity dependent and is therefore dissipative in nature since it dissipates the kinetic energy of the atom. This is a requirement for it to be effective in cooling atoms. The velocity dependence relies solely on the red detuning of the laser light to match the Doppler shift of the atom to be cooled. When the atom is subjected to laser beams from all six directions the resulting motion of the atom is damped and the atom is thus cooled. This process is referred to as optical molasses. (For example: If an average saturated atom is traveling at 500 m/s it would be subjected to a 10^5 g force, bringing the atom to rest in half a millisecond over a distance of 13 cm.)

The second force is the dipole force. It is the result of the time averaged force caused from the interaction of the transition dipole, induced by the oscillating electric field of the laser light, with the gradient of the amplitude to the electric field [5]. The dipole force is responsible for trapping atoms and confining them, but to lowest order is conservative and does not provide cooling. Tuning the laser light below atomic resonance attracts the atom to the high intensity part of the light beam while tuning the laser light above resonance causes atoms to seek the low intensity region.

These two forces are significantly different; the spontaneous force is dissipative and velocity dependent and is used to cool atoms, while the dipole force is conservative and position dependent and can therefore be used to trap atoms [22]. By treating the atom as a two-level system and the radiation of the light field as a classical

electromagnetic field, a mathematical expression can be derived for the two forces. An interaction Hamiltonian of an atom in an electric field can then be written as

$$H = -\vec{\mu}_{eg} \cdot \vec{E}(\vec{r},t). \tag{2-1}$$

Where $\vec{\mu}_{eg}$ is the effective dipole moment for the two level atom transition, and $\vec{E}(\vec{r},t)$ is the electric field of the light. The force exerted on an atom is given by

$$\vec{F} = -\vec{\nabla}_r H = \vec{\nabla}_r(\vec{\mu}_{eg} \cdot \vec{E}(\vec{r},t)). \tag{2-2}$$

By assuming no spatial variation of the dipole moment and using the steady state solutions of the optical Bloch equations [Appendix A], the force can be separated into two terms. The first term, the dipole force, is proportional to the gradient of the electric field amplitude, while the second is proportional to the gradient of the phase and is called the spontaneous force [5, 131]. This can be written as

$$\vec{F} = \vec{F}_{dip} + \vec{F}_{sp}, \tag{2-3}$$

where

$$\vec{F}_{dip} = -\vec{\nabla}_r \left|\vec{E}_0\right| \frac{\hbar\Omega^2}{2}\left(\frac{\delta}{\delta^2 + (\Gamma/2)^2 + \Omega^2/2}\right), \tag{2-4}$$

and

$$\vec{F}_{sp} = \vec{\nabla}_r(\vec{k} \cdot \vec{r})\frac{\hbar\Omega^2}{2}\left(\frac{\Gamma/2}{\delta^2 + (\Gamma/2)^2 + \Omega^2/2}\right). \tag{2-5}$$

Here Γ is the natural line width of the atomic transition of the atom being cooled, and $\delta = \omega_{\text{Laser}} - \omega_{\text{Atom}}$ is the laser detuning from the atomic resonance frequency. The Rabi frequency Ω is defined by

$$\Omega = -\frac{\vec{\mu}_{eg} \cdot \vec{E}_0}{\hbar}. \tag{2-6}$$

The spontaneous force can be rewritten by first defining a saturation parameter as

$$s = \frac{\Omega^2/2}{\delta^2 + (\Gamma/2)^2} = \frac{s_0}{1 + (2\delta/\Gamma)^2}, \tag{2-7}$$

and an on resonance saturation parameter as

$$s_0 = \frac{2\Omega^2}{\Gamma^2} = \frac{I}{I_s}. \tag{2-8}$$

I is defined as the intensity of the laser light used, and I_s is the saturation intensity of the atom laser cooling transition used. Furthermore, we can define an excited state population ρ_{ee}, according to a two level system described by the optical Bloch equations as

$$\rho_{ee} = \frac{s}{2(1+s)}. \tag{2-9}$$

In the case of a low saturation parameter, $s \ll 1$, the atom's population is in the ground state, and in a large saturation parameter, $s \gg 1$, the population is evenly distributed between excited and ground state. The population in the excited state decays at a rate of Γ, and in a steady state the excitation and decay rates are equal, thus allowing us to define the total scattering rate Γ_p of an atom in a laser field as

$$\Gamma_p = \Gamma \rho_{ee}. \tag{2-10}$$

With this information the spontaneous force can now be rewritten as

$$\vec{F}_{sp} = \hbar \vec{k} \Gamma_p = \frac{\hbar \vec{k} \Gamma}{2} \frac{s_0}{1 + s_0 + (2\delta/\Gamma)^2}, \tag{2-11}$$

which is simply the momentum of a laser photon multiplied by the atom's scattering rate. The spontaneous force is sometimes also called the scattering force and is responsible for cooling atoms. In a high laser intensity regime this force saturates at $\vec{F}_{sp} = \hbar \vec{k} \Gamma/2$ [22,

132]. (For ^{85}Rb a laser intensity of >>1.6 mW/cm^2 the atom saturates and a spontaneous force of 1.5×10^{-20} N is exerted on it. Resulting in an acceleration of atom of 10^5 g.)

2.2 THE OPERATION OF A MAGNETO OPTICAL TRAP (MOT)

Since the spontaneous light force is dissipative and velocity dependent it can cool atoms but it cannot trap them, it is not a position dependent force. For the atoms to be contained in space, a varying magnetic field can be used in conjunction with the spontaneous light force to create a position dependent force for trapping atoms. To produce the position dependent force in a MOT a magnetic field gradient producing an inhomogeneous magnetic field of the form $B(z) = (\partial B/\partial z)z$ can be used (where $\partial B/\partial z$ is the magnetic field gradient in the z direction). The field gradient is produced by means of a set of anti-Helmholz coils that produces a magnetic quadrupole field in the MOT region. The MOT can then trap atoms by using three pairs of counterpropagating circularly-polarized laser beams, detuned to the red of the atomic cooling transition, intersecting orthogonally to each other where the magnetic field is zero.

The principle on which a MOT works can be visualized by again considering a two level atom $J_g=0 \rightarrow J_e=1$ moving one dimensionally. The inhomogeneous magnetic field Zeeman shifts the atomic sub levels causing a position dependent force on the atoms. The red detuned circular polarized laser light populates the respective Zeeman sub levels, σ^+-polarized beam can only populate the $m_e=+1$ level while the σ^--polarized beam populates the $m_e=-1$ level. Fig. 2.2 shows this schematically. As the atoms are moving toward the –z direction, the σ^+-polarized laser falls in resonance with the $m_e=+1$ atomic Zeeman sub level and subsequently scatters more photons of those atoms causing

a restoring force on the atom that then pushes it toward the center of the trap. The opposite case takes place for atoms moving toward the +z direction. Thus the magnetic field and detuned polarized laser light imposes a velocity and position dependent restoring force on the atoms, consequently trapping them [133].

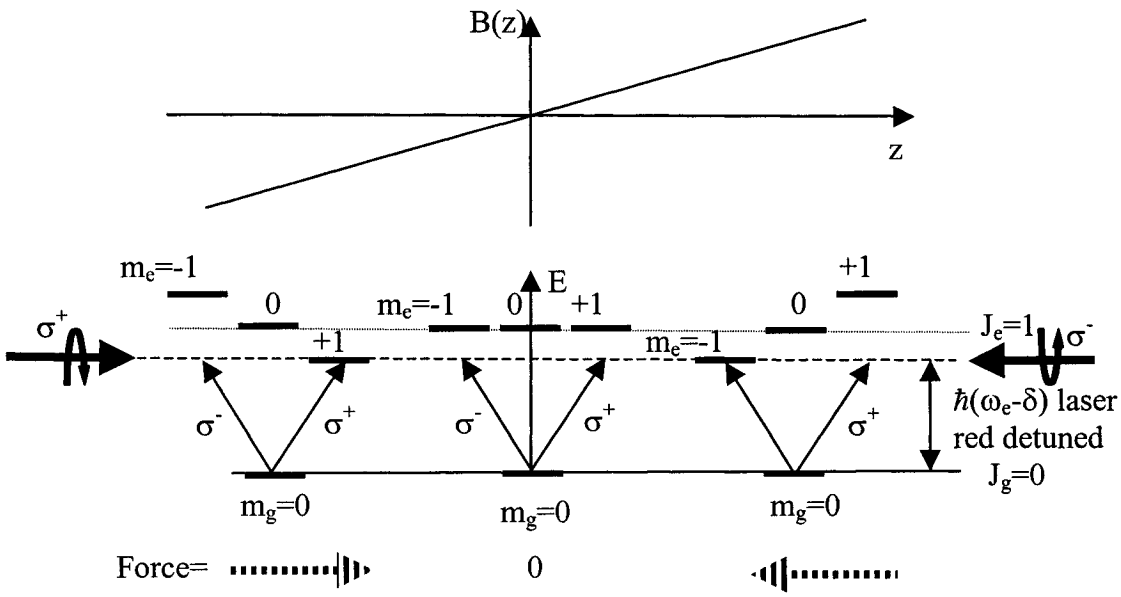

FIG. 2.2. Simplified schematic of the principles involved in the workings of a one dimensional MOT. As an atom moves toward the +z direction it falls into resonance with the σ^- laser light and gets pushed back into the center, while the opposite takes place when it moves toward the –z. The atom is cooled and confined near the center of the trap.

To define the motion of an atom in a MOT the expression for the spontaneous force Eq. (2-11) can be rewritten to read

$$\vec{F}_{\pm} = \frac{\hbar\vec{k}\Gamma}{2}\frac{s_0}{1+s_0+(2\delta_{\pm}/\Gamma)^2}, \tag{2-12}$$

where the total force on the atom is given by

$$\vec{F} = \vec{F}_{+} + \vec{F}_{-}, \tag{2-13}$$

and the detuning $\delta_{\pm}$ for each laser beam is given by

$$\delta_{\pm} = \delta \mp \vec{k}\cdot\vec{v} \pm \mu_{eg}B(z)/\hbar. \tag{2-14}$$

The Doppler shift that the atom experiences when it is in motion is $\omega_D = -\vec{k}\cdot\vec{v}$ and $\omega_z = \mu_{eg}B(z)/\hbar$ is the Zeeman shift as the atom moves away from the center of the trap. Near the center of the trap, where the velocity and the Zeeman shift of the atom is small with respect to the detuning, the total force on the atom $\vec{F}$, Eq. (2-13) with the substitutions of Eq. (2-12) can be expanded to give

$$\ddot{z} + \frac{\beta}{m}\dot{z} + \frac{\kappa}{m} = 0. \tag{2-15}$$

This is an equation of motion for a simple damped harmonic oscillator, where m is the mass of the atom, β is the damping constant and

$$\kappa = \frac{\mu_{eg}B_z}{\hbar k}\beta, \tag{2-16}$$

is the spring constant, which is dependent on the magnetic field gradient B_z of the trap. The MOT damping rate is given by $c_{MOT} = \beta/m$, and the oscillation frequency is $\omega_{MOT} = \sqrt{\kappa/m}$. The ratio of damped atomic motion over oscillation frequency is the characteristic restoring time $\tau_{res} = 2c_{MOT}/\omega_{MOT}^2$ of the MOT [22].

Since a real MOT is three-dimensional, six counterpropagating laser beams are required as well as a three-dimensional magnetic field, like the one produced by the

magnetic field gradients of an anti-Helmholz coil pair, Fig. 2.3. The magnetic quadrupole field gradients of the anti Helmholz coils are produced by two identical loops of wire that have current running through them in opposite directions. This generates a uniform magnetic field gradient along the coordinate axes with the magnetic field being zero at the center of symmetry of the coils. Along the MOT coil axis at the center of symmetry the magnetic field gradient in the z direction is defined as

$$B_z = \frac{\partial B}{\partial z} = \frac{3\mu_0 NIa^2 b}{2(a^2 + (b/2)^2)^{5/2}}. \qquad (2\text{-}17)$$

Where μ_0 is the permeability of free space, N is the number of coil windings, I is the current, a is the coils radius, and b is the separation between the two current loops, Fig. 2.3. The field gradients are fixed along each axis, but they do not have the same values. The field gradients in the horizontal xy plane are half that of the field gradient along the z-axis, $B_z = 2B_x = 2B_y$. As this is the case the spring constant along the z-axis is also twice as large as in the x and y direction, Eq. (2-16). This results in the restoring force in the z direction to be twice as large as in the xy plane causing the MOT to be anisotropic. (The magnetic field gradient B_z in our experimental setup has a typical value of $\approx$6.6 G/cm.)

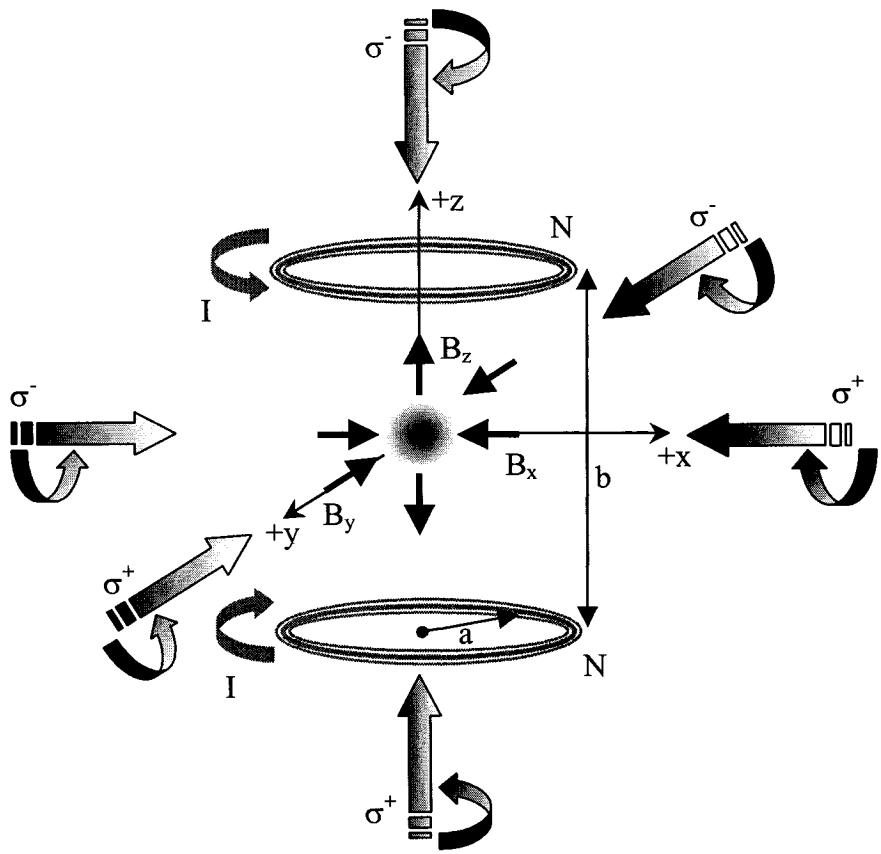

FIG. 2.3. A model of a three-dimensional MOT. The six circularly polarized counterpropagating laser beams intersecting at the center of the trap, and an anti-Helmholz coil pair producing the uniform quadrupole magnetic field gradients.

2.3 COOLING LIMITS AND IMPORTANT MOT PARAMETERS

During the absorption and spontaneous emission of a near-resonant photon the atom receives a net momentum kick of $\hbar k$, where $k=2\pi/\lambda$ is the wavenumber of the light in vacuum. During each cycle the cooling is counteracted by the heating of the atom due to the recoil of the spontaneously emitted photon. Since the emission of the photon is in a random direction, this is comparable to a random walk problem in momentum space. For N photon emissions the mean momentum of the atom is $\langle p\rangle=0$ and the mean squared momentum magnitude can be written as $\langle p^2\rangle= N(\hbar k)^2$. Thus the equilibrium between the cooling and heating of the atom determines the lowest achievable temperature, for a two level atom this temperature is called the Doppler temperature. There are several ways to derive the Doppler temperature or Doppler cooling limit, one way is to use Eq. (2-13) in a one-dimensional optical molasses with substitution of

$$F_{\pm} = \frac{\hbar k \Gamma}{2} \frac{s_0}{1+(2\delta_{\pm}/\Gamma)^2}, \tag{2-18}$$

which is Eq. (2-12) far from saturation $s\ll 1$, where

$$\delta_{\pm} = \delta \mp \vec{k}\cdot\vec{v}. \tag{2-19}$$

Assuming for small velocities at the Doppler limit Eq. (2-13) can then be expanded in v to give

$$F \approx \hbar k \Gamma s_0 \frac{2\delta k}{(\delta^2+\Gamma^2/4)} v. \tag{2-20}$$

This is the viscous damping force for red detuned light $\delta<0$. The respective kinetic cooling energy can then be written as

$$\frac{d\langle KE_{Cool}\rangle}{dt} = \langle Fv\rangle = \hbar k\Gamma s_0 \frac{2\delta k}{(\delta^2 + \Gamma^2/4)}\langle v^2\rangle. \tag{2-21}$$

The kinetic heating energy rate can be written in a similar manner for $s_0 \ll 1$

$$\frac{d\langle KE_{Heat}\rangle}{dt} = 4\frac{d\left(\langle p^2\rangle/2m\right)}{dt} \approx 4\frac{1}{2m}\Gamma\frac{s_0}{2}(\hbar k)^2. \tag{2-22}$$

Where $\Gamma s_0/2$ is the spontaneous photon emission rate and the factor of four arises from the fact that the total momentum diffusion is four times larger due to spontaneous emission and absorption rates [134]. Adding both the heating and cooling rate gives

$$\frac{d\langle KE_{Cool}\rangle}{dt} + \frac{d\langle KE_{Heat}\rangle}{dt} = 0, \tag{2-23}$$

and substituting Eq. (2-21) and Eq. (2-22) into Eq. (2-23) gives a new expression for energy

$$\left\langle \frac{1}{2}mv^2 \right\rangle = -\frac{\hbar\Gamma}{8}\left(\frac{2\delta}{\Gamma} + \frac{\Gamma}{2\delta}\right), \tag{2-24}$$

which has a minimum at $\delta = -2\Gamma$. Rewriting Eq. (2-24) for the minimum mean kinetic energy then yields

$$T_D = \frac{\hbar\Gamma}{2k_B}, \tag{2-25}$$

where T_D is the Doppler temperature or Doppler cooling limit and k_B is the Boltzmann constant [22, 134, 135]. As seen the Doppler cooling limit depends only on the natural line width of the atomic transition. This derivation of the Doppler temperature is for a two level atom only, actual temperatures in a MOT were observed to be much lower than this predicted temperature, indicating other sub Doppler cooling mechanisms are at work [2-4, 134].

A new cooling limit below the Doppler temperature can be defined as the recoil

limit defined as

$$T_r = \frac{\hbar^2 k^2}{m k_B}, \tag{2-26}$$

which arises from the energy released by a single photon when it recoils from the atom. After the last absorbed photon the atom has to emit one final photon and is then left with this final recoil kick, thus putting a lower limit on the light assisted cooling process.

Cooling below the recoil limit is also possible by momentum diffusing the atoms into a passive, zero-velocity group or by evaporating the hottest atoms out of the trap. The first process can be done by velocity-selective coherent population trapping (VSCPT) or by the Raman cooling process. VSCPT works by optically pumping the atoms in the trap into non-light coupling transitions, also called dark states. The atoms in the dark state are then unable to interact with the light field (Note: VSCPT is less efficient in three-dimensions since the phase space is larger than that in one-dimension and therefore much harder to random walk into the right momentum superposition of the dark state.) [136, 137]. The Raman method accomplishes the same result by optically pumping the atoms into Raman transitions between ground state sublevels. Evaporative cooling on the other hand uses no light fields at all, it evaporates all the thermal atoms out of the trap with the help of elastic collisions. Cooling below the recoil limit reduces the temperature to such an extent that Bose-Einstein condensation (BEC) starts to take place.

The maximum energy that an atom can have and still be confined in the MOT defines the trap depth. When an atom enters the outer edge of the trap it is being damped by the laser beams, and when the atom can be sufficiently slowed before exiting through the other side of the trap it will be captured by the MOT. If the atoms Doppler shift kv

exceeds its natural linewidth Γ, the atom is not able to absorb a photon form the MOT laser beams, and is too fast to be captured by the MOT. Therefore, a maximum trap capture velocity that is required to capture atoms can be defined as $v_c=\Gamma/k$, which corresponds to a capture temperature of

$$T_C = \frac{m\Gamma^2}{k_B k^2}. \tag{2-27}$$

It is also possible that during an atomic collision in the MOT enough kinetic energy is picked up by two captured atoms that they exceed the capture velocity and are in consequence expelled from the MOT. The capture velocity depends on the maximum deceleration the atom can sustain over the width of the MOT. It also depends on the net force on the atom, which is proportional to the laser light intensity that acts on the atom.

2.4 THE FAR-OFF RESONANCE OPTICAL TRAP (FORT)

The FORT uses the dipole force Eq. (2-4) rather than the spontaneous force Eq. (2-5) of the MOT to trap atoms. The dipole force allows the FORT to operate at far from resonance conditions, which means that the excited state atomic population is negligibly low. This is in contrast with a MOT, which operates at close to atomic resonance conditions and has a large steady state excited population. Because of the large excited state population, trap loss collisions and other light induced collisions limit trap densities.

FORT's consist generally of a linearly polarized tightly focused Gaussian laser beam, which is usually tuned to the red of atomic resonance. Detuning to the red $(\delta < 0)$ causes the atoms to be attracted to the maximum laser intensity, while detuning to the blue $(\delta > 0)$ repels the atoms away from the maximum intensity laser light. The trapping

dipole force Eq. (2-4) can be integrated to give the following trapping potential for an atom in the rotating wave approximation,

$$U_{dip} = -\int F_{dip} dR = \frac{\hbar\delta}{2} \ln\left(1 + \frac{\Omega^2/2}{\delta^2 + (\Gamma/2)^2}\right). \tag{2-28}$$

This expression can be rewritten by substituting Eq. (2-7) to give

$$U_{dip} = \frac{\hbar\delta}{2} \ln\left(1 + \frac{s_0}{1 + (2\delta/\Gamma)^2}\right). \tag{2-29}$$

At a large detuning and laser intensity this expression becomes

$$U_{dip} \approx \frac{\hbar s_0 \Gamma^2}{8\delta}. \tag{2-30}$$

This shows that at large laser detuning and high laser intensity the trap depth can be maintained while at that large of a detuning the atoms will not absorb any light.

The main advantages of a FORT compared to that of a MOT are the higher atomic density and a well-defined polarized axis along which atoms can be spin polarized. The disadvantage of the FORT that it does not cool the atoms and that it generally can only trap a small number of atoms due to a small FORT volume. In many experiments the MOT is the starting point to capture a sample of atoms, which are then transferred into a FORT for further experimental study such as photoassociation and other cooling schemes.

2.5 COLD COLLISION THEORY

Collisional losses in a MOT are the main limiting factor of trap size and density. Light induced collisions between cold atoms tend to heat the sample of trapped atoms

thus limiting the cooling ability of the MOT. There are two types of collisions; elastic and inelastic. Elastic collisions take place when the quantum state for the two colliding atoms remains unchanged. Inelastic collisions result in a change of quantum state during collision. Elastic collisions are usually beneficial in rethermalization of atoms, especially for evaporative cooling in attaining BEC, while inelastic collisions are destructive and result in trap loss. Since during cold collisions the temperature in a MOT is below 1 mK new information can be obtained for low-energy collisions for neutral atoms or molecules, such as high-resolution molecular structures. For electronic ground states the standard theoretical potential scattering method can be used. The potential scattering method uses two ground state, distinguishable, and structureless particles with interaction potential *V(R)*, where *R* is the separation of the two particles in the center of the mass frame. For elastic scattering the time-independent Schrödinger equation can be used to describe the motion of the particle,

$$\left(\frac{\hbar}{2\mu}\nabla^2 + V(R)\right)\psi_k(R) = E\psi_k(R). \tag{2-31}$$

Where $\mu = (M_1 M_2)/(M_1 + M_2)$ is the reduced mass of the two particles, 1 and 2 $E = \hbar^2 k^2/2\mu$ is the particle energy, $\psi_k(R)$ is the particle wavefunction for its position and k is the particle's wave number. For a central force and for unpolarized atoms Eq. (2-31) can be solved by a partial wave series expansion, given by

$$\psi(k,R) = \sum_{l=0}^{\infty} A_l(k,R) P_l(\cos\theta). \tag{2-32}$$

Where $P_l(\cos\theta)$ are the Legendre polynomials and its individual coefficients are given by $A_l(k,R)$. In this analysis the incoming particle's wavefunction is expanded into

spherical partial waves, each with a well-defined angular momentum l. The scattering of each partial wave l is found by solving the radial part of the time-independent Schrödinger equation

$$\left(\frac{\hbar^2}{2\mu}\frac{d^2}{dR^2} - \frac{\hbar^2 l(l+1)}{2\mu R^2} - V(R) + E\right) u_l(k,R) = 0, \tag{2-33}$$

where $u_l(k,R) = RA_l(k,R)$, and the second term represents the centrifugal energy for a given partial wave l. The centrifugal barrier determines the maximum impact parameter b in a collision, when b exceeds a certain value the particles are reflected and no collision can take place. The impact parameter can be defined in terms of angular momentum as $L = \mu v_0 b$, where v_0 is the initial velocity of the particle, and its quantum mechanical counterpart can be written as $L = \hbar\sqrt{l(l+1)}$. An approximate solution to Eq. (2-33) at large internuclear distances can be written as the total scattering cross section,

$$\sigma(k) = \frac{4\pi}{k^2}\sum_{l=0}^{\infty}(2l+1)\sin^2\delta_l(k), \tag{2-34}$$

where $\delta_l(k)$ is the phase shift of the scattered waves with respect to the incident waves. For low collisional energies, at or below the Doppler limit, the centrifugal barrier for l=1 is higher than the kinetic energy in the collision, therefore only l=0 partial waves contribute, this is also referred to as s-wave scattering. For s-wave scattering at low energy the phase shift can be written as $\delta_0(k) = -ka$ where a is the scattering length defined as

$$a = -\lim_{k\to 0}\frac{\tan\delta_0(k)}{k}, \tag{2-35}$$

and the elastic scattering cross-section can be written as

$$\sigma(k \to 0) = 8\pi a^2. \tag{2-36}$$

This is of importance especially when considering a sample of atoms for cooling to a BEC. Atoms with large scattering cross-sections are more easily cooled than atoms with small cross-sections. The scattering length also determines the stability of the BEC, where a condensate with $a>0$ is stable and a one with $a<0$ is only stable when it consists of a small number of atoms [5, 22].

CHAPTER III

EXPERIMENTAL SETUP AND TECHNIQUE

Trapping two distinctively different species simultaneously in a MOT requires a unique experimental setup. For trapping ^{85}Rb, a permanently sealed MOT system is generally used where the ^{85}Rb atoms are present inside the MOT in the form of a background vapor. The atoms are then spatially confined with six counter-propagating laser beams and a quadrupole magnetic field. For ^{40}Ar* (* denotes that ^{40}Ar is in its metastable state) it is not quite as simple. Since Ar is a noble gas, it has to be trapped in its metastable state, because no laser sources exist to trap it in its ground state. To attain this state, a discharge source or electron bombardment has to be used, from which the metastable atoms emerge with a high velocity. Since only about one atom in a thousand is converted into a metastable state there are not a sufficient number of atoms in the low velocity tail of the Maxwell-Boltzmann distribution to establish a significant MOT. Some of the atoms in the low velocity tail are slow enough to be captured but to capture the faster atoms a Zeeman slower is employed. Once the ^{40}Ar* atoms are slowed in significant numbers they can then be confined in the MOT, just as the ^{85}Rb are. It is obvious that the additional ^{40}Ar* source, Zeeman slower, laser sources and other experimental requirements add to the complexity as compared to confining only ^{85}Rb atoms. This chapter deals with describing in detail the experimental setup and techniques used during the various stages of producing a metastable ^{40}Ar* MOT simultaneously with an overlapped ^{85}Rb MOT.

Fig. 3.1 depicts the experimental vacuum system setup, which is divided into three main regions; the source, Zeeman slower, and MOT regions. The laser sources are described separately from the vacuum system setup, since they have their own unique characteristics. In Fig. 3.2 a schematic of the trap regions and their pumping stages is shown. The system is quadruple differentially pumped by four turbo pumps, in-between each pumping stage an atomic beam skimmer is inserted to ensure a better pumping speed and to also help in collimating the $^{40}Ar^*$ beam for the capture region of the MOT. The operating pressures range from the source region of $\sim 10^{-5}$ Torr to $\sim 10^{-8}$ Torr in the MOT region. Mechanical roughing pumps back all four turbo pumps.

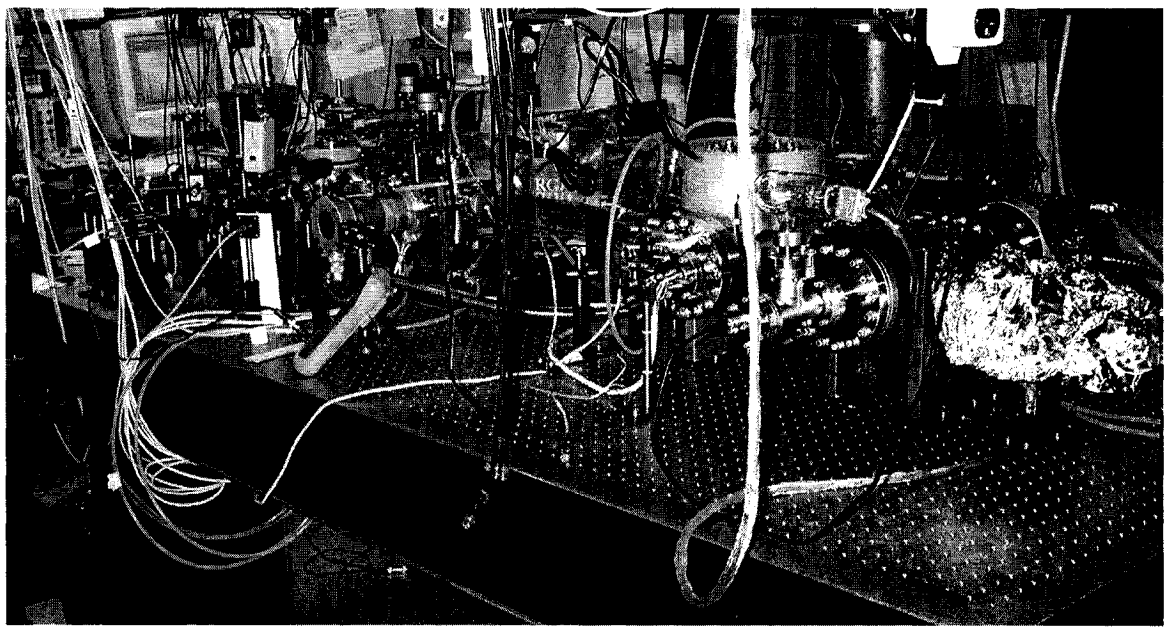

FIG. 3.1. Picture of the dual species vacuum system setup. From right to left; the source, Zeeman slower and MOT regions. The Zeeman slower is shown encapsulated in cooling jacket. The source is covered by aluminum foil to shield against stray rf.

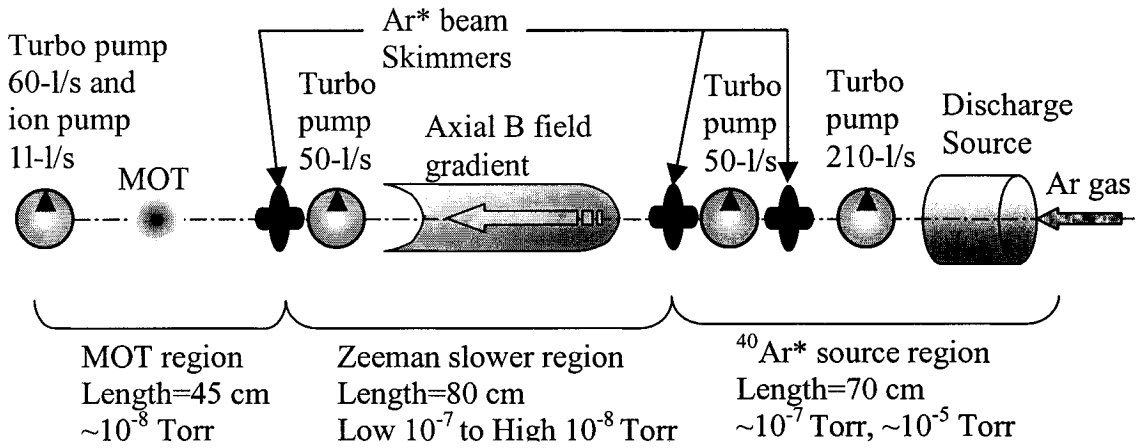

FIG. 3.2. Schematic of the three dual species trap's vacuum system regions and their quadruple differentially pumped stages.

3.1 THE SOURCE CHAMBER REGION

The source chamber region itself can be subdivided into three subdivisions; the ^{40}Ar* source, the source chamber and the intermediate chamber.

There are several different methods available to generate a metastable noble gas beam, one of the most common methods used is that of the high voltage DC discharge type. The gas commonly moves down a Pyrex glass tube. As it reaches the nozzle a high voltage tungsten wire creates a discharge, exciting the atom before it leaves through a skimmer into the vacuum chamber. This type of discharge has a drawback in that it heats the atoms and therefore it has to be frequently cooled with liquid nitrogen [131, 132, 138-140]. Other discharges of the microwave [141] and radio frequency (rf) type are less commonly used but also present a feasible way to produce a metastable atomic beam with comparable or greater flux [142]. In this work we used an rf-driven discharge modeled

after the type described by Chen et al. and built after the concept of Macalpine et al. [143]. The rf-driven discharge is depicted schematically in Fig. 3.3. The research grade Ar gas moves from a tank through a regulator and a needle valve (Granville Phillips Company #5097 with 216 Servo Driver valve assembly controller) into the quartz tube (inside diameter=10 mm), from there it is excited by the coaxial resonator. The coaxial resonator is made out of a 14 gauge copper magnet wire coil and is enclosed by a brass shield, Fig. 3.3. The dimensions of Fig. 3.3 are as follows: D=6.3 cm, d=3.2 cm and b=7 cm, the number of windings of the copper coil are N=11. In Fig. 3.4 the actual rf-driven resonator with orientation toward the source vacuum chamber is shown.

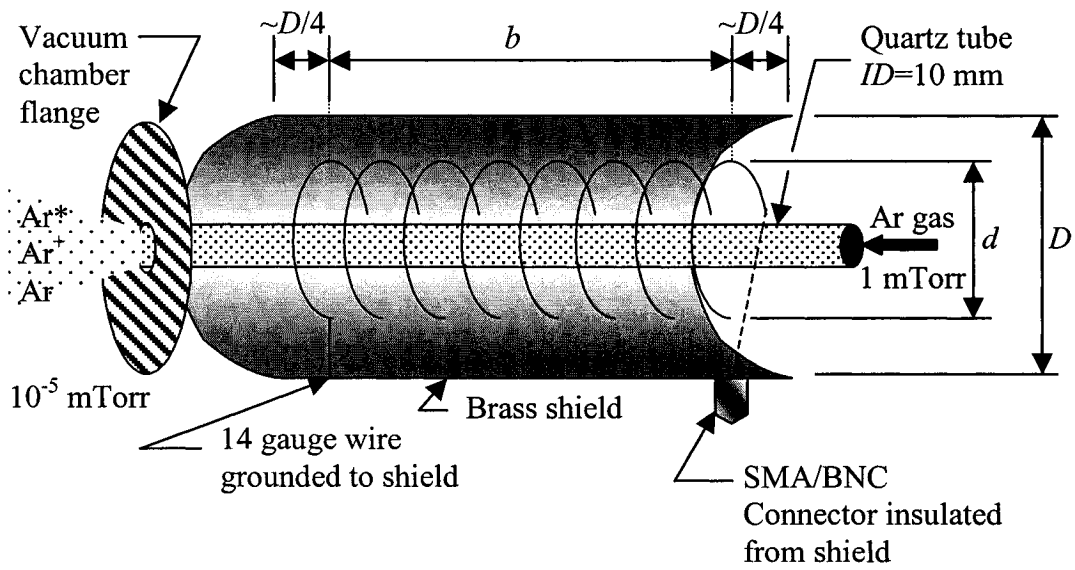

FIG. 3.3. Cutaway view of the coaxial resonator. The copper wire with N windings is enclosed in the brass shield. The Ar gas leaves the resonator as metastables, ions and unaffected Ar gas.

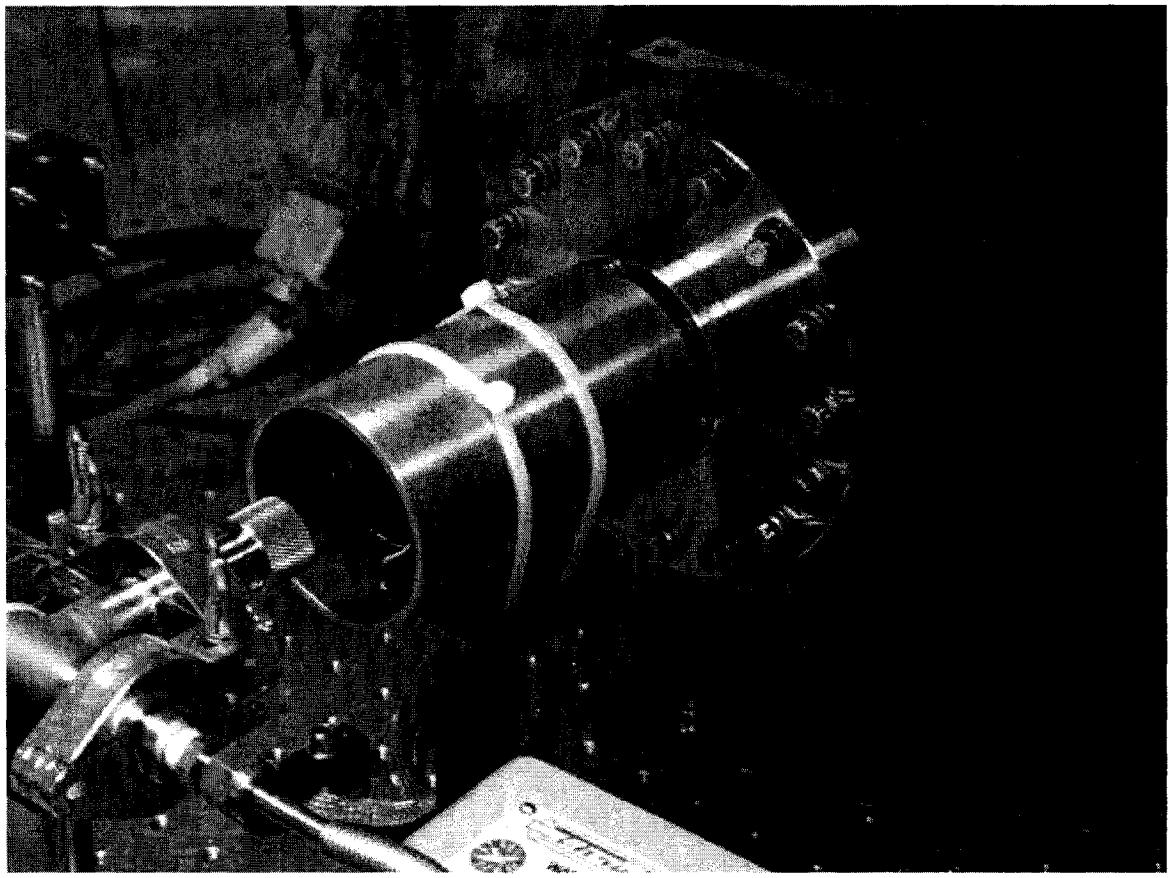

FIG. 3.4. Picture of the rf-driven resonator. It mounts to the flange of the vacuum source chamber with brass shield and quartz tube. Copper wire windings can also be seen. The gas enters from the bottom right.

The resonator resonates at 155 MHz and an rf power of typically 7-15 W, the circuit is impedance matched, and composed of several amplifiers and attenuators, as shown in the circuit flow diagram of Fig. 3.5. The gas that leaves the resonator is in the form of Ar, Ar^+, and Ar*, only about one out of a thousand atoms out of the resonator are metastables.

Immediately after the Ar, Ar^+, and Ar* atoms leave the source and enter the source chamber the ions are removed from the atom beam by means of an ion deflector.

The ion deflector consists of a pair of electric field plates that are mounted parallel to each other and are separated by a distance of 2.5 cm. The atom beam then passes in-between the plates. The ion deflector assembly was built out of stainless steel and the field plates are insulated from the mounting rods with ceramic spacers. One of the field plates was grounded and the other was set to 100 V, this was more than sufficient to deflect the ions out of the main beam. The remaining Ar and metastable atoms are then collimated by a skimmer, which separates the source chamber and the intermediate chamber, Fig. 3.6.

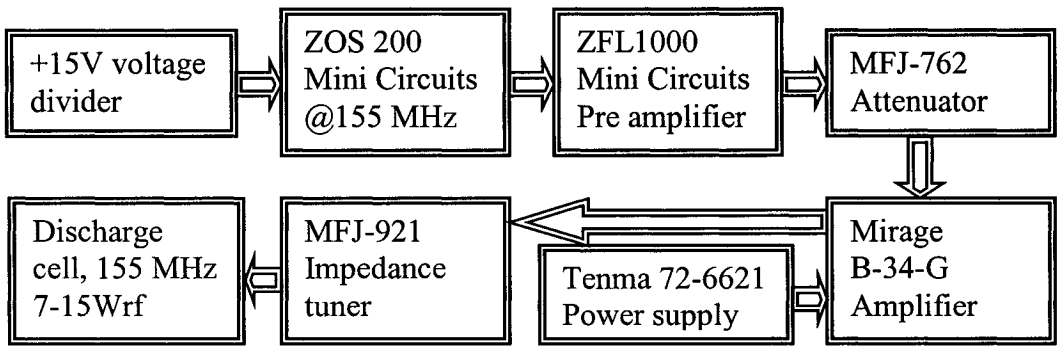

FIG. 3.5. Flow diagram of impedance matched rf resonator circuit. Its resonance frequency is 155 MHz and it produces typically 7-15 Wrf.

The optimal source operating pressure, optimized for maximum metastable flux, is found to be of the range of $1x10^{-5}$ Torr to $5x10^{-5}$ Torr in the source chamber. The pressure in the discharge itself is of the order of ~1 mTorr. The vacuum pressure in the source chamber was initially maintained at that pressure with a 110-l/s Pfeiffer TPU110 turbo pump that later was upgraded to a 210-l/s Pfeiffer TMU262P.

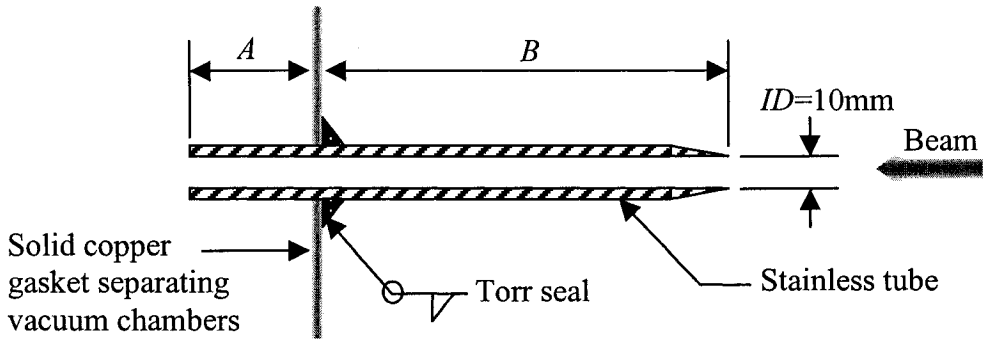

FIG. 3.6. Drawing of an atomic beam skimmer. Three different skimmers are used with dimensions A=25 mm and B=90 mm for the collimator separating the source/intermediate chamber (6" solid copper gasket Duniway BG-600) and the intermediate chamber/Zeeman slower (2 3/4" solid copper gaskets Duniway BG-275). For the separation of the Zeeman slower/MOT chamber A=3 mm and B=45 mm, this is due to physical restraints in the vacuum system (2 3/4" solid copper gaskets).

Directly adjacent to the source chamber was a 2 3/4" six-way conflat cross small observation chamber that is part of the intermediate chamber. This observation chamber was used to optimize the metastable flux since the metastable flux had to be optimized with a minimum increase in system pressure. The observation chamber was later removed when it was no longer needed. The intermediate chamber is pumped with a 50-l/s Pfeiffer TPH050 turbo pump in conjunction with a liquid-nitrogen cold trap. The purpose of this chamber is to further reduce the pressure in the system before the Ar* atoms move into the Zeeman slower, which is separated from the intermediate chamber by another collimation tube of the same make as shown in Fig. 3.6. The pressure in the intermediate chamber is typically on the order of ~3×10^{-7} Torr for a source chamber

pressure of 1.5×10^{-5} Torr. The atomic metastable beam flux was initially optimized by observing the fluorescence signal with a photomultiplier tube (PMT) (Hamamatsu R636-10), which was mounted on the observation chamber, shown in Fig. 3.7. The photomultiplier tube was equipped with a narrow bandpass interference filter at 811 nm (Esco S908100). A laser beam that intersected the atomic beam at 90° was allowed to scan several MHz over the $^{40}Ar^*$ 811 nm cycling transitions to obtain a Doppler free signal, this produced the desired fluorescence signal necessary for optimizing the metastable beam, Fig. 3.8. It was later possible, due to experience gained with the experimental setup, to optimize the metastable beam directly by observing the $^{40}Ar^*$ MOT fluorescence.

It is estimated that the metastable angular flux density of the $^{40}Ar^*$ atomic beam is $\dot{\Phi}/\Omega = 4 \times 10^{14}$ atoms $s^{-1}sr^{-1}$ as reported in Ref. [142], where Ω is the geometrical solid angle occupied by the atoms in the beam. Atom beams are also sometimes characterized by their beam brightness or radiance R and their spectral brightness or brilliance B, which is defined as

$$R = \frac{\dot{\Phi}}{\pi x_{\perp}^2 \Omega}, \tag{3-1}$$

and

$$B = R\frac{\bar{v}_{\parallel}}{v_z}. \tag{3-2}$$

Where $x_{\perp}$ is the beam radius, $\bar{v}_{\parallel}/v_z$ is the average longitudinal velocity divided by their longitudinal velocity spread, and v_z is the direction along the longitudinal axis. This quantity is generally $\bar{v}_{\parallel}/v_z \cong 1$ for atomic beams causing R and B to have similar values

[131]. Thus the $^{40}Ar^*$ atomic collimated beam is expected to have a radiance and brilliance of $B \cong R = 5 \times 10^{18}\ s^{-1}m^{-2}sr^{-1}$.

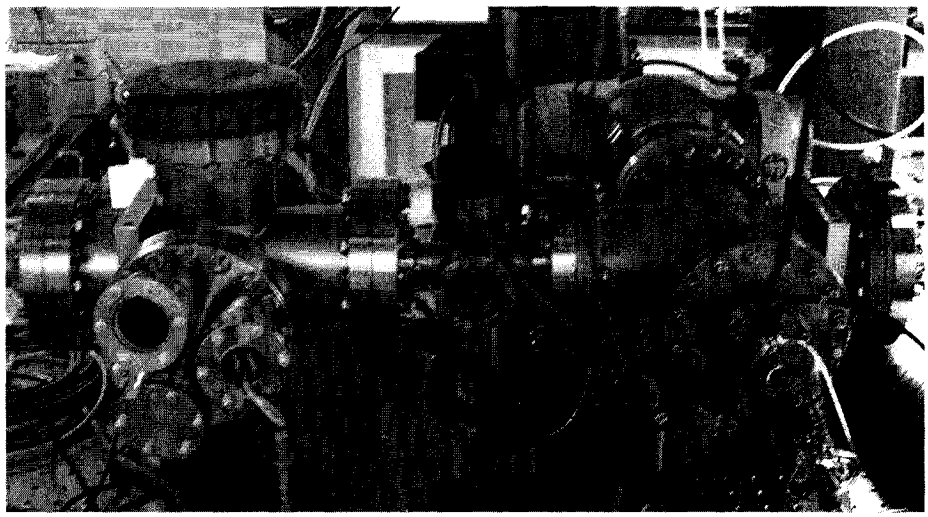

FIG. 3.7. Picture of the source and intermediate vacuum chambers. The source chamber is on the right and the intermediate chamber on the left. In between is the small observation chamber with the PMT mounted on top (black box) and the laser beam mirrors shown for an orthogonally intersecting laser beam on the metastable atoms. The observation chamber was later removed, when it was no longer needed. The atomic beam is moving from right to left.

As the argon beam leaves the intermediate chamber to enter the Zeeman slower region its most probable velocity is estimated to be 400 m/s and is composed of a ratio of $Ar^*/Ar \approx 10^{-3}$. This signifies that hot Ar atoms are migrating into the trapping region, increasing the MOT's background pressure; this is a disadvantageous side effect of working with metastable atoms.

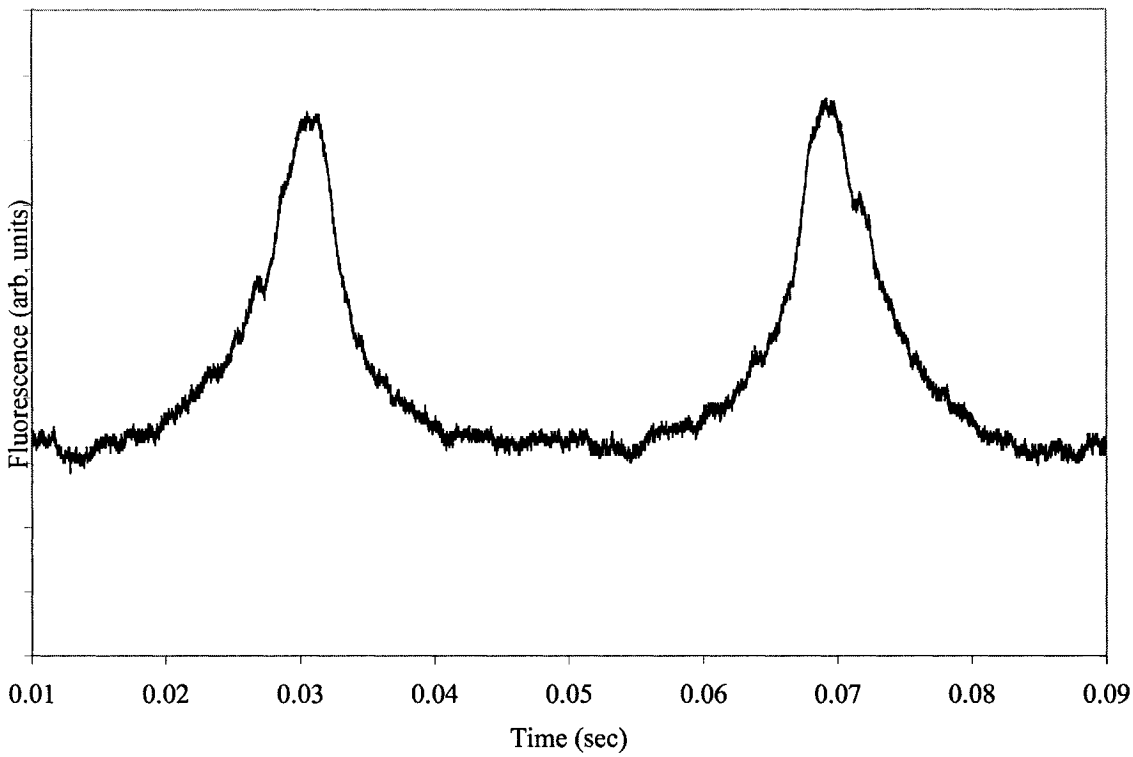

FIG. 3.8. Fluorescence signal of metastable $^{40}Ar^*$ beam. As is observed from the PMT, for metastable flux optimization. $^{40}Ar^*$ has only one peak because it does not have a hyperfine structure, the second peak is a reflection of the first peak due to the laser scanning back.

To reduce some of the background pressure in the MOT the initial vacuum system construction consisted of three turbo pumps. This system was later upgraded to four turbo pumps, further reducing background pressure. In addition to the fourth turbo pump a third collimation skimmer was also installed at the end of the Zeeman slower, resulting in a final vacuum system as depicted in Fig. 3.2. Future system optimizations could include a beam bending technique in which a metastable beam is deflected out of the source beam. A laser would be used to bend the beam through the collimation tubes thus

allowing only metastable atoms into the MOT chamber, Fig. 3.9. This method would reduce MOT background pressure significantly.

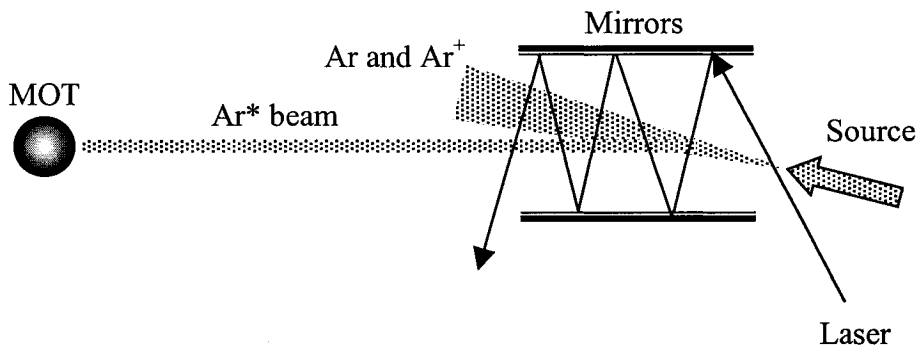

FIG. 3.9. A beam of Ar* atoms is being deflected from the main source beam by a laser. The Ar and Ar^+ atoms are removed from the system without increasing the background pressure in the MOT chamber. This proposed setup is similar to that one of a 2-D collimator [22, 131].

3.2 THE ZEEMAN SLOWER REGION

The average Maxwell-Boltzmann velocity distribution of atoms leaving an oven or an rf-driven discharge source, as used in this work, is much too fast to be captured by a MOT in significant numbers. Atoms therefore have to be slowed down and cooled. One method of accomplishing this process is by using a Zeeman slower. A Zeeman slower uses a variably changing magnetic field and a counterpropagating circularly polarized laser beam to longitudinally slow the atoms down in 1-D. In this experiment σ^+ circularly polarized light was used. The laser beam works with the same principle on the

atoms in 1-D as described in Chapter 2 Eq. (2-12), which is using the spontaneous force on the atoms by scattering photons. To effectively slowing and 1D cooling the atoms the laser beam has to be resonant with the atom. To accomplish resonance the atoms are Zeeman shifted with a magnetic field. But, because the atoms change velocity during deceleration they are continuously detuned from the light field due to the Doppler shift. To compensate for this shift the magnetic field has to change with the slowing atoms. An inhomogeneous magnetic field can compensate for the detuning caused by the Doppler velocity shifted atoms, effectively keeping the atoms in resonance with the light and slowing them to the desired MOT capture velocity. The governing equation for this process can be written as follows

$$kv(z) - \frac{\mu_B B(z)}{\hbar} + 2\pi\delta = 0. \tag{3-3}$$

Where $k = 2\pi/\lambda$ is the wave number of the transition, $kv(z)$ is the Doppler velocity, μ_B is the Bohr magneton, $B(z)$ is the variable magnetic field, and δ is the laser detuning. $\delta = \omega_{Laser} - \omega_{Atom}$ is the difference between the laser frequency and atom rest frame frequency. The velocity with respect to axial distance z can be defined using kinematics

$$v^2(z) = v_i^2 + 2a\Delta z, \tag{3-4}$$

rewriting Eq. (3-4) into a second equation for initial and final velocity and setting this equal to twice the atomic deceleration $2a$ in Eq. (3-4) gives

$$v(z) = v_i\sqrt{1 - \frac{z - z_i}{z_f - z_i}\left(1 - \frac{v_f^2}{v_i^2}\right)}. \tag{3-5}$$

Where the subscripts i and f stand for initial and final velocity respectively: $v(z)$ is then an expression for the axial velocity profile the atom has to follow for it to slow down to v_f.

Substituting Eq. (3-5) into Eq. (3-3) gives the

$$B(z)=\frac{\hbar 2\pi\delta}{\mu_B}+\frac{\hbar k v_i}{\mu_B}\sqrt{1-\frac{z-z_i}{z_f-z_i}\left(1-\frac{v_f^2}{v_i^2}\right)}, \qquad (3\text{-}6)$$

which is the magnetic field that the Zeeman slower has to have to satisfy the atomic resonance condition.

It is customary that the magnetic field in the Zeeman slower is generated by winding many loops of magnetic wire around the vacuum tube of the Zeeman slower and sending current through the wire. The Zeeman slower was thus wound and the current matched so that it would conform to the required profile of Eq. (3-6). To match the magnetic field usually entailed that the windings were more numerous at the beginning of the Zeeman slower and started to taper down toward the end [22, 131, 144-151]. A simpler design to fabricate is the single layer variable pitch design. The drawback of this design is that it requires more current to generate the same magnetic field as the taper down design. This results in an increased heating of the Zeeman slower, which has then to be cooled with a cooling jacket. In this work a single layer variable pitch wound coil with 14 gauge copper wire was chosen to generate the magnetic field [132]. The single layer wire was then encapsulated with a brass water-cooled cooling jacket, Fig. 3.10.

Also shown in Fig. 3.10 is a reverse magnetic field coil, this two coil magnetic setup serves three purposes [131, 132, 148-150]. First, it helps in the power dissipation. The magnetic field is distributed over both a positive and a negative field gradient that allows for a less dense winding of the coils, which results in a lower magnetic field required. Secondly, the sharp change in field gradient at the end of the coil causes a rapid decoupling of the atoms of the slowing laser beam's light field, with this the final

velocity of the decelerated atoms can be fine tuned. Thirdly, the separation between two coils can be used as a place for locating a vacuum pump, additional diagnostic instrumentation, and optical compressors. Finally, it is important to note that the detuning of the Zeeman slower is chosen to be $\delta \sim -27\Gamma$. This is important so that the slowing laser beam, which passes directly through the MOT, does not affect trapped atoms in the MOT.

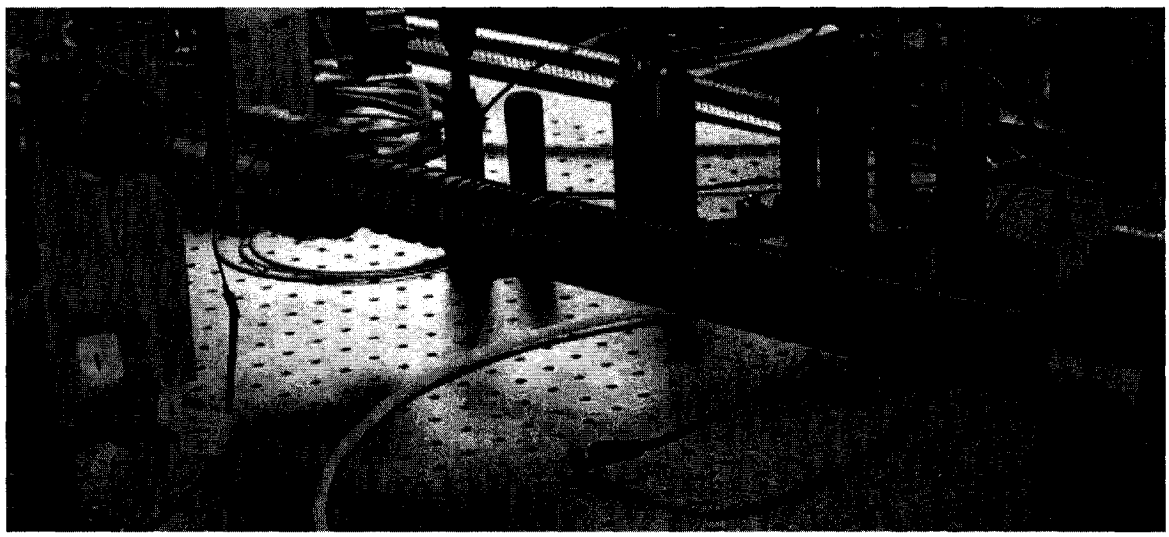

FIG. 3.10. Variable pitch wound Zeeman slower. On the left is the smaller second solenoid that creates a reversed $B(z)$ field. The brass cooling jacket and third turbo pump are not shown in this picture. The tube diameter is 7.5 cm. The atoms are moving from right to left.

Using Eq. (3-6) for both coils, where the final velocity of the atoms exiting the first solenoid becomes the initial velocity of the atoms entering the second solenoid. The resulting theoretical magnetic field and its experimental matched real life counterpart are

shown in Fig. 3.11.

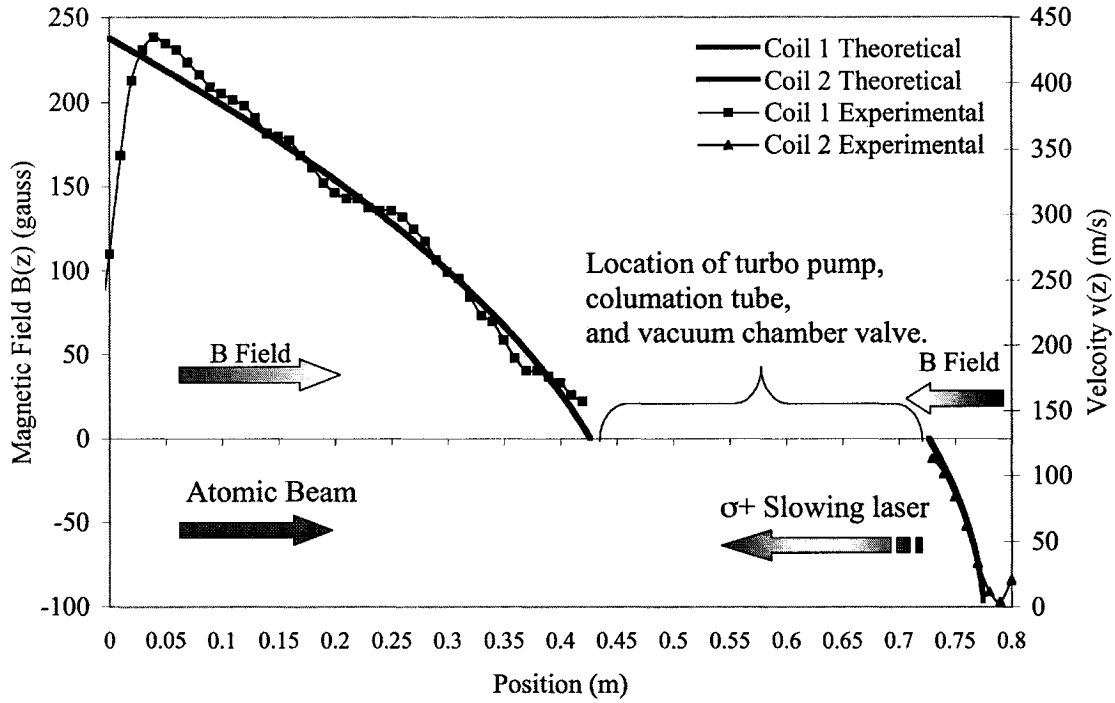

FIG. 3.11. Theoretical and actual matched magnetic field profile of the Zeeman slower.

In obtaining the magnetic profile of Fig. 3.11 the following design conditions cannot be exceeded

$$\mu_B \frac{dB(z)}{dz} v(z) \leq \hbar k a. \tag{3-7}$$

This expression is obtained by differentiating Eq. (3-3) with respect to z. It also states that to keep the atoms in resonance with the laser light field during the slowing process, the change in detuning due to the varying magnetic field must not exceed the changing Doppler shift. Assuming maximum saturation, Eq. (2-11) can be rewritten as

$a_{max} = \hbar k\Gamma/(2m)$, introducing a design safety parameter η, which is $\eta \leq 1$, the deceleration can then be expressed as $a=\eta a_{max}$ [131, 149-151]. The design limit for the magnetic field gradient Eq. (3-7) can then be rewritten as

$$\frac{dB(z)}{dz} \leq \frac{\eta \hbar k \Gamma}{\mu_B v(z) 2m}. \tag{3-8}$$

Physically atoms are limited in their deceleration because their scattering rate is also limited. A design safety factor of η=0.3 was chosen for this experimental setup. The required Zeeman slower parameters for this work are presented in Table 3.1.

TABLE 3.1. Design parameter requirements used in the Zeeman slower.

Parameter	First slowing coil	Second slowing coil
Length Δz	40 cm	10 cm
Entrance velocity v_i	400 m/s	129 m/s
Exit velocity v_f	129 m/s	20 m/s
Optimal current	34 A	15 A
Design safety parameter η	0.30	0.30
Slowing laser Power	40 - 50 mW	40 - 50 mW
Slowing laser intensity I	102 - 125 mW/cm^2	102 - 125 mW/cm^2
Laser detuning δ	160 MHz (-27Γ)	160 MHz (-27Γ)

The Zeeman slower is pumped with a Pfeiffer TPH050 50-l/s turbo pump, located

right after the first solenoid, the pressure is estimated in the Zeeman slower region to be in the low 10^{-7} Torr to high 10^{-8} Torr. The third collimating skimmer nipple, Fig. 3.6, is located in front of the second slowing solenoid.

3.3 THE MOT CHAMBER REGION

After the slowed metastable $^{40}Ar^*$ atoms leave the Zeeman slower region they enter the MOT region to be trapped simultaneously with the already present ^{85}Rb. The MOT is a cylindrical chamber that is 20 cm (8") in diameter and 6 cm (2 2/5") high; it has fourteen 7 cm (2 3/4") diameter Conflat-type vacuum flanged ports, Fig. 3.12. Those ports are used for connecting the MOT to the Zeeman slower, and to other vacuum chamber components such as a turbo pump, ion pump, channel electron multiplier (CEM), residual gas analyzer (RGA), and optical windows. The glasses of the optical windows are 3.7 cm (1 1/2") in diameter and anti reflection (AR) coated. They are used for the six counterpropagating MOT laser beams intersecting at the center of the MOT to form the trap, the observation of trap fluorescence with photomultiplier tubes (PMT), and for probe beams used in absorption measurements. All Conflat-type flanges are sealed with copper gaskets and the whole system has been baked out to ensure a clean vacuum environment [133]. The MOT region is pumped by a Pfeiffer TMU 071P 60-l/s turbo pump and an 11-l/s ion pump. The pressure in the trap region for dual MOT operation is estimated to be in the mid ~10^{-8} Torr range and was initially monitored through the ion pump current and later the RGA. Rb atoms are loaded into the MOT from a background vapor that was released into the MOT region trough an alkali-metal dispenser (SAES Getters), the Getter current was then optimized for maximum trap fluorescence to be

~(3.5±0.1) A [152]. A CEM (Amptek MD-502) is placed in one of the MOT chamber ports 13 cm from the center of the trap to monitor ion production. The trap fluorescence of each species can be monitored simultaneously by two independent PMTs (Hamamatsu R928). Each PMT is equipped with a narrow bandpass interference filter (Melles Griot 03 FIL 056 (780 nm) for ^{85}Rb, and Esco S908100 (811 nm) for ^{40}Ar*). The fluorescence

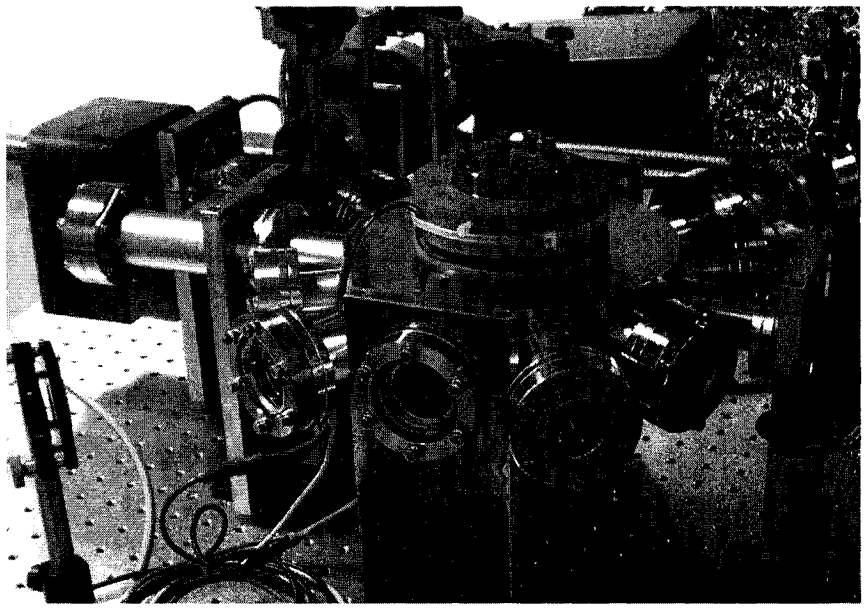

FIG. 3.12. Picture of the dual species MOT chamber. Zeeman slowed ^{40}Ar* atoms enter from the right, ^{85}Rb atoms are released from the dispenser seen in the rear right wrapped in aluminum foil. The ion pump is on the far left, with the turbo pump not clearly visible in the photo. The turbo pump was later mounted directly to a MOT port for a higher conductance. No trapping optics are shown in this early picture.

can be monitored through one port by using an optical aperture, a beam splitter, and the appropriate lenses to focus the fluorescence onto the PMT tubes. To ensure that both the

^{85}Rb and ^{40}Ar* traps are spatially overlapped two charge coupled device (CCD) cameras (Sanyo VCB-3524) were placed at right angles to each other. For absorption imaging a triggered CCD camera (Apogee AP7B) with a resolution of 512x512 pixels with a pixel size of 24 μm, was used.

For trapping both ^{85}Rb and ^{40}Ar* simultaneously, two separate laser sources at different wavelengths have to be used, 780 nm for ^{85}Rb and 811 nm for ^{40}Ar*. Because of physical constraints in the number of optical window ports available for trapping and observation, the two laser beams are generally spatially overlapped and sent into the MOT with the aid of dichroic optics. Due to the small wavelength separation of the two trapping species, dichroic optics are difficult and expensive to manufacture. Therefore, an alternate method for overlapping the two beams has been used, Fig. 3.13. The two laser beams arrive at the MOT via single-mode optical fibers (ThorLabs P3-4224-FC-5), each beam after exiting the optical fiber is identically collimated and then sent through a half-wave plate before being combined on a polarizing beam-splitter cube. The beams leave the polarizing beam-splitter cube completely spatially overlapped, but their polarization axes are orthogonal to each other. To remedy this situation a half-wave plate rotates the polarization of both beams by 45°, then the combined beams get expanded by an optical telescope to a $1/e^2$ diameter of 1 cm. The combined beam is then further split into two equal parts by an additional polarizing beam-splitter cube, one half leaves toward the MOT's vertical axis arm, while the second half is further split by a 50-50 non-polarizing beam splitter to be sent to each of the horizontal arms of the MOT's axis. The three

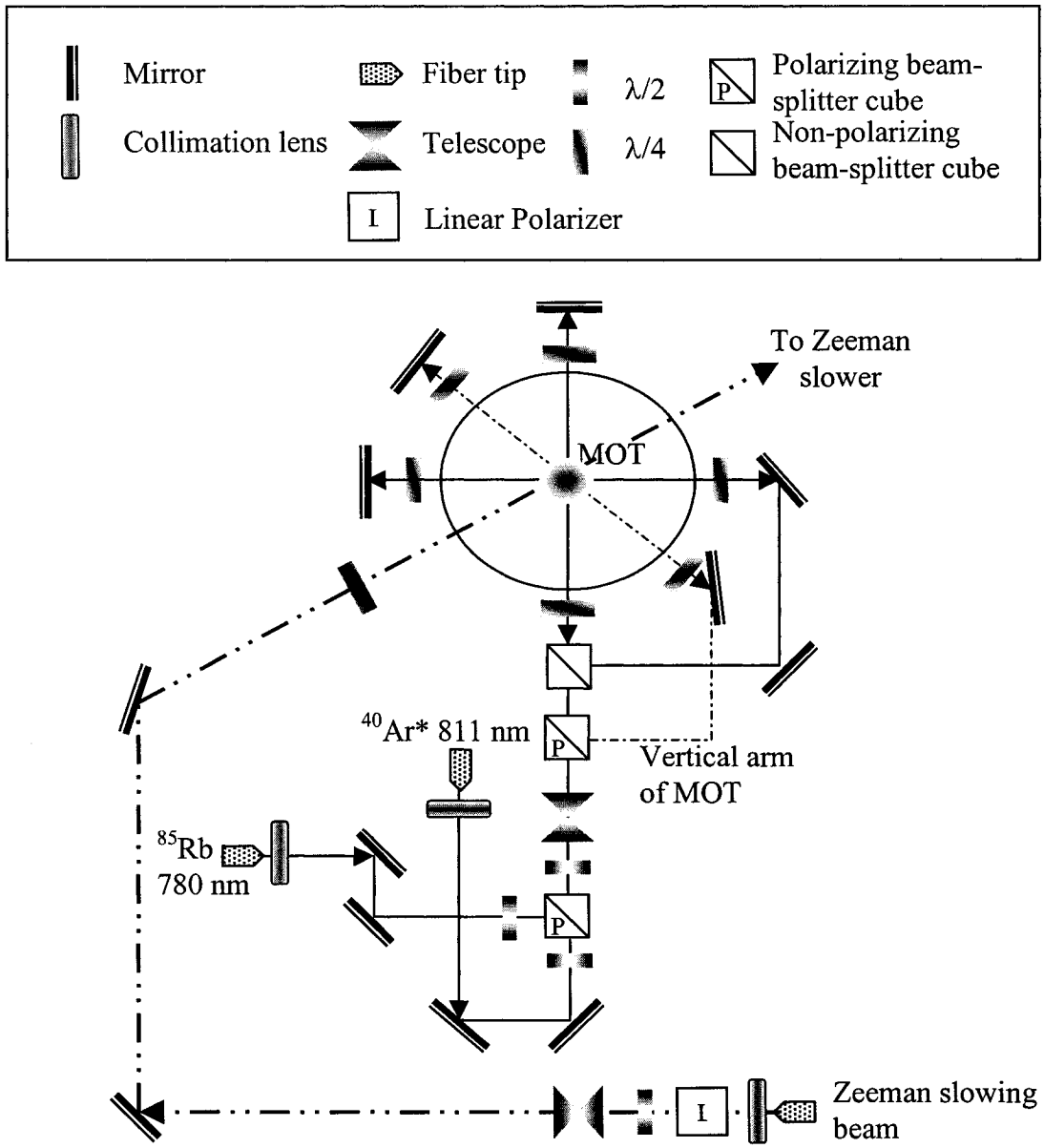

FIG. 3.13. Optical arrangement and technique for overlapping the two species laser beam.

beams are circularly polarized by quarter-wave plates before they enter the MOT and before being retroreflected back through the MOT they are oppositely circularly polarized again by another set of quarter-wave plates. MOT laser intensities and parameters for the two species are summarized in Table 3.2.

Also shown in Fig. 3.13 is the optics for the Zeeman slower as it passes through the MOT region. The laser power for the Zeeman slower arrives the same way as the MOT laser power, through a single MOT optical fiber. It also gets collimated before passing through a linear polarizer and a half-wave plate before being expanded into a $1/e^2$ diameter 1 cm beam. A quarter-wave plate then circularly polarizes the beam before it enters the MOT chamber and travels down the Zeeman slower.

TABLE 3.2. Typical dual species MOT operating parameters.

Parameter	^{85}Rb	^{40}Ar*
Trapping wavelength	780 nm	811 nm
Laser Power	6 - 8 mW	30 - 50 mW
Laser Intensity I	30 - 40 mW/cm^2	152 - 250 mW/cm^2
B field vertical-axis	6.6 G/cm	6.6 G/cm
Trap diameter typical	~0.6 mm	~0.6 mm
Trap size atoms	1.2x10^6 atoms	1.4x10^6 atoms
Trap density	~10^{10}/cm^3	~10^{10}/cm^3
Detuning δ	-2Γ=12 MHz	-3/2Γ=9 MHz

3.4 ELECTRONIC TRANSITIONS OF THE ^{85}Rb AND ^{40}Ar ATOM

^{85}Rb is an alkali-metal atom; it is located in the extreme left-hand column of the periodic table. The core is a closed shell, with one valence electron. Since the core is closed it does not contribute to the orbital angular momentum of the atom, which is solely determined by that of the valence electron. The state of the electron determines the orbital angular momentum $\vec{L} = \vec{l}$ and the spin angular momentum $\vec{S} = \vec{s}$ (s=1/2 for an electron) of the atom, to give the total angular momentum $\vec{J} = \vec{j} = \vec{l} + \vec{s}$ of the electron. (Capital letters refer to atomic states while small letters to those of the electrons). For the alkali-metal atoms the Russell-Saunders notation is used to specify the different electronic atomic states. This notation is defined as

$$n^{(2S+1)}L_J, \tag{3-9}$$

where n is the principle quantum number of the valence electron. Due to different values of $\vec{J}$, the energy levels of the alkali-metal atom are split in the following ways. The first is the spin-orbit interaction $V_{SO} = A\vec{L} \cdot \vec{S}$, which gives rise to the fine structure splitting of the atom. The energy levels are further split by the interaction with the nuclear spin $\vec{I}$ of the atom. The total angular momentum of the atom then becomes $\vec{F} = \vec{I} + \vec{J}$, where the nuclear spin of the atom couples with that of the total angular momentum of the electron. With the interaction of $B\vec{I} \cdot \vec{J}$, different values of $\vec{F}$ result in the hyperfine structure splitting of the atom. The energy level diagram of ^{85}Rb is depicted in Fig. 3.14 (a). (For the $5^2P_{3/2}$ state of ^{85}Rb atom the fine- and hyperfine structure constants have experimentally be determined to be A=25.0 MHz and B=25.8 MHz [22].) Due to its hyperfine splitting the trapping of ^{85}Rb is slightly complicated, because for one out of

approximately 1000 excitations from $F=3\rightarrow F'=4$ trapping cycling transition, a $F=3\rightarrow F'=3$ transition will take place instead. In this case the electron can decay back to the F=2 state, the F=2→F=3 transition is a non-cycling transition. This decay would effectively deplete the trap, so in order to circumvent this a hyperfine repumper is used to repopulate the upper hyperfine level of the ground state. (A hyperfine repumper is an additional laser separate from the trapping laser, or a 3.1 GHz sideband on an existing Rb trapping laser.)

^{40}Ar is a noble gas, located on the far right hand side of the periodic table. In laser cooling and trapping, the metastable state of the atom has to be used, because no available laser source for a ground-excited state cycling transition exists. ^{40}Ar has two metastable states where the lower state is suitable for trapping, since it has a cycling transition at a wavelength of 811 nm, which can be attained with present laser sources. The metastable state is the state of the atom where the electron can not decay to the ground state due to a forbidden electric dipole transition, therefore having a lifetime of the order of ~60 sec for ^{40}Ar lower metastable state. This state can then effectively act as the ground state for an atomic trapping transition. Since even isotopes of noble gas atoms do not have a nuclear spin, they also do not have a hyperfine structure, thus simplifying their energy level structure and trapping ability. Due to the metastability of the atom, the outer electron is in a highly excited state, which is close to the ionization level of the atom. Due to this, the atom can be treated as a one-electron atom, with the core and outer electron having an orbital and spin angular momentum. Two notations are used to couple the angular momenta of the core and valence electron into a total angular momentum of the atom, the first is again the Russell-Saunders notation for noble gases and the second is

referred to as the *jl* coupling

$$n^{(2S_{ce}+1)}L_J, \tag{3-10}$$

$$^{(2S+1)}L_j nl[K]_J. \tag{3-11}$$

Here L and S is the core angular and spin momenta respectively and l and s are the respective electronic angular and spin momenta. The following coupling takes place for the core to give $j=L+S$, this is coupled with l to give $K=j+l$, which is then finally coupled to s to give $J=K+s$, the total angular momentum of the atom. Where in the Russell-Saunders notation the S_{ce} stands for the coupling of both the core and valence electrons spin, $S_{ce}=S+s$ [22]. The trapping cycling transition and their respective energy levels for ^{40}Ar is represented in Fig. 3.14 (b).

Table 3.3 summarizes all the pertinent trapping transitions and parameters for both ^{85}Rb and ^{40}Ar respectively.

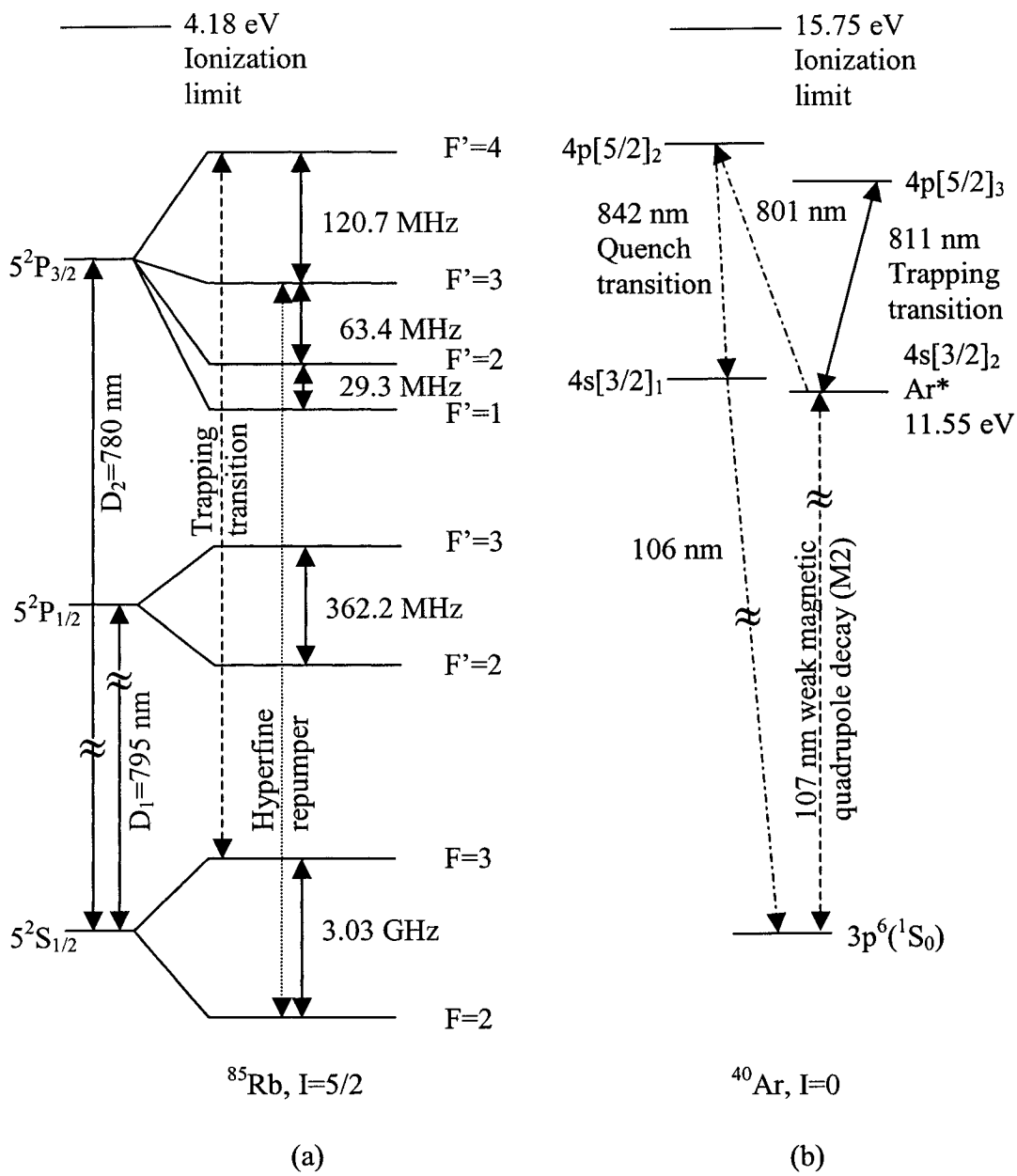

FIG. 3.14. Detailed energy level diagrams. For (a) ^{85}Rb with hyperfine splitting, the cycling and hyperfine repumping transitions, and (b) ^{40}Ar with its lower metastable state acting as trap cycling transition and a 842 nm quench transition shown.

TABLE 3.3. Recapitulation of the relevant trapping and atomic parameters for both ^{85}Rb and ^{40}Ar [22].

Parameter	**Symbol**	**^{40}Ar***	**^{85}Rb**
Mass (1 amu=1.66x10^{-27} kg)	M	40	85
Abundance		99%	72%
Nuclear spin	I	0	5/2
Trapping transition		$4s[3/2]_2 \rightarrow 4p[5/2]_3$	$5^2S_{1/2} \rightarrow 5^2P_{3/2}$
Transition wavelength	λ	811.75 nm	780.24 nm
Transition energy	$\hbar\omega_{ge}$	1.527 eV	1.589 eV
Upper state lifetime	τ	27.09 ns	26.63 ns
Linewidth	$\Gamma/2\pi$	5.87 MHz	5.98 MHz
Absorption cross section	σ_{ge}	314.6x10^{-15} m^2	290.7x10^{-15} m^2
Saturation intensity	I_s	1.44 mW/cm^2	1.64 mW/cm^2
Capture velocity	v_c	4.77 m/s	4.66 m/s
Capture temperature	T_c	109.33 mK	222.12 mK
Doppler velocity	v_D	17.12 cm/s	11.85 cm/s
Doppler temperature	T_D	140.96 μK	143.41 μK
Recoil velocity	v_r	1.23 cm/s	0.602 cm/s
Recoil temperature	T_r	0.727 μK	0.37 μK
Metastable Exc. Energy		11.55 eV	N/A
Metastable lifetime		60 sec	N/A
Ionization Potential		15.75 eV	4.18 eV

CHAPTER IV

LASERS AND OPTICAL METHODS

To be able to trap two different atomic species simultaneously requires two separate laser sources. Since each atom has its own unique independent energy level structure its trapping laser cycling transitions are also different, as shown in Fig. 3.14. Consequently, both the ^{85}Rb and ^{40}Ar* have different laser wavelength requirements, which cannot be fulfilled by a single laser source. In addition, some experiments require probing lasers, which again require independent wavelength control. This chapter describes the different laser sources used to trap both ^{85}Rb and ^{40}Ar*, and how they are locked using phase-sensitive detection to their respective saturation absorption spectrometers, within a few megahertz of their atomic transitions linewidth.

4.1 THE ^{85}Rb LASER SOURCE

^{85}Rb is trapped using the cycling transition $F = 3 \rightarrow F' = 4$ at a wavelength of 780 nm, as can be seen in the energy level diagram of Fig. 3.14. The transition is detuned by $\delta = -2\Gamma$ (12 MHz) to the red of the cycling transition. This transition was chosen because the atoms can only decay back down to the F=3 transition after which they are again available for re-excitation. Due to infrequent Raman scattering, some atoms end up in the F=2 state. In this new ground state level the atoms could not be re-excited, thus losing their ability to be trapped; as a result a second laser is necessary to repopulate the

F=3 level. This can be done by using the $F = 2 \rightarrow F' = 2$ or 3 transitions. From F'=2 or 3 the atom can decay back down to the F=3 level and is recycled for reuse in trapping. A laser that performs this function is referred to as the hyperfine repumper.

In this work a narrow-band tunable diode laser system with optical grating feedback in a master-slave configuration was used. The master laser was constructed with a Sanyo DL7140-201 (λ=785 nm, P=70 mW, anti-reflection (AR) coated) laser diode in the external cavity; sometimes called Littman-Metcalf configuration [133, 153-155]. The laser diode is mounted into a mounting block that is cooled by a Peltier thermo electric cooler that is in thermal contact with the mounting block and receives temperature feedback from a thermistor that is also mounted in the aluminum block. A lens mounted directly in front of the diode collimates the laser beam, which is projected onto an optical grating (Edmund Scientific NT43-848, gold plated, with a 1200-lines/mm vertically located). The output laser beam reflects specularly off the grating while the first-order diffracted beam is reflected back into the diode via a mirror in which horizontal orientation is controlled by a piezoelectric transducer (PZT) driver, Fig. 4.1. The diode's frequency is determined by adjusting the mirror position, to control laser light feedback back into the diode, the temperature of the diode, and the current that is supplied to the diode. To obtain the right wavelength for the trapping transition the right combination of all three settings has to be attained. In finding the right combination a laser diode can be tuned to within ~1 MHz of linewidth, running single mode, of an atomic resonance line.

Due to optical losses in the grating feedback system the laser power yielded by the laser is generally of the order of a 10 mW. Subtracting from that the power needed

for the saturation absorption system and additional optical losses incurred by optics and fiber coupling, only about 3 mW is available at the trap. This is sufficient to run an ^{85}Rb MOT, but for a dual species MOT a larger power requirement is needed. To accomplish this a master-slave configuration is used. This is done by injection locking the slave laser with the help of the master laser, by using a small amount of light that is split off the main master laser beam with a piece of glass and then fed into the slave laser [156]. The slave laser runs then at the same frequency as the master does, but without the losses incurred by the master. Power output from the slave is usually of the order of 40 mW giving an available power of about ~9 mW at the MOT. The slave is constructed the same way as the master, but without a feedback grating and mirror (Sanyo DL7140-201).

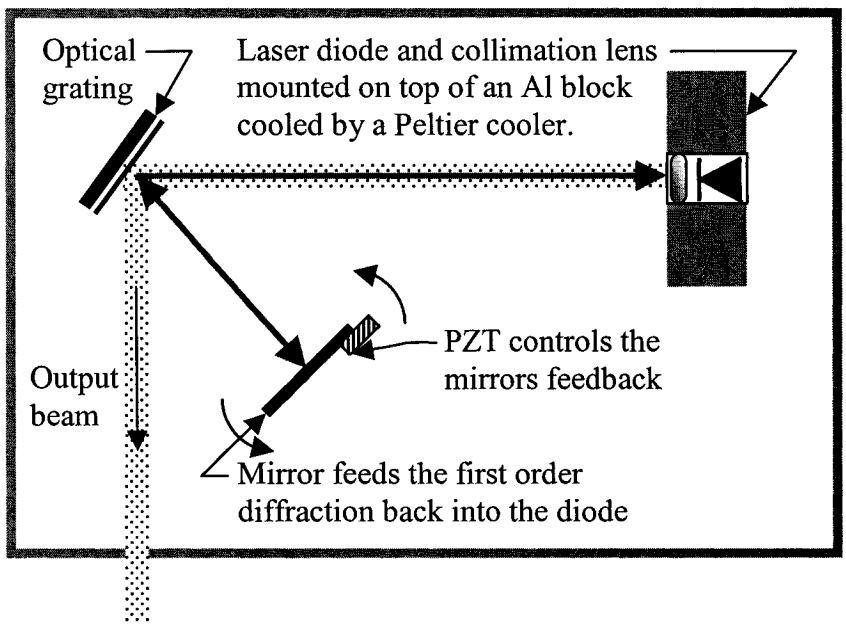

FIG. 4.1. Schematic of external cavity diode laser. External cavity laser diode setup and PZT feedback are shown as used for the Master laser.

Instead of building an additional laser for the hyperfine repumping transition, an alternative method is used. The excitation transition for $F = 2 \rightarrow F' = 3$ is about 3.1 GHz larger than that of the trapping transition. Therefore, the current of the diode of the trapping laser can be microwave modulated at 3.1 GHz to generate a sideband on the laser light that acts as a hyperfine repumper [157, 158]. This was done by modulating the slave laser diode current with a voltage-controlled oscillator (VCO) (Hewlett Packard VTO-8240) coupled to the diode with a bias-T junction (Mini Circuits ZFBT-6G) to create two sidebands with a 10% intensity of the fundamental frequency.

The laser is locked by phase-sensitive detection to a saturation absorption signal. The laser light of the main master laser beam is split off by a beam splitter or simple piece of glass and then sent through an acousto-optic modulator (AOM), which downshifts the light by 80 MHz before it is split again by a beam splitter into three beams, 2 weak and one strong, before being sent through an Rb vapor cell. The two weak beams that pass through the vapor cell are called the probe beams. The third strong beam which counter propagates relative to the probe beams in the vapor cell is called the pump beam, Fig. 4.2. Each of the two probe beams is partially reflected into a separate photodiode. The photodiodes are arranged into a parallel circuit with opposite polarity and the circuit then subtracts the two photodiode currents and gives the saturation absorption signal. To obtain a saturation absorption signal that has dips and peaks to which the laser can be locked requires the precise alignment of the pump beam with one of the probe beams in an overlapped orientation. There are several laser lock schemes available [159-161], one of them being where the pump beam is parallel overlapped with one of the probe beams [162]. When this method is used the laser is on resonance and

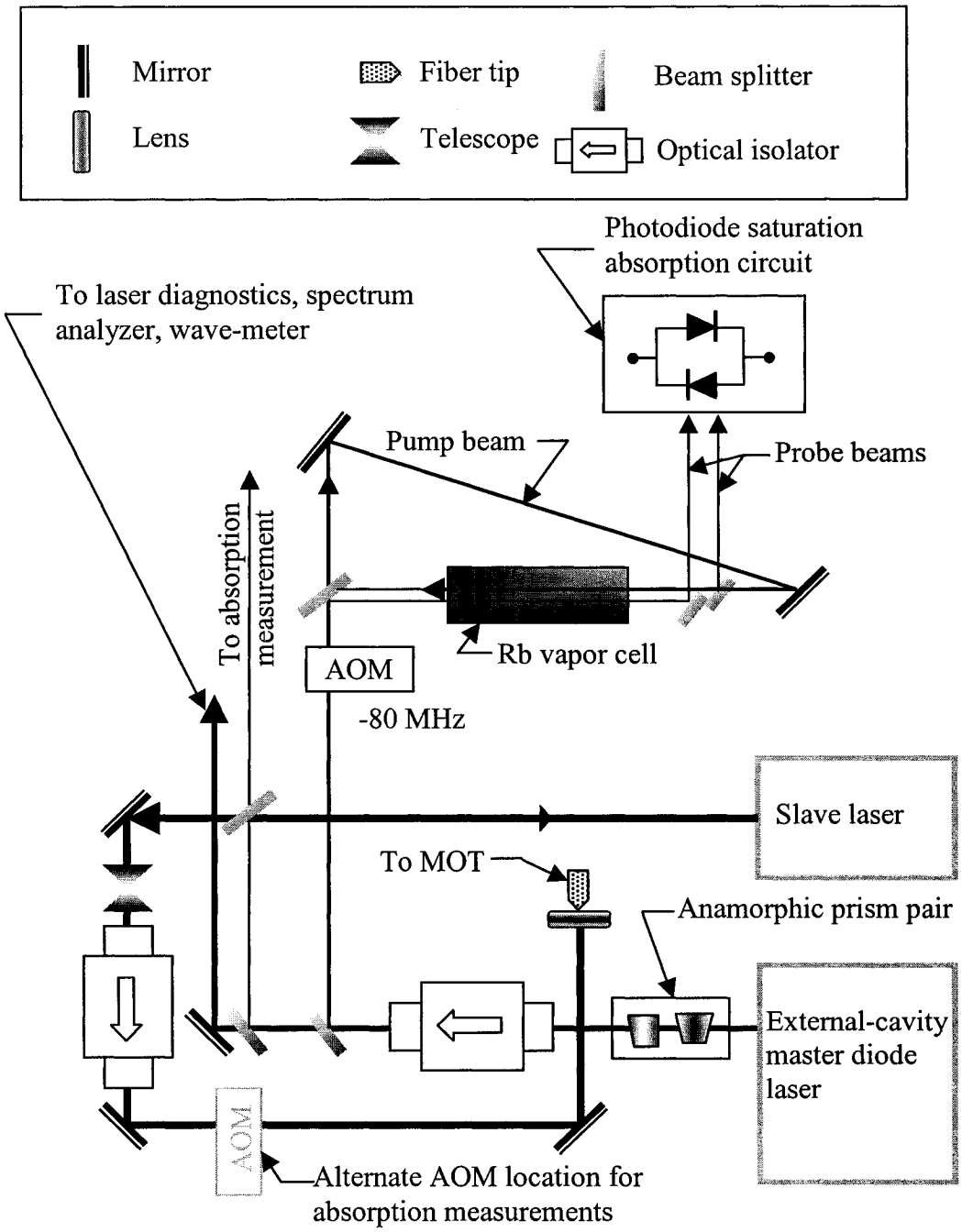

FIG. 4.2. Optical setup of ^{85}Rb master-slave diode laser system with saturation absorption spectrometer. The alternate AOM setup for absorption measurements is also shown. This setup delivers 6-9 mW to the MOT for trapping.

the probe and pump beam interact with the same group of atoms in the cell. This can be understood by considering that when the laser is not on resonance one beam will interact with atoms at parallel velocity component v_z, while the other beam will interact with atoms with velocity component $-v_z$. When the laser is on resonance both beams will interact with the same group of atoms with parallel velocity component $v_z \approx 0$, this results in a Doppler-free signal. The stronger pump beam depletes the atoms in the ground state F level, while the weaker probe beam then passes through the cell with reduced absorption. When this reduced absorbed probe beam is subtracted from the other probe beam, which acts as a reference beam, an absorption signal is observed as shown in Fig. 4.3 [153, 162].

The signal shown in Fig. 4.3 is obtained by scanning the laser with a PZT driven mirror over several hundred megahertz in the master laser external cavity configuration, Fig. 4.1. The actual laser is locked to one of the crossover peaks ($F = 3 \rightarrow F' = 2-4$), which occur when two atomic transitions share a common ground state and differ in frequency by less than a few Doppler linewidths. The pump beam then interacts with two different groups of atoms simultaneously causing the extra absorption peaks. This can be understood by considering that the probe beam will interact with one group of atoms at $-v_{z1}$ red shifted from one transition ($F = 3 \rightarrow F' = 4$) while at the same time it interacts with a group of atoms from a different transition ($F = 3 \rightarrow F' = 3$) at $+v_{z2}$ blue shifting them. This causes a reduction in the ground state population ($F = 3$) and results in more intense crossover peaks. Crossover peaks occur halfway between any two allowed transitions. The AOM in the saturation absorption setup shifts the laser light down by 80

MHz, which then allows the laser to be locked to the third peak as shown in Fig. 4.3. The laser then is running at an actual trapping frequency of two natural linewidths detuned to the red of the $F = 3 \rightarrow F' = 4$ trapping transition. A note to the absorption signal of Fig. 4.3 is that the actual width and height of the peaks and dips depends upon the probe beam's alignment into the photodiodes, beam intensity, electronic damping constants, and absorption cell pressure.

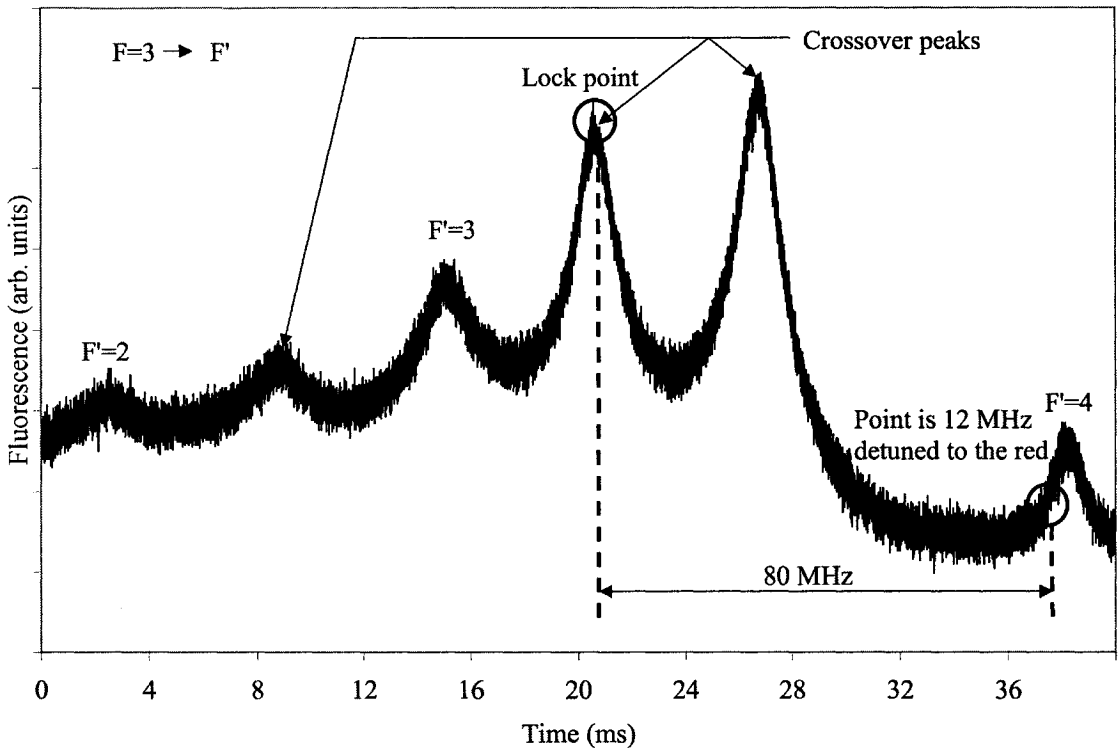

FIG. 4.3. ^{85}Rb absorption signal as used to lock the laser for trapping. Crossover peaks, lock point, and trapping transition are clearly shown.

Some other important optical components shown in Fig. 4.2 are the anamorphic prism pair and the optical isolators. As the laser beam leaves the master laser it is

elliptical in shape. The anamorphic prism pair then converts this beam into a circular beam. Following its change in shape the beam passes through an optical isolator, which prevents any optical feedback from the slave laser from being fed back to the master laser. A second isolator, which provides 45 dB of attenuation, is also fitted to the slave laser fiber pick-up to prevent feedback into the slave from the fiber tip even with a angle polished connector (APC) tip. Any feedback into the lasers can cause laser instability and prevent the laser from being pulled to the desired frequency.

For absorption measurements the saturation absorption AOM is moved to the slave fiber pick-up where it can act as a optical switch to turn the trap light on and off in about a 100 ns, Fig. 4.2.

The electronic components flowchart for the locking circuit used to lock the lasers is given in Fig. 4.4. The lock-in amplifier generates a phase sensitive derivative signal of the saturation absorption signal to which, at the zero crossing of the desired lock peak, the laser is locked. The modulation to obtain an error signal is a 10 kHz sine wave, which is added to the laser current. Feedback is provided by the saturation absorption signal and the laser is corrected through the lock box that is driven by a ramp. The lock box corrects the laser by controlling the PZT. The PZT in its turn drives the mirror adjusting the grating feedback in the master laser.

To determine the wavelength of the laser, a Burleigh WA-1000 wavemeter was used, this wavemeter has an accuracy to within ±0.3 ppm. Laser power was measured with a Coherent LaserMate-Q, which has an accuracy of to within 3.5% of the displayed reading. To determine if the laser was running single or multimode a Burgleigh SA^{Plus} laser spectrum analyzer system was used, this system included the interferometer SA-91,

the ramp RG-91 and detector amplifier DA-100. The Burleigh system had a free spectral range (FSR) of 2 GHz and a finesse of 200. Data was recorded with a four-channel Tektronix TDS-3034B digital oscilloscope.

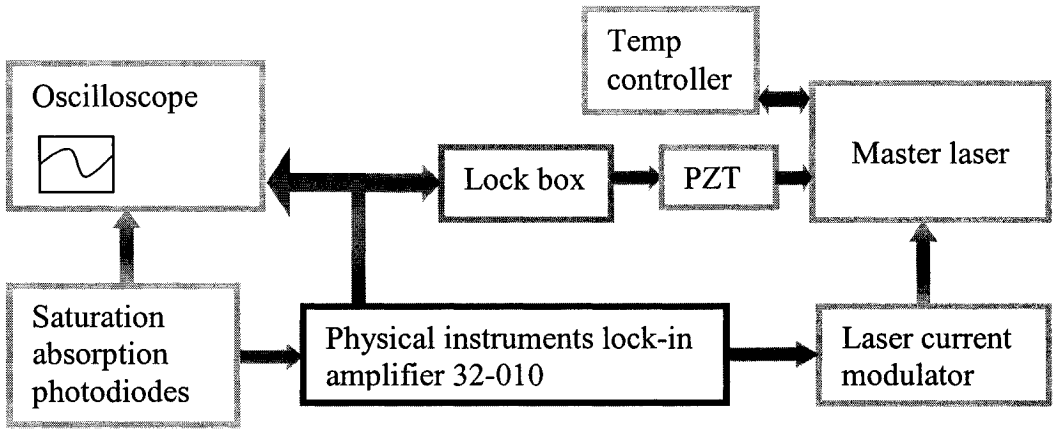

FIG. 4.4. Flow chart of ^{85}Rb laser locking circuit with feedback. The laser current is being modulated at 10 kHz.

4.2 THE ^{40}Ar* LASER SOURCE

In trapping ^{40}Ar* only one laser light source is required since ^{40}Ar* does not have a hyperfine structure and therefore does not require a hyperfine repumper. This somewhat simplifies the number of lasers needed, but it is offset by the power requirements that one laser has to fulfill; since to trap ^{40}Ar* a Zeeman slower beam is also required in addition to the MOT beam. To accomplish this a Coherent 899-01 Ti:sapphire laser is used. The Ti:sapphire is pumped by an Coherent Argon Ion laser (Innova 300C) at 6 W. To obtain the narrow bandwidth (~1 MHz of linewidth) required for cooling and trapping a Coherent 895 etalon assembly is utilized. The laser is scanned and controlled in the same manner as the Rb laser: with a piezoelectric driven mirror

(tweeter), the tweeter is able to scan one cavity mode of 200 MHz. With this tweeter the laser is locked through a phase-sensitive detection scheme. Typical Ti:sapphire laser power outputs for on-resonance operation is of the order of 250 mW. In day-to-day operations walk off losses of the thick etalon are strongly ambient temperature dependent, since small changes in temperature affects the cavity length. This is the main source of Ti:sapphire laser power loss. With minimal walk off, on-resonance Ti:sapphire power can be as high as 380 mW. This power is split between the MOT beams and a Zeeman slower beam. A small fraction of the main beam goes to the saturation absorption spectrometer and to a diagnostic fiber pick up. The power delivered to the MOT is typically 30-50 mW and to the Zeeman slower it is 40-50 mW.

The Ti:sapphire optical arrangement is shown in Fig. 4.5. As the beam leaves the laser a small portion of it is split off and sent to the saturation absorption spectrometer and to a wave-meter for beam diagnostics. After that a 50/50 beam splitter distributes the light evenly between the MOT and Zeeman slower. The saturation absorption signal of $^{40}Ar^*$ is similar to that shown in Fig. 3.8, with only one peak to lock to. Therefore, to lock the laser at a detuning of $\delta = -(1.5)\Gamma$ (9 MHz) to the red of the cycling transition, which is necessary for optimal trap operation, several AOMs have to be used. The first AOM in the saturation absorption setup is +80 MHz, causing the laser to run –80 MHz to the red, a second AOM up shifts the MOT beam by +71 MHz, resulting in the desired trap light detuning of 9 MHz to the red of the cooling resonance transition. The Zeeman slower operates at a detuning of 160 MHz to the red of the cooling transition, so a third AOM therefore shifts the Zeeman beam down by –80 MHz for the total desired detuning of 160 MHz.

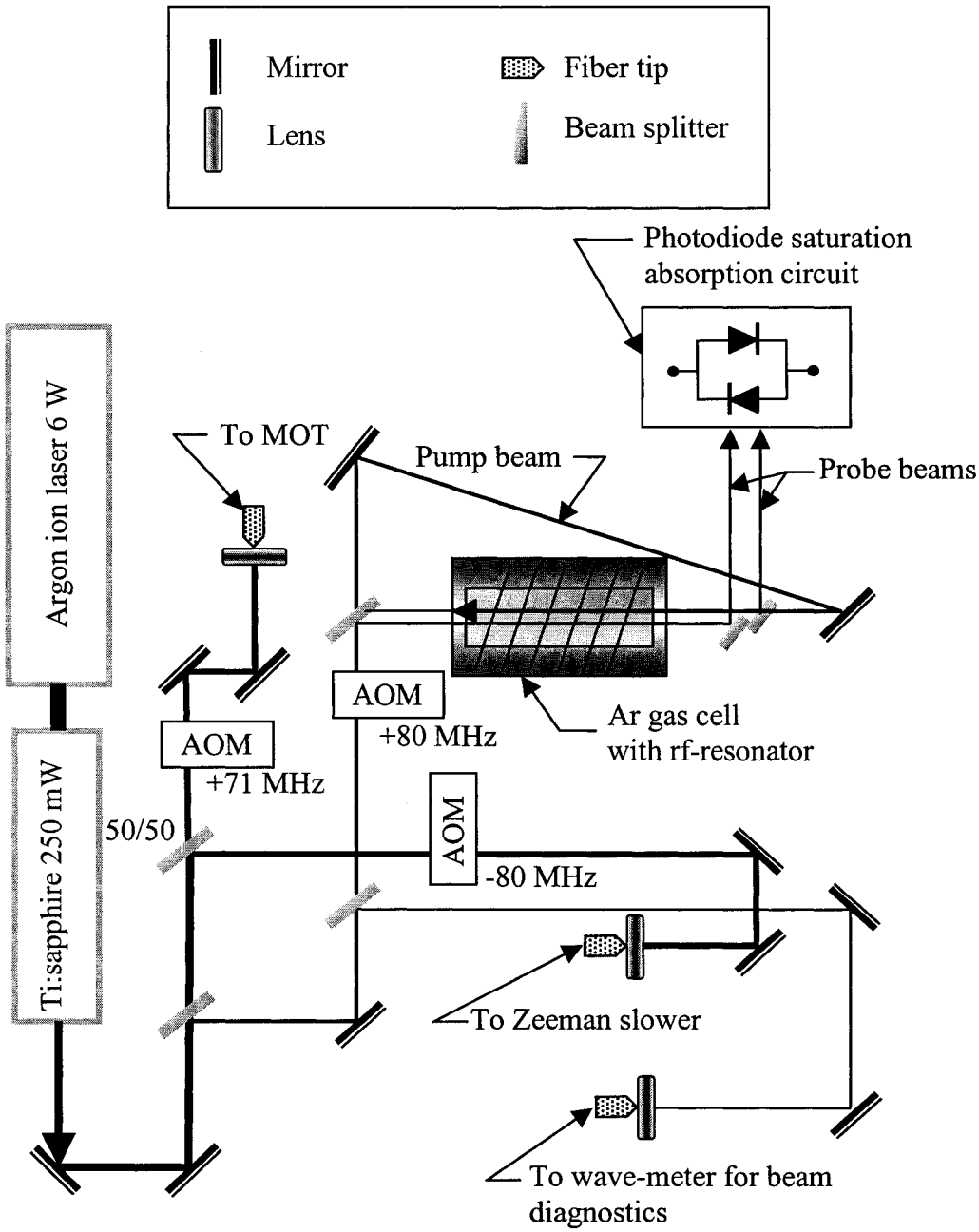

FIG. 4.5. Ti:sapphire laser optical setup as used for the trapping and slowing of $^{40}Ar^*$.

The saturation absorption setup is similar to that used for Rb, with the distinction that the Ar cell is operated in an rf discharge and filled with research grade Ar gas at 10 mTorr; the cell was constructed in-house as reported in Ref. [163]. The rf resonator was constructed in the same fashion and operated with the same parameters as that shown in Fig. 3.3 and Fig. 3.5 and explained in the accompanying text. The dimensions of Fig. 3.3 for the discharge cell differ from those of discharge source of Chapter 3 and are as follows: D=7.5 cm, d=4 cm, b=5.7 cm, the number of windings of the copper coil is N=15.

In locking the Ti:sapphire laser it was observed that the laser was susceptible to acoustic noise of approximately 15 Hz, which the locking loop was not able to filter out, as indicated in Fig. 4.6. This was mainly due to the fact that the 899-01 laser does not have a reference cavity to which it is locked. This effect would manifest itself in trap fluorescence jitter since the laser frequency was oscillating in the range of the natural linewidth of the atom (fluctuations > 6 MHz). To obtain a good laser lock, fluctuations should be less than 1 MHz. To remedy this situation a reference cavity (Fabry-Perot etalon) from a Coherent dye laser 699-21, with a free spectral range of 1 GHz and a bandwidth of 350 MHz, was borrowed from Prof. L. Vuskovic and fitted to the Ti:sapphire laser. Two small laser beams were split off the Ti:sapphire's main laser beam, one was used as a reference beam and passed through a neutral density filter to attenuate it before it impinged onto a photodiode, while the other beam was sent through the reference cavity before it was directed onto its respective photodiode. This produced an error signal to which the Ti:sapphire laser's PZT could be locked. By providing feedback through the reference cavity galvanometer the reference cavity was then locked

to the lasers $^{40}Ar^*$ saturation absorption signal, Fig. 4.7. A new electronic circuit had to be designed to complete the task of driving the reference cavity galvanometer and obtaining an error signal from the Ti:sapphire laser's two photodiodes to which the laser could be locked [164, 165], Fig. 4.8. With this new setup the instrumentation needed to lock the laser had to be modified from the locking scheme used when locking ^{85}Rb. The new locking method flowchart schematic is summarized in Fig. 4.7. With this laser locking modification scheme the noise was significantly removed from the laser and the laser could be locked in a stable manner.

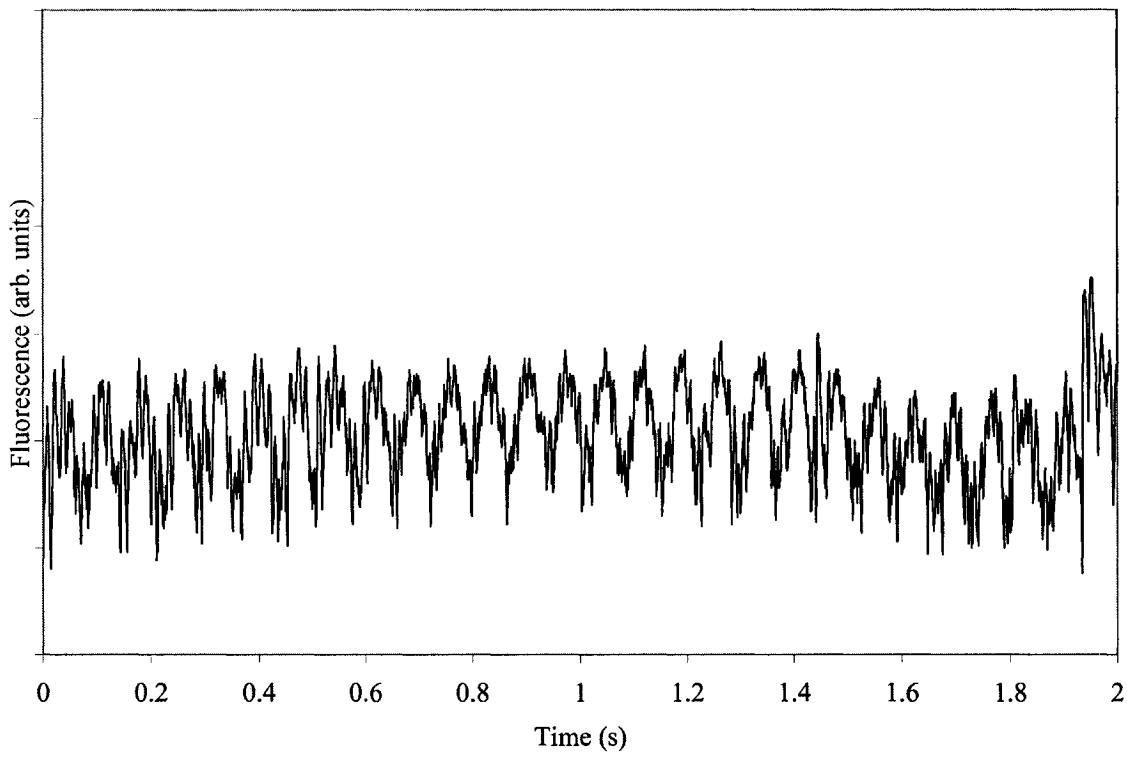

FIG. 4.6. Ti:sapphire laser acoustic noise fluctuations. Those fluctuations caused frequency instability in locking the laser to the natural linewidth of the atom.

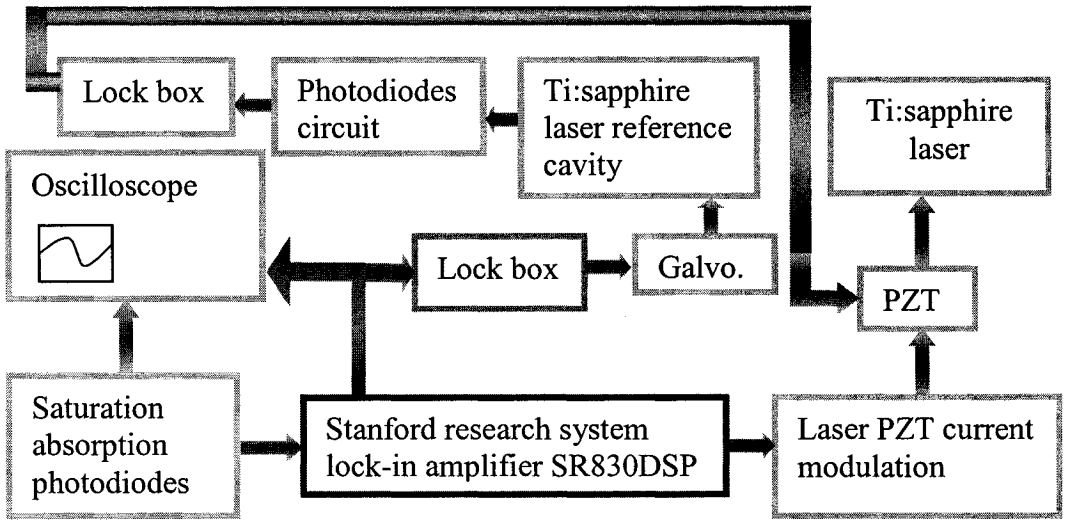

FIG. 4.7. Flow chart of $^{40}Ar^*$ laser locking scheme. The laser PZT current was modulated with a 10 kHz sine wave.

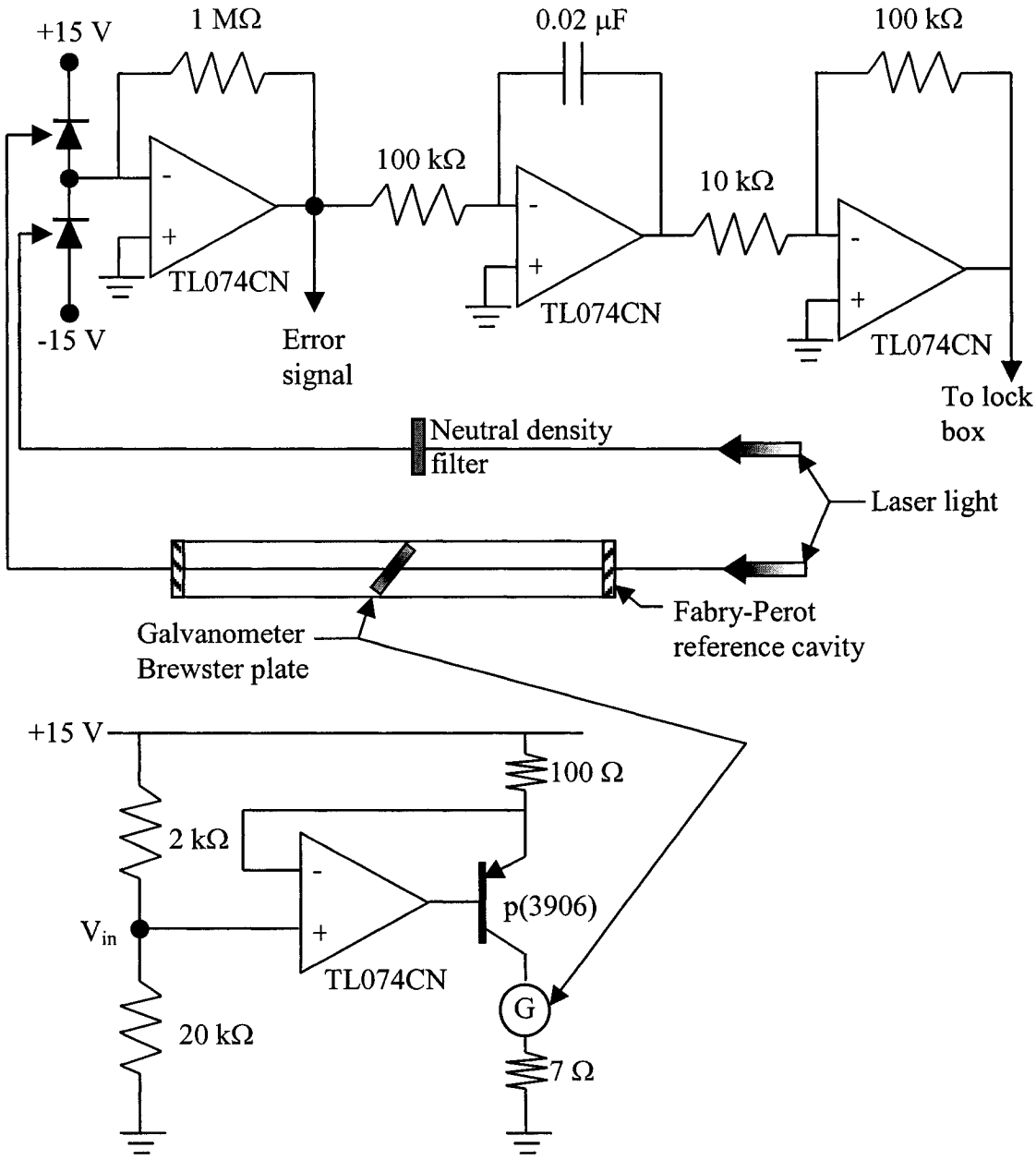

FIG. 4.8. Circuit designed to stabilize the Ti:sapphire laser. It drives a glass plate mounted on a galvanometer and produces an error signal from two photodiodes to which the laser could be locked.

4.3 FLUORESCENCE MEASUREMENTS AND ABSORPTION IMAGING

The number of atoms in a MOT can be determined by two methods, one method uses fluorescence measurements and the other uses absorption imaging.

As a trapped atom decays back from its excited state to its ground state, it emits a photon (fluorescence). As this photon impinges on a photomultiplier tube (PMT) it generates a current by releasing an electron. In dividing the current by the charge of one electron, quantum efficiency of the PMT, gain of the PMT, solid angle, and window losses, a relation can be obtained that relates the current of the PMT to the photons scattered by the MOT. (The PMT used was an uncalibrated PMT.) To obtain the total scattering rate of the MOT Γ_{pMOT}, the losses due to MOT windows and lenses (8%), interference filters (50%), aperture (75%), beam splitter (Rb 35%/Ar 65%), and solid angle of the PMT port have to be multiplied into the final scattering rate obtained from the PMT. Fig. 4.9 shows a typical dual MOT fluorescence observation setup. By rewriting Eq. (2-10) for many atoms

$$\Gamma_{pMOT} = \Gamma \rho_{ee} N_{MOT}, \tag{4-1}$$

the number of atoms N_{MOT} in the MOT can then be extracted. To find the density in the MOT two limiting regimes have to be considered, the low and high-density regime. In the low-density regime the MOT's spatial density distribution is of the Gaussian form while in the high-density limit the MOT loading takes place at a constant density and the spatial distribution has the shape of a top hat, as depicted in Fig. 4.10.

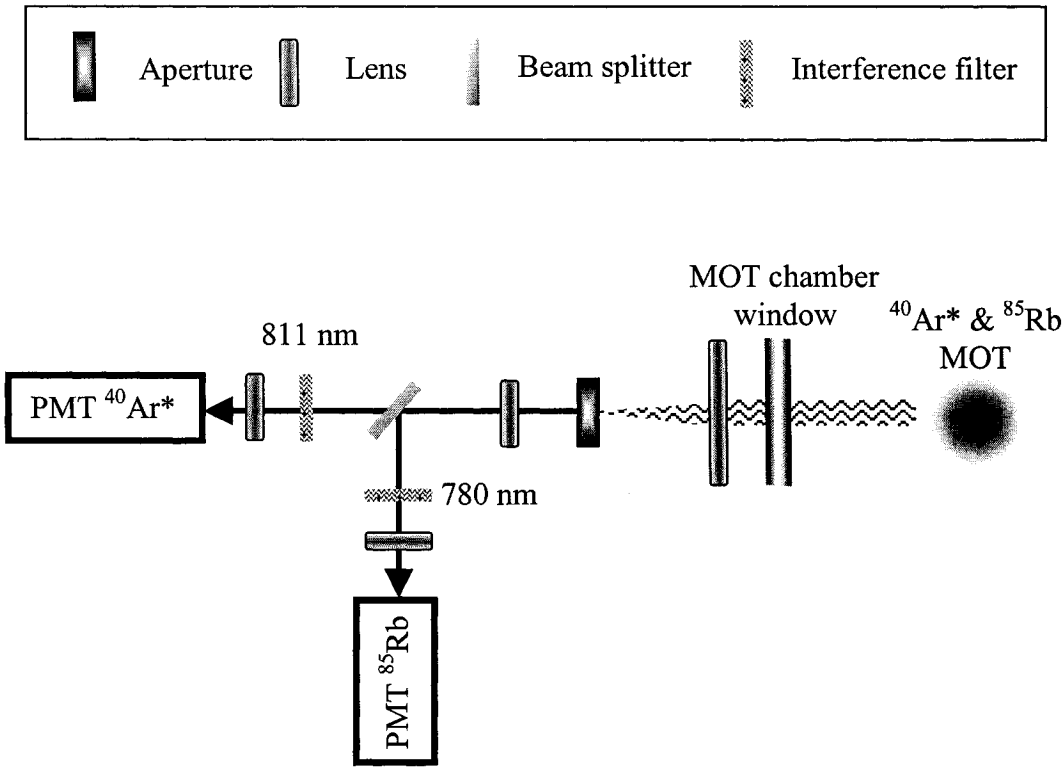

FIG. 4.9. A typical dual MOT fluorescence experimental PMT setup. This setup allows the simultaneous observation of ^{40}Ar* and ^{85}Rb fluorescence when confined in dual MOT.

Fig. 4.10 shows the fluorescence of a ^{85}Rb MOT with no ^{40}Ar background, as measured by a PMT. This profile is of the low-density limit regime and can be matched to that of a Gaussian density distribution

$$n_{Rb}(\vec{r},t) = n_0(t)e^{-(r^2/a^2)}. \qquad (4\text{-}2)$$

Where n_0 is the peak Gaussian density and a is the $1/e$ Gaussian radius determined from a Apogee CCD camera. Since the fluorescence is of an approximate Gaussian profile the number of atoms in the MOT can be obtained by integrating the density over the

spherical volume of the MOT to give an expression

$$n_0 = \frac{N_{MOT}}{\pi^{3/2} a^3}, \tag{4-3}$$

for the peak Gaussian density.

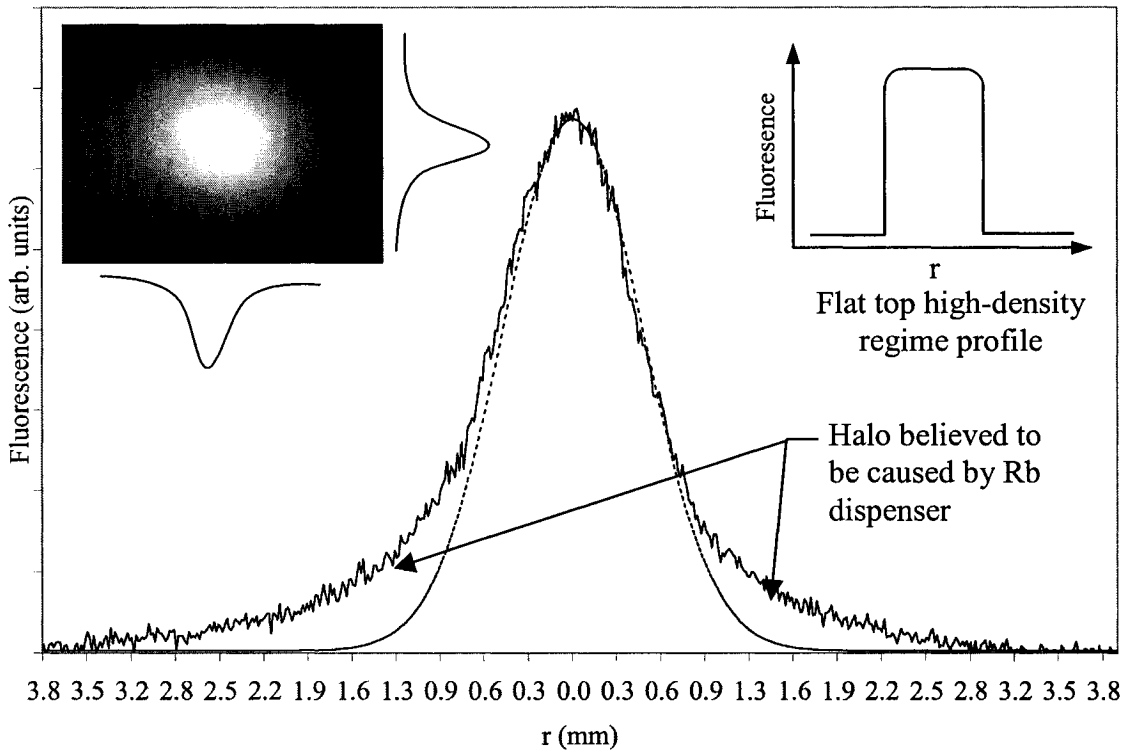

FIG. 4.10. A typical radial Gaussian ^{85}Rb trap density distribution. The dotted line is the Gaussian curve fit of Eq. (4-2). This trap is a ^{85}Rb trap with no ^{40}Ar background gas influence. Left insert shows a CCD image of a cloud of trapped atoms. Right insert depicts how a MOT fluorescence signal would look like in the high-density limit.

In Fig. 4.10 it can also be observed that the tail ends of the Gaussian fluorescence distribution are slightly larger than the direct Gaussian fit. This is believed to be caused by the Rb Getter dispenser, the dispenser expels the Rb vapor directly on axis with the

MOT, this Rb wind creates a halo around the MOT.

An alternate method for measuring trap density and the number of trapped atoms is the absorption imaging method. The absorption imaging method uses an additional resonant trap laser beam that passes through the cloud of trapped atoms and then projects onto a CCD camera. The absorption beam is much larger in size than the trap and is of low laser intensity $I \sim 10^{-3} I_s$. As the absorption beam passes through the resonant trapped atoms the trapped atoms absorb it, resulting in a loss of intensity of the beam when it reaches the CCD camera. Beer's law defines the absorption rate of the trapped atoms as follows

$$\frac{dI}{dz} = -\sigma_{eg} n I, \tag{4-4}$$

where σ_{eg} is the cross section for absorption, n is the Gaussian density distribution, and z is a spatial variable in the z-direction. Solving Eq. (4-4) gives

$$I(z) = I_0 e^{-OD}, \tag{4-5}$$

where

$$OD = \int n \sigma_{eg} dz. \tag{4-6}$$

I_0 is the intensity of the absorption beam without the trap, and OD is the optical density of the trap. By determining the OD profile of the trap we can determine the density distribution of the trap from which we can again integrate over the trap volume to determine the number of trapped atoms [131, 132, 166-171].

The OD is obtained by taking three CCD camera still frames. The first frame is a background frame without trap light and absorption beam present. This frame is used to subtract the background noise out of the absorption images (I_{BACK}). The second frame is

a CCD image of the absorption beam without any trap light present (I_{ABS}). The third and final frame is a CCD image with both absorption beam and trap present ($I_{MOT/ABS}$) where the trap light beams are turned off a fraction of a second before the absorption image was taken. The *OD* is obtained as follows by using Eq. (4-5) to give

$$OD = \ln\left(\frac{I_{ABS} - I_{BACK}}{I_{MOT/ABS} - I_{BACK}}\right). \tag{4-7}$$

A typical absorption image is shown in Fig. 4.11 with its respective *OD* profile. During absorption measurements the MOT beams are switched off with the aid of an AOM as the CCD camera takes its picture. The AOM is connected to a TTL triggered switch that can switch the MOT light of in about 100 ns, as shown in Fig. 4.2. By turning the MOT beams off as the CCD picture is taken there is less fluorescence background scattered light influence from the MOT beams on the image. The absorption imaging technique was used to compare the number of trapped atoms with those of the fluorescence measurements, which agreed with each other within a factor of two, which is typical.

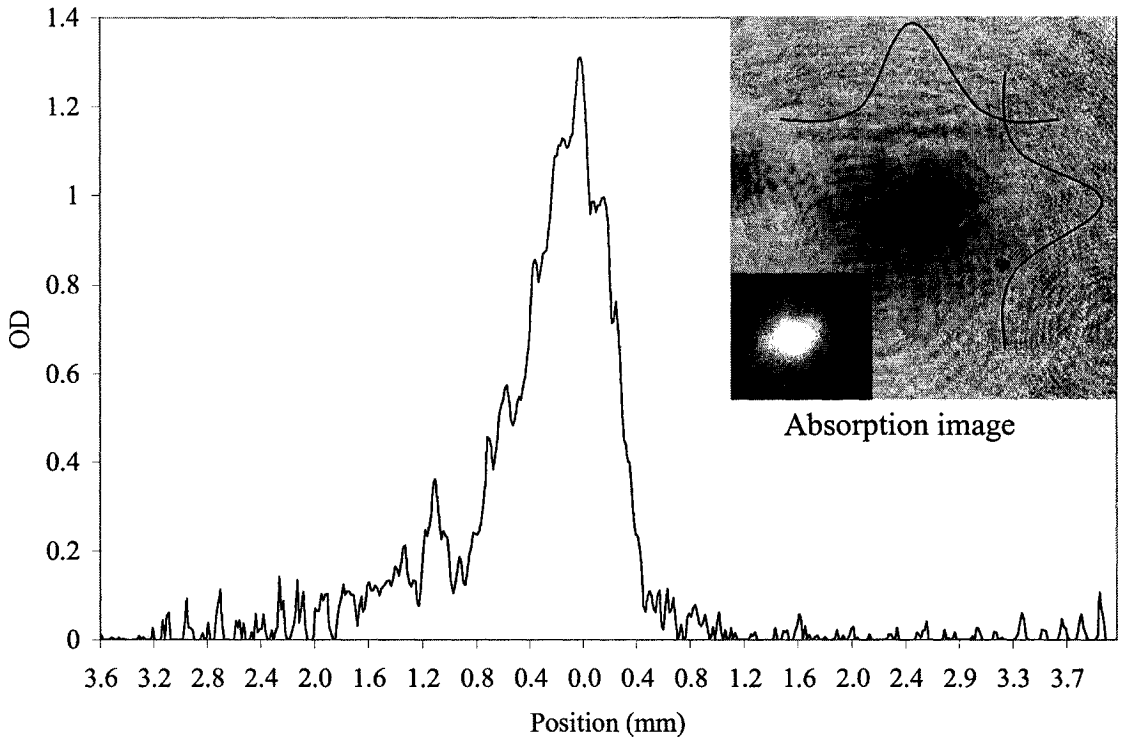

FIG. 4.11. A typical *OD* profile of a ^{85}Rb MOT. Large insert shows the respective absorption image as taken by a CCD camera. (Small insert shows an inverted absorption image).

CHAPTER V

DETERMINATION OF TRAP LOSS RATE COEFFICIENTS

Both alkali-metal and metastable noble gas traps are subject to trap loss due to atomic collisions. The collisional losses are caused by a combination of atomic room temperature atoms colliding with the trapped atomic species and with interatomic collisions between trapped atoms. Either collision can result in trap loss, which manifests itself in the release of kinetic energy to the atoms, and the loss of one or more atoms from the trap. The loss of those atoms can be measured by observing the fluorescence change in the loading and decay curves of the trapped atoms. From this, trap loss rate coefficients can be extracted which are distinctive to each individual trapped species and states of the atoms.

5.1 TRAP LOADING RATE EQUATION

For a single species trap, the equation governing the number of atoms in the trap as a function of time is:

$$\frac{dN_{Atom}}{dt} = L_{Atom} - \alpha_{Atom} N_{Atom} - \beta_{Atom} \int_V n_{Atom}^2(\vec{r},t) d^3r . \qquad (5\text{-}1)$$

Where N_{Atom} is the total number of atoms in the trap, n_{Atom} is the trap density distribution, and L_{Atom} is the atomic loading rate from a background vapor in the case of Rb, or the atomic capture rate from an atomic beam in the case of Ar. The linear loss rate coefficient is represented by α_{Atom}. This is the loss rate coefficient that is responsible for

the accounting of the thermal background atoms interacting with the trapped atoms and is independent of the number of trapped atoms. (The background gas is usually composed of some He, N_2, and primarily thermal Rb atoms, and in the case of the presence of the Ar* beam also thermal Ar*/Ar atoms.) The density dependent losses are defined by β_{Atom}, which is the loss-rate coefficient due to inelastic (exoergic) collisions between trapped atoms. Such collisions can be a composition of various combinations of two body-collisions and result in enough transfer of kinetic energy to the atoms that both atoms are ejected from the trap. (At typical MOT densities three body collisions are too small to be of significance and are ignored in this analysis.)

For Rb the loss rate coefficient can be written as follows

$$\beta_{Rb} = \beta_{RE} + \beta_{FS} + \beta_{HFS}. \qquad (5\text{-}2)$$

Where RE is the contribution from radiative escape, which occurs when one of two atoms is excited with respect toward the other atom and the atom pair is then accelerated on the long range ($V \sim 1/R^3$) potential toward each other. During that acceleration sudden spontaneous emission of a photon, different from the excitation photon, can occur. The difference in the absorbed and emitted photon energy is then created and converted to external kinetic energy Eq. (5-3). When the kinetic energy is larger than the trap depth both atoms are ejected, Fig. 5.1. The FS interaction stands for fine structure changing collisions. In this type of interaction one atom again is in the excited state and goes up into the $5^2P_{3/2}$ state and is transferred in to the $5^2P_{1/2}$ state due to a collision with a ground state atom, Eq. (5-4). Again, the energy released is converted to kinetic energy and since it is larger than the trap depth for Rb, both atoms are ejected from the trap, Fig. 5.1. Both the RE and FS processes are the dominant trap loss mechanisms in the high intensity

regime. (For ^{85}Rb the β_{FS} is about (4±2)% of the total β_{Rb} trap loss [180].) At low intensity another mechanism is also of significance, this is the hyperfine structure HFS changing collision. Since at low intensity most Rb atoms are predominantly in the ground state, this collision occurs between ground state atoms, Eq. (5-5). (Most atoms will be in the upper hyperfine

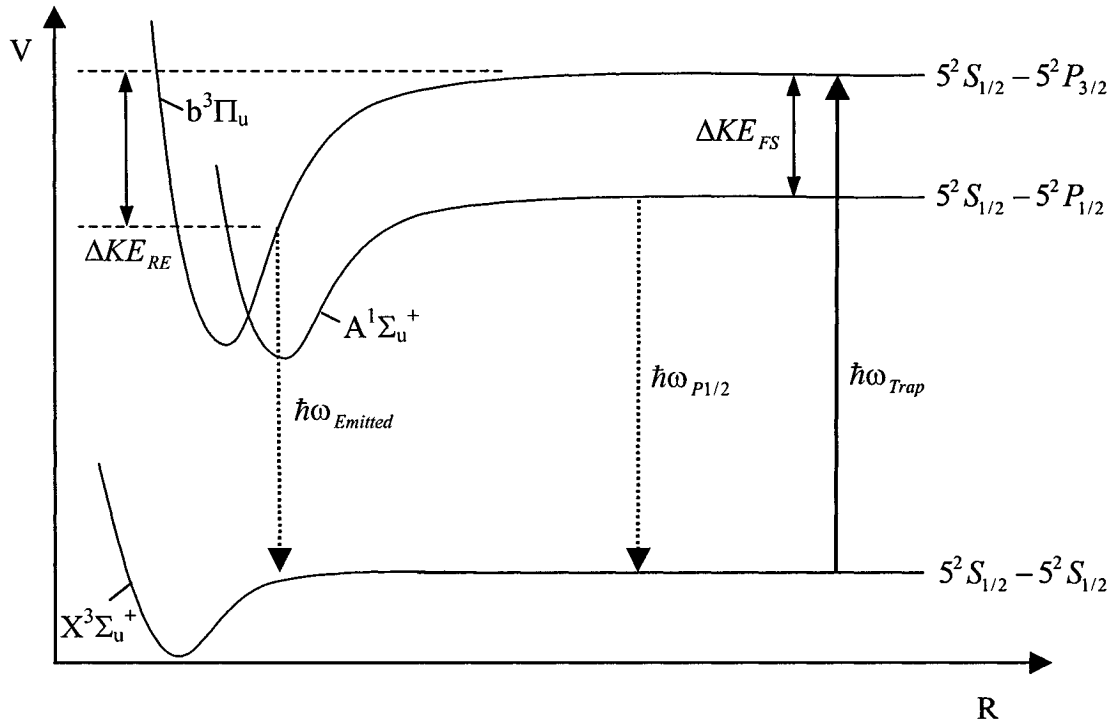

FIG. 5.1. Diagram of the RE and FS trap loss mechanisms. In either case the energy released is sufficient to cause trap loss. (T_c=222.1 mK for ^{85}Rb.)

ground state, F=3 for Rb.) Both Rb atoms in the F=3 state are knocked down to the F=2 state and again the release of energy is sufficient to release the two atoms from a much shallower low intensity trap. It is also possible that one atom is already in the F=2 state

and the other in the F=3 state, Eq. (5-6), thus only one atom is moved down to the F=2 and the release energy is half that of the previous reaction. Those cases are summarized as follows:

$$\begin{aligned} &Rb(5^2S_{1/2}) + Rb(5^2S_{1/2}) + \hbar\omega_{Trap} \rightarrow Rb_2(5^2S_{1/2} + 5^2P_{3/2}) \\ &\rightarrow Rb(5^2S_{1/2}) + Rb(5^2S_{1/2}) + \Delta KE_{RE} + \hbar\omega_{Emitted} \end{aligned}, \tag{5-3}$$

$$\begin{aligned} &Rb(5^2S_{1/2}) + Rb(5^2S_{1/2}) + \hbar\omega_{Trap} \rightarrow Rb_2(5^2S_{1/2} + 5^2P_{3/2}) \\ &\rightarrow Rb_2(5^2S_{1/2} + 5^2P_{1/2}) \\ &\rightarrow Rb(5^2S_{1/2}) + Rb(5^2S_{1/2}) + \Delta KE_{FS} + \hbar\omega_{P1/2} \end{aligned}, \tag{5-4}$$

$$\begin{aligned} &Rb(5^2S_{1/2}, F=3) + Rb(5^2S_{1/2}, F=3) \rightarrow \\ &Rb(5^2S_{1/2}, F=2) + Rb(5^2S_{1/2}, F=2) + \Delta KE_{HFC} \end{aligned}, \tag{5-5}$$

$$\begin{aligned} &Rb(5^2S_{1/2}, F=3) + Rb(5^2S_{1/2}, F=2) \rightarrow \\ &Rb(5^2S_{1/2}, F=2) + Rb(5^2S_{1/2}, F=2) + \Delta KE_{HFC}/2 \end{aligned}. \tag{5-6}$$

For a metastable rare-gas trap, such as Ar*, Eq. (5-1) also applies. Metastable rare-gas atoms have a larger initial energy, therby opening the ionization channel. For even isotopes the noble gases do not have a hyperfine structure, which simplifies the density dependent loss rate coefficient β_{Ar}, to

$$\beta_{Ar} = \beta_{NI} + \beta_I . \tag{5-7}$$

Where β_{NI} is the loss rate to non-ionizing inelastic atomic collisions, and β_I is the loss rate caused by ionizing collisions. Ionizing trap collisions can take place through two unique channels for metastable gases; the more dominant mechanism is Penning ionization (PI) Eq. (5-8), in which two metastable atoms collide to produce an ion and a ground state Ar atom, Fig. 5.2. The second mechanism is associative ionization (AI) Eq. (5-9). In this process a molecular ion is formed which contains some of the internal energy in the form of vibrational energy (The electron is carrying off the majority of the

energy.), Fig. 5.2 [131]. These reactions can be written as follows:

$$Ar^*(4^2P_2) + Ar^*(4^2P_2) \rightarrow Ar(^1S_0) + Ar^+ + e^-, \quad (5\text{-}8)$$

$$Ar^*(4^2P_2) + Ar^*(4^2P_2) \rightarrow Ar_2^+ + e^-. \quad (5\text{-}9)$$

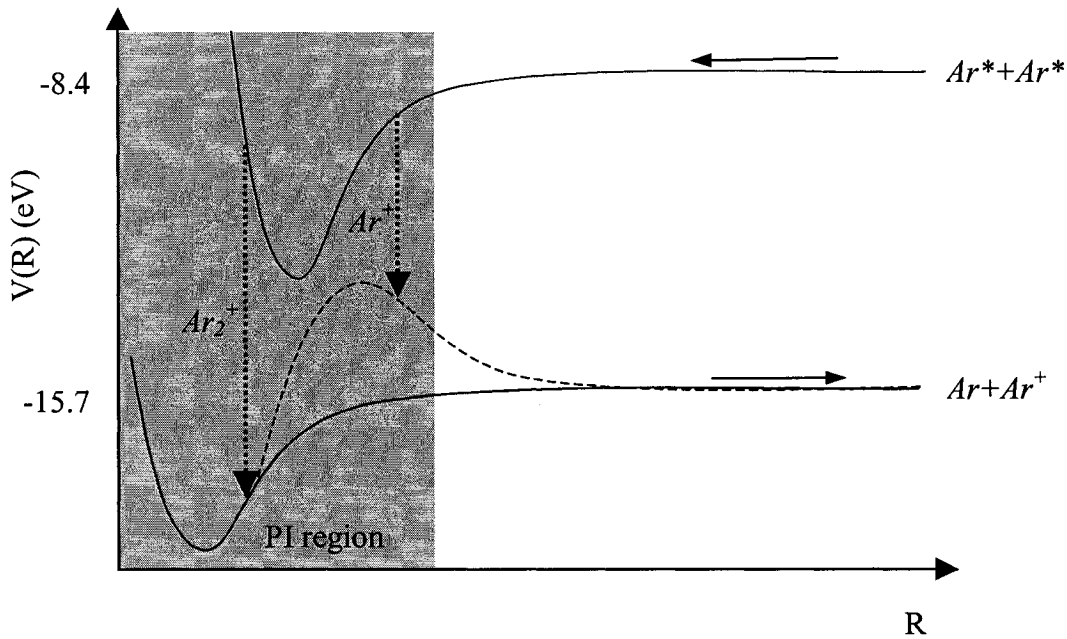

FIG. 5.2. Schematic of the PI and AI process as a function of interatomic separation.

In general PI is of order ten times larger than the AI process. As for other metastable traps the ionization rates limit the MOT density, but the ion byproducts allow for a means to be conveniently detectible [132]. Since it is possible to count the ion production with high accuracy using a channel electron multiplier (CEM) an ion load rate equation can also be defined [172-175] as

$$\frac{dI_{Ar}}{dt} = \alpha_I I_{Ar} + \frac{\beta_I}{2} \int_V n_{Ar}^2(\vec{r},t) d^3r. \quad (5\text{-}10)$$

Where α_I is the linear loss rate coefficient, which arises like its Rb counterpart from

losses due to background gas collisions. The factor of 1/2 is due to the fact that during PI and AI processes each ion counted results in two atoms being ejected from the trap.

5.2 SOLUTIONS TO THE TRAP LOAD RATE EQUATION

In solving Eq. (5-1) an integration over the volume of the spatial variation of the trap density is necessary. This can be simplified if the spatial density distribution of the trap is in one of two possible limits [5]. Those limits being the low and high-density regimes.

In the high-density limit, when radiation trapping is strong, trap loading proceeds at a constant density. This happens when the number of atoms increases with an expanding volume so that the density remains unchanged. In this regime the spatial density distribution can be defined by $n_{Rb}(r,t)=n_c$, where n_c is the constant atomic density in the trap [176, 177]. In that case Eq. (5-1) can be rewritten for Rb loading as follows

$$\frac{dN_{Rb}}{dt} = L_{Rb} - (\alpha_{Rb} + \beta_{Rb})N_{Rb}. \tag{5-11}$$

Eq. (5-11) can be solved directly to yield

$$N_{Rb}(t) = N_0(1 - e^{-t/\tau_L}) \tag{5-12}$$

where N_0 is the steady state number of trapped atoms and

$$\tau_L = \frac{1}{\alpha_{Rb} + \beta_{Rb} n_c} \tag{5-13}$$

is the loading time of the trap. The loading time is generally obtained by curve fitting the fluorescence obtained from a photomultiplier tube (PMT) or photodiode during the loading process of the trap from empty to a steady state value. The value of α_{Rb} can be

obtained by loading the trap in a low-density regime, where the term $\beta_{Rb}n_c$ is sufficiently small so as to be negligible. This occurs when the trap is operated in a regime where the trap intensity or magnetic field is very low or the trap is sufficiently detuned so that background collisions dominate the trap loss mechanism, as shown in Fig. 5.3. Once α_{Rb} is obtained β_{Rb} can be extracted from loading curves with constant density loading curves [178].

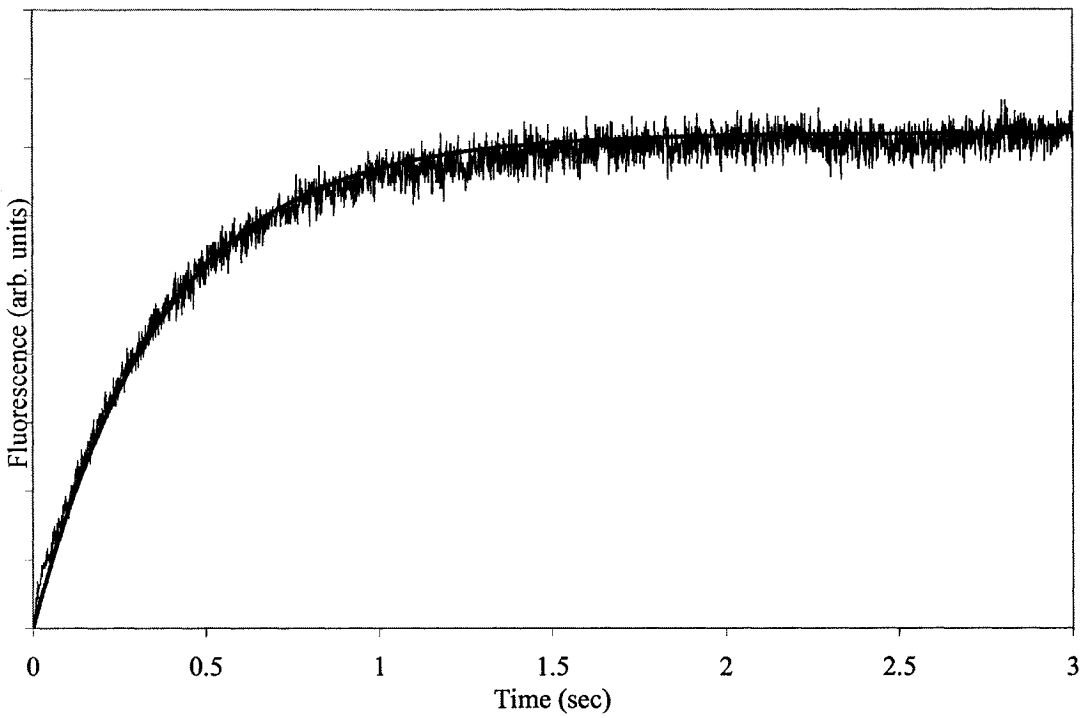

FIG. 5.3. A typical Rb loading curve in the presence of an Ar background. This curve represents Rb in a regime where background collisions dominate. The dark curve is fitted to Eq. (5-12) with a loading time of τ_L=0.38 sec and α_{Rb}=2.63/s.

In the low density limit radiation trapping is negligible and the trap's spatial distribution can be closely approximated as Gaussian, Fig 4.10. The density distribution

can then be expressed as

$$n_{Rb}(\vec{r},t) = n_0(t)e^{-(r^2/a^2)}. \tag{5-14}$$

Where a is defined as the $1/e$ Gaussian radius and n_0 is the peak trap density. Substituting Eq. (5-14) into Eq. (5-1) we then get

$$\frac{dN_{Rb}}{dt} = L_{Rb} - \alpha_{Rb}N_{Rb} - \frac{\beta_{Rb}}{(2\pi)^{3/2}a^3}N_{Rb}^2, \tag{5-15}$$

which is in the form of a Ricatti equation with constant coefficients. During the loading phase with the initial condition $N_{Rb}(0)=0$, Eq. (5-15) can be solved and becomes

$$N_{Rb}(t) = N_0\left(1 - \frac{(1+\xi)e^{(-t/\tau_L)}}{1+\xi e^{(-t/\tau_L)}}\right). \tag{5-16}$$

Where ξ is defined as the total loss rate fraction of trapped atoms

$$\xi = \frac{1}{1 + \sqrt{8}\,\frac{\alpha_{Rb}}{\beta_{Rb}\,n_0}} \tag{5-17}$$

and τ_L is the load time constant

$$\tau_L = \frac{1-\xi}{1+\xi}\frac{1}{\alpha_{Rb}} \tag{5-18}$$

[179]. Eq. (5-15) can also be solved for a case of trap decay when suddenly at $t=0$ the trap filling is stopped, for instance, for an Ar* trap, when the Zeeman slower is blocked, and the trap is allowed to decay naturally. Therefore, at $N_{Rb}(0)=N_0$ the solution to Eq. (5-15) is

$$N_{Rb}(t) = N_0\frac{(1-\xi)e^{(-t/\tau_D)}}{1-\xi e^{(-t/\tau_D)}}, \tag{5-19}$$

where τ_D is decay rate time constant and is defined as the inverse of the linear loss rate

α_{Rb},

$$\tau_D = \frac{1}{\alpha_{Rb}}. \tag{5-20}$$

ξ is defined in the same way as Eq. (5-17) and in the case for an Ar* decay curve β_{Ar} can be extracted from that expression. Two other useful relations are the steady state number of trapped atoms

$$N_0 = \frac{L_{Rb}}{\alpha_{Rb}}(1-\xi), \tag{5-21}$$

and the loss rate $\beta_{Rb}n_0/2^{3/2}$, which leads to the total loss rate fraction ξ. In general the total loss rate fraction is of the order of $\xi \approx 0.3$ for this experiment and is typically in the range of $0.01 \leq \xi \leq 0.5$ [179].

5.3 SINGLE SPECIES ^{85}RB & ^{40}AR* TRAP LOSS RATE COFFICIENTS

For Rb traps, loss rate coefficients β_{Rb} and linear loss rate coefficients α_{Rb} have already been obtained for various detuning and intensity regimes [180-183]. They are summarized in Table 5.1 with a comparison of the coefficients obtained by this work. The linear loss rate coefficient α_{Rb} is strongly dependent upon background pressure and is therefore smaller for the experiments sited in the references, since their trap background pressure was of the order of $\sim 10^{-10}$ Torr or smaller. In our experimental set up, for only a Rb trap, the background pressure is estimated in the $\sim 10^{-9}$ Torr and the loss rate coefficient of $\alpha_{Rb} = (0.3 \pm 0.1)/s$ reflects the collisions of thermal background Rb atoms with the trapped atoms. The thermal atoms are released from the Rb dispenser source.

TABLE 5.1. Known trap parameters for similar ^{85}Rb traps in comparison with our ^{85}Rb trap. Ar* present denotes that the Ar* decelerated beam is turned on and slowed metastable and Ar atoms are in the trapping region free to interact with the ^{85}Rb trap.

I (mW/cm^2), δ (2π MHz)	N_{Rb} # of atoms	Density (cm^{-3})	β_{Rb} (cm^3/s)	α_{Rb} (s^{-1})	Ref.
35, $\delta = -\Gamma$	$(6.0 \pm 0.5)x10^6$	$(2.5 \pm 0.5)x10^{10}$	$(3.9 \pm 0.8)x10^{-12}$	0.007	[180]
30, $\delta = -2\Gamma$	$5x10^3$	$3x10^9$	$4.0x10^{-12}$	0.02	[181]
20, $\delta = -\Gamma$	N/A	$2x10^{10}$	$9x10^{-12}$	0.02	[182]
10, $\delta = -\Gamma$	N/A	$2x10^{10}$	$3.4x10^{-12}$	0.02	[182]
10, δ=small	N/A	N/A	$(3.6 \pm 1.5)x10^{-12}$	N/A	[183]
30, $\delta = -2\Gamma$ Rb only	$(4.1 \pm 0.5)x10^6$	$(3.1 \pm 0.7)x10^{10}$	$(2.7 \pm 0.5)x10^{-12}$	0.3 ± 0.1	T/W
30, $\delta = -2\Gamma$ W/Ar/BG	$(1.2 \pm 0.3)x10^6$	$(1.1 \pm 0.6)x10^{10}$	$(5.6 \pm 1.8)x10^{-12}$	1.9 ± 0.3	T/W

T/W: Represents this work.

N/A: No information was available in the references.

W/Ar/BG: With Ar background

When the trapping chamber is opened up to the decelerated Ar* beam, the background pressure is estimated to be in ~10^{-8} Torr further increasing the linear loss rate coefficients to $\alpha_{Rb} = (1.9 \pm 0.3)/s$. This is of order 10 times larger than without the Ar*

beam. This increase is due to the fact that thermal Ar* atoms, not captured by the Zeeman slower, and regular thermal Ar atoms, expelled from the source, are contributing toward a higher background pressure. The immediate impact of this increase in background pressure is a drastic reduction in the number of trapped ^{85}Rb atoms. On average four times less atoms are present in the trap after the Ar* beam is turned on.

The two-body loss rate coefficient $\beta_{Rb,}$ in Table 5.1, for the Rb trap only is within accepted values of the other data presented for similar intensity and detuning. With the Ar* beam present the two-body loss rate coefficient is $\beta_{Rb} = (5.6 \pm 1.8) x 10^{-12} cm^3/s$ a factor of two times larger than without an Ar* beam. This number is also within the accepted range for the Rb two-body loss rate coefficient. The slight difference can be attributed to a change in light assisted collisions, since during dual MOT operations the optics have to be optimized for both Rb and Ar lasers simultaneously, Fig. 3.13. Even slight daily adjustments on a polarizer can have small effects on MOT intensity sufficient to attribute for small changes over time. Furthermore the overall MOT system dynamics have changed from a closed system to an open system affecting background pressure and getter dispenser influences on the MOT.

The ^{85}Rb data from Table 5.1 was obtained by curve-fitting Eq. (5-16) to the loading curves of the MOTs. Fig. 5.4 and Fig. 5.5 show a typical example of two loading curves fitted to Eq. (5-16), one without an Ar* background, and the other with an Ar* background.

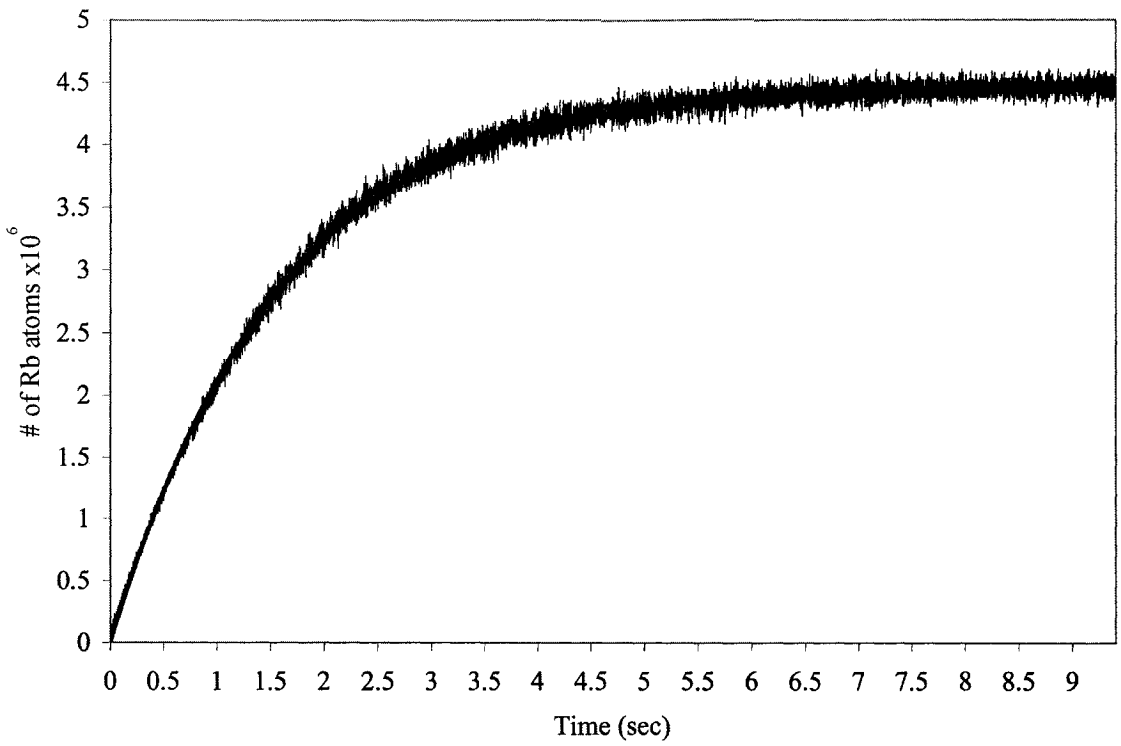

FIG. 5.4. Rb loading curve without any Ar* background. With α_{Rb}=0.6/s and $\beta_{Rb} = 3.6x10^{-12} cm^3/s$. The light gray line is the fluorescence from the PMT, and the dark solid lines are the curve fits of Eq. (5-16), from which rate coefficients were extracted.

All data was taken after the open system was allowed to reach equilibrium after several hours of running. Care had to be taken that the Ar* source was adjusted continuously, during this time, so as not to surge the system and still allow it to reach equilibrium without extinguishing the source. All optics and equipment was fine-tuned for the day's operation before data was taken. After the system had reached the optimal operating conditions the data was taken, in the form of loading curves by blocking and unblocking the MOT beam, and recorded with a PMT. The PMT was a multialkali Hamamatsu R928 with a quantum efficiency of 4% at 780 nm and it was adjusted to a

gain of 10^7. The optical losses were discussed in Chapter 4.3 and depicted in Fig. 4.9, with an solid angle of 1/225 sr. All data was curve fit as shown in Fig. 5.5, and the loss rate coefficients were extracted for different runs over a three month period. During

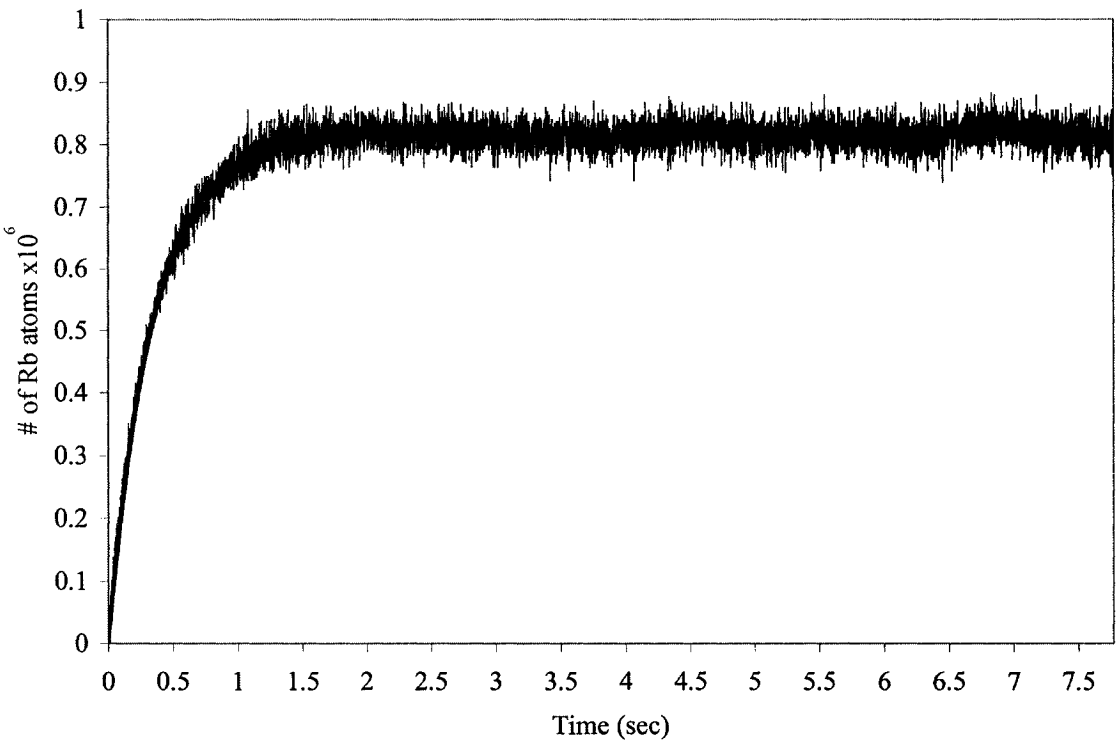

FIG. 5.5. Rb loading in the presence of an Ar* background. With α_{Rb}=2.8/s and $\beta_{Rb} = 5.8x10^{-12} cm^3/s$. The light gray line is the fluorescence from the PMT, and the dark solid lines are the curve fits of Eq. (5-16), from which rate coefficients were extracted.

that timeframe eleven successful loss rate coefficients were recorded. All of them were repeatable and their standard deviation error was calculated to be 13% for α_{Rb} and 30% for β_{Rb}. Systematic error due to laser drift and noise was estimated to be less than 2%. Due to the ^{85}Rb halo of Fig. 4.10 the Gaussian distribution was not a perfect fit, but the

solution to Eq. (5-1) rest on that assumption, this resulted in a model error of 20%.

Comparable information on Ar* collisional loss rate constants is not available, but an Ar* trap was built by Hidetoshi Katori and Fujio Shimizu of Japan in the early 1990's. Some relevant information is available from this experiment [184, 185]. They showed a relation for the linear loss rate coefficients α_{Ar} with dependence on trap background pressure to be $3.3\text{x}10^{7}$ $\text{Torr}^{-1}\text{s}^{-1}$ which suggest an α_{Ar}=3.3/s for a background pressure of $\sim 10^{-7}$ Torr. They summarized that collision with residual gas molecules had a substantial effect on their measurements. Even at $\sim 10^{-10}$ Torr the collisional quenching rate was reported to be of order 10^{-2} s^{-1} from background ionization. They expected that most of the trapped atoms were kicked out of the trap by collisions with large impact parameters. In this case the collisions are elastic and their cross section depends largely on the configuration of the outer electrons.

In trapping Ar* it is possible to obtain a fluorescence signal of the number of trapped atoms and their respective loading and decay curves. It is also possible, because of collisions between two metastable atoms, to produce ions and an ion signal. Since the ionization potential of most residual background gas molecules in the vacuum chamber is higher than the ionization energies of the $1s_5$ metastable state of Ar*, ions are produced only by the PI Eq. (5-8) and AI Eq. (5-9) processes between Ar* atoms. The fluorescence signal of loading and decay curves, fitted to Eq. (5-16) and Eq. (5-19) respectively, give us the total rate constants α_{Ar} and β_{Ar}, while the ion signals fitted to Eq. (5-10) give us the corresponding ionization components α_I and β_I, Eq. (5-7) of the total loss rate. Fig. 5.6 shows a typical decay/loading curve and its ion counterpart for an Ar* MOT. The trap was first loaded until it reached a steady state, the Zeeman slower laser

beam was then blocked thus allowing the trap to decay. After the trap had emptied, the Zeeman slower beam was again unblocked and the trap was allowed to load. This technique makes it possible to obtain load and decay time constants without having to

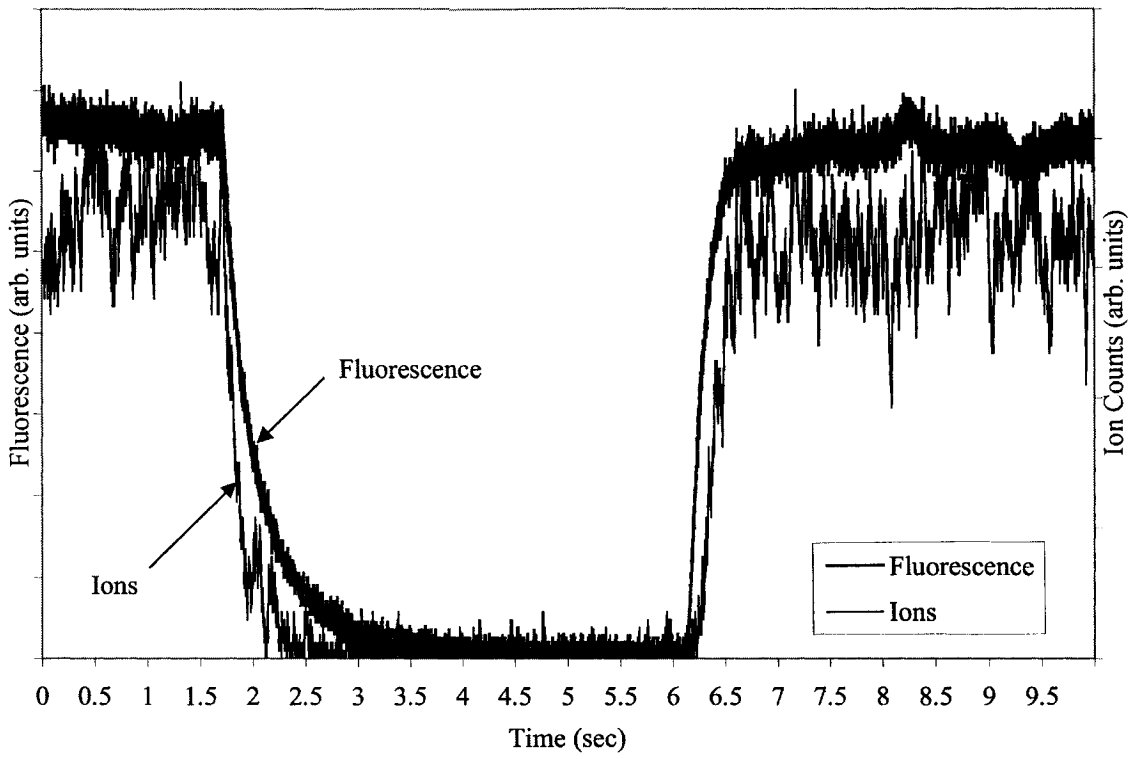

FIG. 5.6. Typical decay and loading curves of an Ar* MOT. These curves were obtained by the blocking and unblocking of the laser beam of the Zeeman slower. The light gray curve represents the total number of atoms in the trap at a given time, with α_{Ar}=3.5/s. While the dark gray line represents the ion loss rate due to metastable collisions.

turn the Ar* MOT beam on and off. This is an advantage over the Rb trap where the MOT beams have to be initially blocked then unblocked to obtain a loading curve. Understandably, this technique does not yield a decay curve for Rb consequently giving

the Ar* trap another advantage.

In analyzing the data the fluorescence signal was curve fitted first, then the ion signal was curve fitted, and the two rate constants were then compared. It was not possible to determine any distinguishable differences between the fit parameters and the total rate constant and the ion rate constant, which suggest that $\beta_{NI} \ll \beta_I$ and that $\beta_{Ar} \cong \beta_I$. This result is not surprising since it had already been observed that ($\beta_{NI} \ll \beta_I$) for Xe and that ionization collisions in metastable atoms are the dominant trap loss rate mechanisms at high trap densities [172]. The collisional rate constants obtained for the Ar* trap are listed in Table 5.2 with some known values obtained from other noble gas experiments. No direct Ar* numbers are available for comparison from experiments or ultracold collisional theory.

Since it was our objective to create a dual species trap we looked for the largest possible Ar* MOT we could create. Large traps would make a dual trap Rb-Ar* overlap easier and the interaction probability of Rb-Ar*, for determining its interaction parameter, is much increased. It was determined that the maximum trap fluorescence was obtained when the detuning was set to three-halves to the red of the natural linewidth of ^{40}Ar* ($\delta = -3/2\Gamma$). This detuning also corresponded to the maximum ions produced by the trap, since at higher trap density the ion production rate should also be increased. At that detuning, and at a MOT intensity of 200 mW/cm^2, we obtained a $\beta_{Ar} = (2.7 \pm 1.4) x 10^{-10} cm^3/s$. No direct comparison could be made since this loss rate coefficient is an original result for Ar*. Since most other noble gas collisional rate constants are larger by at least one order of magnitude to those of the alkali-metal type

TABLE 5.2. Important Ar* trap parameters for the MOT, in comparison with other noble gas collisional rate constant and known factors.

Atom, I (mW/cm^2), δ (2π MHz)	N # of atoms	Density (cm^{-3})	β (cm^3/s)	α (s^{-1}) * Torr^{-1}s^{-1} ** Torr	Ref.
He N/A	$5x10^6$	$1x10^9$	$1.3x10^{-10}$	N/A	[81]
N/A	N/A	N/A	$2.7x10^{-10}$	N/A	[186]
Ne 33, VAR	$7.6x10^8$	$4x10^{10}$	$6.8x10^{-10}$	0.26	[131]
N/A, VAR	$4x10^7$	N/A	N/A	10^{-7} **	[187]
^{40}Ar 200, $\delta = -3/2\Gamma$	$(1.4\pm0.4)x10^6$	$(1.2\pm0.4)x10^{10}$	$(2.7\pm1.4)x10^{-10}$	3.2 ± 0.8	T/W
200, N/A	$6x10^5$	$9x10^9$	N/A	N/A	[184]
N/A	N/A	N/A	N/A	$3.3x10^7$ *	[185]
Kr 200, N/A	$1x10^5$	N/A	N/A	$2.1x10^7$ *	[185]
N/A	N/A	N/A	$2x10^{-10}$	10^{-10} **	[174]
Xe 24, $\delta = -3/2\Gamma$	N/A	$5x10^{10}$	$6x10^{-11}$	~0 small	[172]
230, $\delta = -1/2\Gamma$	$2x10^5$	$2x10^3$	N/A	N/A	[188]

T/W: Represents this work.

N/A: No information was available in the references.

VAR: Varied during the experiment.

* and **: Some experiments do not give a precise α but report a background pressure or rate.

mostly due to PI and AI and it is in agreement with those expectations. During an average MOT operation as many as half the atomic population can be in the excited state making it possible to have both ground state S - S collisions as well as excited state S - P collisions. Both of these collisions contribute toward the total loss rate coefficient β_{Ar} and are responsible for the fact that the noble gas coefficients are larger than those of the alkali-metal ones. Making this the PI and AI losses for Ar* a more dominant loss mechanisms than the FS and RE losses of that of alkali-metal type atoms, like Rb. This can further be understood by considering that during collisions in the PI process one atom decays to the ground state and the other is ionized. While for AI process an ionized molecule is formed which means that during each collision two atoms are lost which cannot be recovered by the MOT. This is contrary to the alkali-metal type atoms, which sometimes can be recaptured by the MOT, resulting in an overall smaller loss rate coefficient for those atoms.

Future studies can focus on studying what contribution the metastable ground state and excited state have toward the total rate coefficient. This could be done by confining a sample of Ar atoms in a MOT and observing the metastable ground state ionization rates while then using an excitation laser to populate the excited states and observe the change in the ionization rate.

The linear loss rate coefficient for the Ar MOT was determined to be $\alpha_{Ar} = (3.2 \pm 0.8)/s$ this can be compared to H. Katori et al. [185] MOT pressure dependent collision rate constant of 3.3×10^{7} $Torr^{-1}s^{-1}$. At a MOT background pressure range from 10^{-7} Torr to 10^{-8} Torr this would suggest a range of α_{Ar} of 3.3/s to 0.33/s, which is in the range of what we have found for our MOT. The type of discharge used

and if the beam is optimized for metastable Ar* should also play a roll in the α_{Ar} rate coefficient. Future improvements such as beam bending techniques as discussed in Chapter 3.2 and shown in Fig. 3.9 will lead to a reduction of that coefficient.

Due to experimental limitations the same maximum laser intensity of the Ti:Sapphire laser could not be ensured on a daily basis. It is therefore important to know how the rate coefficient behaves over varying laser intensity. Since ^{40}Ar* does not have a hyperfine structure it is not expected that in a low intensity regime a new loss mechanism will dominate as in ^{85}Rb. But due to low laser intensity fewer atoms should be in the excited state suggesting a lower loss rate coefficient for lower intensities than with higher ones. Fig. 5.7 shows the rate coefficient dependence on the MOT intensity variation for a constant detuning and a constant Zeeman beam intensity. As the MOT laser intensity increases an initial increase in β_{Ar} can also be observed, due to the limitation of a further increase of laser intensity no further increase can be identified but is expected. Band and Julienne predicted such a trend and it is generally expected that there is a dependence of MOT laser intensity on the trap loss rate coefficients [178, 189]. The limitation maximum laser intensity and data points taken at that maximum intensity leave a final conclusion at this point still open. A future study of Ar* trap loss with a large intensity variation would resolve any such uncertainties. The maximum number of data points were recorded for data points at our maximum laser operating intensity since this is the operating point for the dual MOT experiments.

The Ar* MOT experiments were conducted under the same conditions as for the Rb MOT with Ar influence. The system was allowed to reach equilibrium and the florescence was recorded with a similar multialkali Hamamatsu R928 PMT with a

quantum efficiency of 2% at 811 nm and it was adjusted also to a gain of 10^7. The optical losses were also as discussed in Chapter 4.3 and depicted in Fig. 4.9, with a solid angle of 1/225 sr. All data was curve fit as shown for Rb MOT loading with the exception that the decay time constant could now be obtained due to blocking of the Zeeman beam, and the loss rate coefficients were extracted for different runs over a three month period. During that timeframe nineteen successful loss rate coefficients were

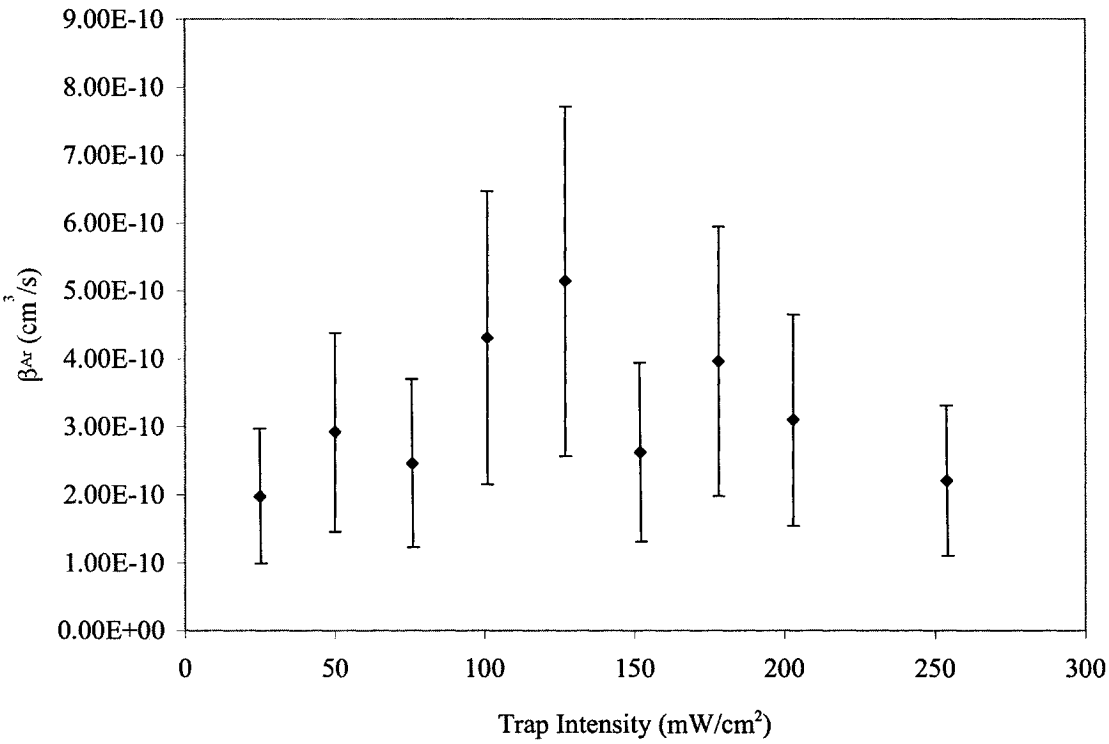

FIG. 5.7. Variation of trap loss rate constant with an increase of MOT intensity. With $\delta = -3/2\Gamma$, and a Zeeman slower intensity of 130 mW/cm^2.

recorded at maximum operating intensity. All of them were repeatable and their standard deviation is 25% for α_{Ar} and 50% for β_{Ar}. Systematic error due to laser drift and noise

was estimated to be less than 2%.

Since the maximum Ti:sapphire laser power could vary from day to day operation it is of interest to know how the daily Ar* MOT operation could vary with different MOT and Zeeman laser intensities. Fig. 5.8 shows how the number of trapped atoms increases with increasing MOT laser intensity with the Zeeman slower laser held at a constant

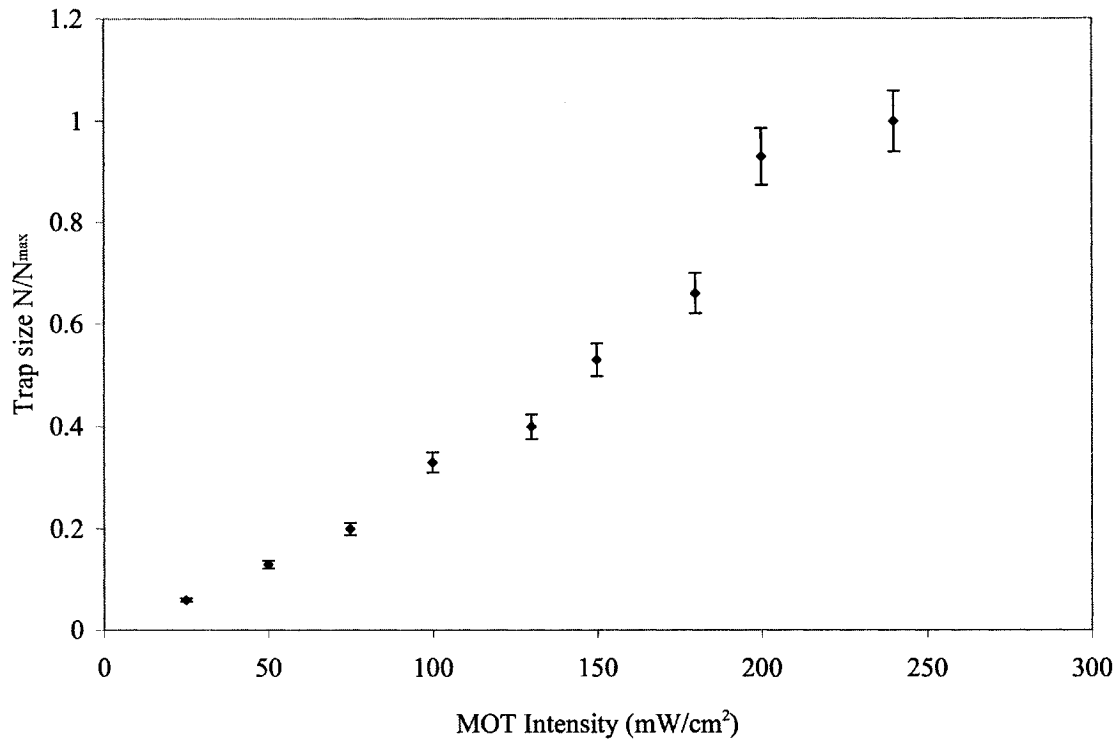

FIG. 5.8. The change of trapped atoms for an alteration in MOT laser intensity with a constant Zeeman slower intensity of 150 mW/cm^2. The number of atoms is normalized to the maximum number of atoms in the trap at maximum MOT intensity.

maximum intensity. As can be seen this is a nearly linear process, with a decrease of trap size to half maximum when the laser intensity is approximately half maximum and going

toward zero as the intensity goes to zero. In Fig. 5.9 the MOT laser intensity is held constant and the Zeeman slower laser intensity is varied. With decreasing laser intensity, the Zeeman slower captures fewer atoms and the MOT load rate is diminished. From Fig 5.9 it can be seen that above 100 mW/cm^2 the Zeeman slower reaches a saturation regime, where an increase in laser intensity produces less atoms per mW/cm^2 of laser

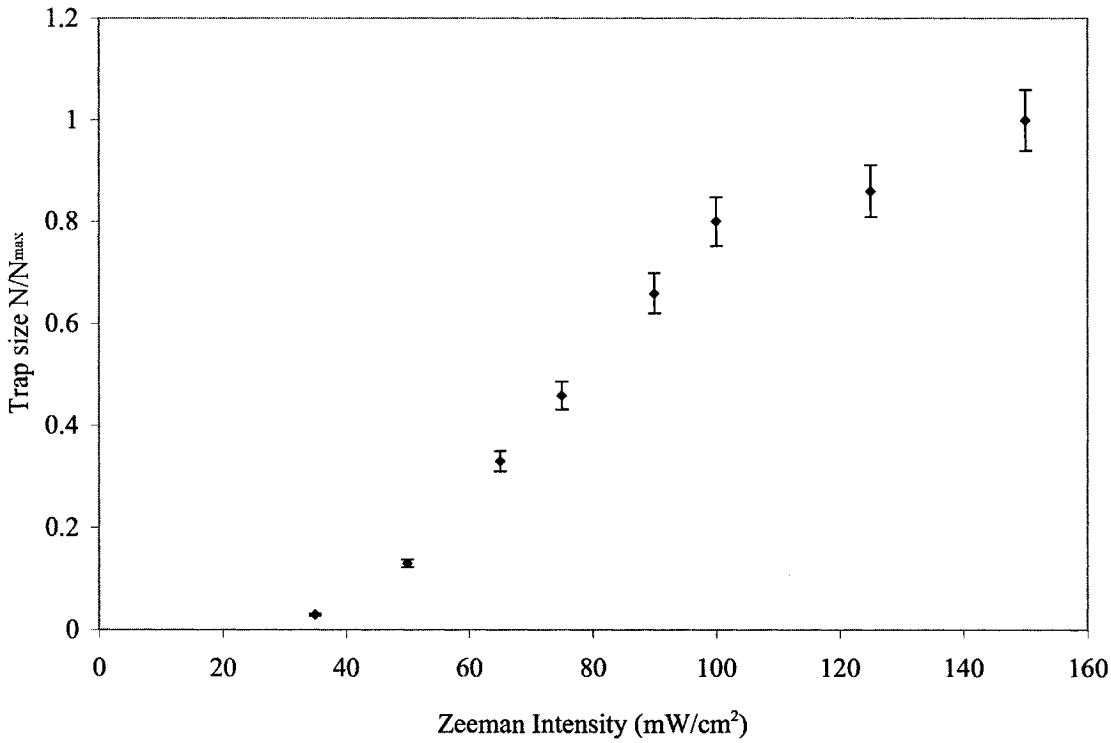

FIG. 5.9. The change of trapped atoms for a constant MOT intensity of 240 mW/cm^2 with varying Zeeman slower laser intensity. The number of atoms is normalized to the maximum number of atoms in the trap at maximum MOT intensity.

power. As for an intensity of 30 mW/cm^2, this is the lower threshold of intensity, below this intensity no Ar* will be trapped and the Zeeman slower is not operational. The

regime 30 mW/cm^2< I_{Zeeman}<100 mW/cm^2 shows a constant linear increase in the atoms captured in the MOT, with optimal maximum of slowed Ar* flux at a laser intensity of >100 mW/cm^2.

All dual species trap experiments were conducted at maximum Rb and Ar* MOT laser intensities to increase the number of atoms in the MOT and to be able to detect and quantify a dual species interaction.

5.4 THE DUAL ^{85}RB-^{40}AR* TRAP LOAD RATE EQUATION

The loss rate mechanisms for the single species MOTs of Rb and Ar* still apply in a dual species MOT. In addition a new intra species loss rate mechanism also has to be defined. Eq. (5-1) still applies but has to be modified to contain a term for the MOT loss mechanism of the intra species interactions, it then can be rewritten as

$$\frac{dN_{Rb}}{dt} = L_{Rb} - \alpha_{Rb} N_{Rb} - \beta_{Rb} \int_V n_{Rb}^2 d^3r - \gamma_{Rb-Ar} \int_V n_{Rb} n_{Ar} d^3r. \qquad (5\text{-}22)$$

This equation describes the trap loading of Rb in the presence of Ar*, where $\gamma_{Rb\text{-}Ar}$ represents the Rb loss rate due to collisions with trapped Ar* atoms. Ar* has a noticeable exact counterpart to Eq. (5-22) with $\gamma_{Ar\text{-}Rb}$, where this is the loss rate constant representing the collisional loss of Ar* in the presence of trapped Rb. It cannot be assumed that there is a reciprocity in the $\gamma_{Rb\text{-}Ar}$ and $\gamma_{Ar\text{-}Rb}$ terms since trap depth, size of traps, number of trapped atoms, atomic energy levels and other trap parameters are not the same for each individual species trap [124]. All other parameters in Eq. (5-22) are the same as defined in the previous sections.

The primary loss channels for the Rb-Ar* dual species interaction are expected to

be similar to those of noble gases. The first one is again Penning ionization. This time a ground state Rb atom collides with an Ar* atom to produce a ground state Ar atom and a Rb^+ ion, Eq. (5-23). The second less dominant loss mechanism is associative ionization in which a Rb^+Ar molecular ion is formed again containing some of the internal energy in the form of vibrational energy, Eq. (5-24). These processes are

$$Rb(5^2S_{1/2}) + Ar^*(4^2P_2) \rightarrow Ar(^1S_0) + Rb^+ + e^-, \quad (5\text{-}23)$$

$$Rb(5^2S_{1/2}) + Ar^*(4^2P_2) \rightarrow Rb^+Ar + e^-. \quad (5\text{-}24)$$

Therefore, a ^{85}Rb atom in a dual ^{85}Rb - ^{40}Ar system has six possible ways to collide inelastically with another atom in the dual MOT and be ejected from it. ^{40}Ar has four possible channels to leave the trap during a collision. It also gives rise to two species dependent and two intra species collisional dependent rate constants, and two background gas dependent constants.

Table 5.3 shows a brief summary of other dual species trap collisional interaction parameters. Most of the collisional loss rate parameters are higher in the low intensity regime due to heteronuclear hyperfine changing collisions [119, 121-124, 127]. As with an increase in intensity fine structure and radiative escape begin to dominate and the loss rate constant increases again. This behavior is the result of the heteronuclear alkali-metal interaction, and this interaction is expected to be different than that of a noble gas interaction, where the noble gas does not have a hyperfine structure.

TABLE 5.3. A summary of loss rate coefficients of other heteronuclear collisions.

Species	γ	Species	γ
^{85}Rb-^{87}Rb [113]	~1-2x10^{-11} cm^3/s	Na-Rb^{85} [122]	~10^{-11} cm^3/s
Na-Li [115]	~10^{-11} cm^3/s	Na-Rb^{87} [122]	~10^{-11} cm^3/s
Cs-Li & Li-Cs [118]	~10^{-10} cm^3/s	Na-Rb [123]	~10^{-10} cm^3/s
^{39}K-^{85}Rb [119]	~10^{-11} cm^3/s	Na-Cs [124]	~10^{-11} cm^3/s
Na-K [121]	(3.0±1.5)x10^{-12} cm^3/s	Rb-Cs [127]	~10^{-11} cm^3/s

5.5 DETERMINATION OF THE LOSS RATE COEFFICIENTS

To obtain an expression for the dual species loss rate coefficient for a Gaussian spatial density distribution the following equation is used

$$n_{Rb}(\vec{r},t) = n_{0Rb}(t)e^{-2(r/w_{Rb})^2}. \qquad (5\text{-}25)$$

Where n_{0Rb} is again the respective peak density and w_{Rb} is the Gaussian waist of the trap, observed by a CCD camera of the cloud of trapped atoms. Eq (5-25) also applies for Ar* where the subscripts are then changed to Ar. The definition of the Gaussian density distribution and Gaussian waist w_{Rb} of the dual species MOT is chosen here to be consistent with other work done in dual species MOTs [119]. Substituting Eq. (5-25) and its Ar* counterpart into Eq. (5-22), yields

$$\frac{dN_{Rb}}{dt} = L_{Rb} - \alpha_{Rb} N_{Rb} - \frac{\beta_{Rb}}{(\pi)^{3/2} w_{Rb}^3} N_{Rb}^2 - \gamma_{Rb-Ar} \left\{ \frac{2}{\pi \left(w_{Rb}^2 + w_{Ar}^2 \right)} \right\}^{3/2} N_{Ar} N_{Rb} \quad . \tag{5-26}$$

To determine $\gamma_{Rb\text{-}Ar}$, a steady state approach is used. In this technique an already loaded Rb trap, in a steady state, is subjected to the loading of a Ar* trap spatially overlapped with the Rb trap. Eq. (5-26) is then written for a steady state condition before the presence of Ar* where $\gamma_{Rb\text{-}Ar}$=0. A second Eq. (5-26) is then written for a steady state with Ar* present. Both equations are then subtracted from each other and solved for $\gamma_{Rb\text{-}Ar}$ to give

$$\gamma_{Rb-Ar} = \left[\frac{\pi (w_{Rb}^2 + w_{Ar}^2)}{2} \right]^{3/2} \frac{1}{N_{Ar} N'_{Rb}} \left\{ \alpha_{Rb} (N_{Rb} - N'_{Rb}) + \beta_{Rb} \left[\left(\frac{1}{\pi w_{Rb}'^2} \right)^{3/2} N'_{Rb} - \left(\frac{1}{\pi w_{Rb}^2} \right)^{3/2} N_{Rb} \right] \right\} . \tag{5-27}$$

Where N'_{Rb} and w'_{Rb} are the number of atoms and Gaussian cloud waist in the presence of the Ar* MOT, while N_{Rb}, w_{Rb} and N_{Ar}, w_{Ar} are the number of atoms and Gaussian waist respectively, of the independent MOTs without the other species present [127]. A similar expression can be derived for the $\gamma_{Ar\text{-}Rb}$ MOT coefficient. Of significance will be the definition of $\Delta N = N_{Rb} - N'_{Rb}$ which is the difference with and without atoms lost due to the loading of the other species. Again, a counterpart for Ar* also applies.

Fig 5.10 shows a typical loading curve of an Ar* MOT being loaded spatially overlapped with a previously loaded Rb trap, the Ar* MOT is then suddenly unloaded to reveal again the Rb MOT. After the sudden unload, the Rb trap needs to reload to its maximum pre Ar* trap interaction level. In Fig. 5.10 this area is marked with a circle,

but due to our small Rb-Ar* interaction a small change in Rb cannot be accurately detected with this method. This is contrary to other experiments where a dip was easily detected in their reloading curves; this was observed with the Cs-Li and K-Rb and Rb-Cs dual species MOTs [118, 119, 127]. For some of those experiments it was possible to read ΔN directly from the figures. In those experiments a reduction of up to 30~40% in trapped atoms was observed when a second species was loaded [123, 127]. Their reduction was significantly larger when compared with our 3%. To determine an accurate change in the

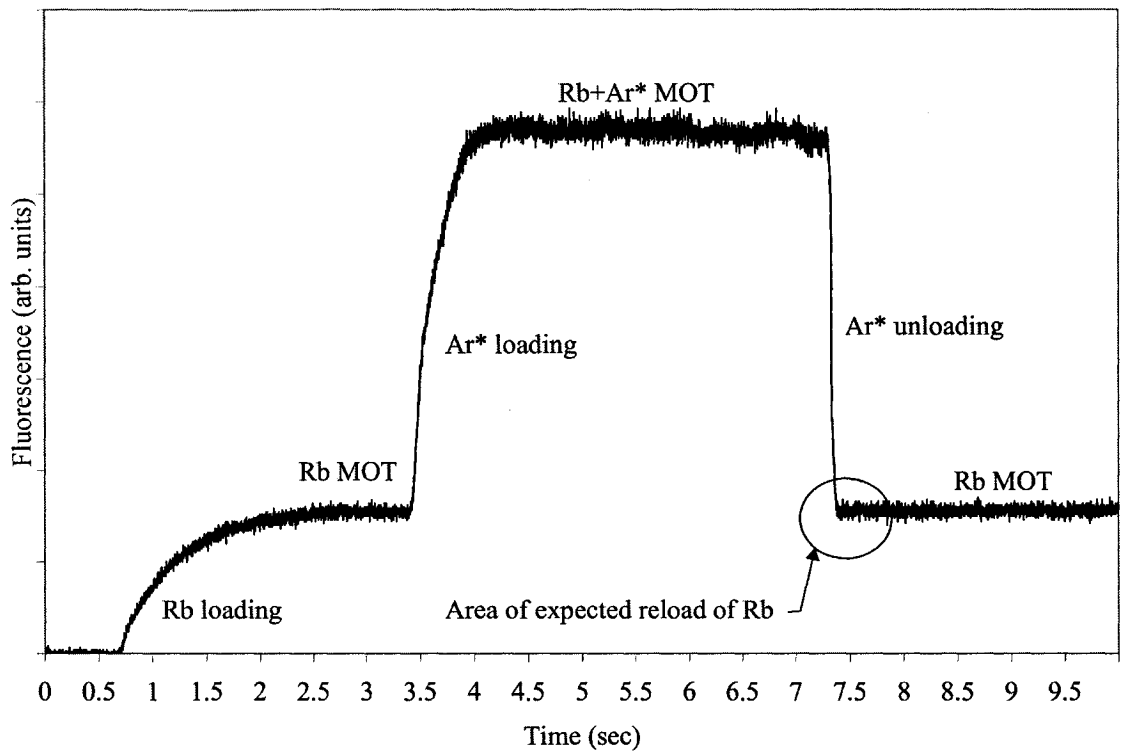

FIG. 5.10. A typical loading of an Ar* MOT on top of a Rb MOT. The Ar* MOT is unloaded suddenly by blocking the Ar* MOT laser beam. The circled area shows the expected reload area, which is too small to be observed for Rb-Ar* interaction.

number of atoms of Rb in the presence of loading/unloading of Ar*, a 780 nm interference filter was used in front of the PMT. The Rb trap was then loaded to a steady state. Subsequently the Ar* trap was loaded spatially overlapped with it and then unloaded. This created the desired dip in the Rb atoms which now could be measured to obtain ΔN, shown in Fig. 5.11. Each data set contained approximately twelve thousand data points representing the number of atoms in the Rb MOT. From those twelve thousand, half were averaged for the Rb+Ar* dual MOT, while the other half were averaged for a sole Rb MOT. Subtracting both the numbers of atoms for the dual MOT population and for the single Rb MOT, ΔN could now be obtained. The Gaussian waists (w_{Rb} and w_{Ar}) were measured with a CCD camera for each trap and the waist of Rb (w'_{Rb}) in the presence of the Ar* loaded trap and vise versa for Ar* (w'_{Ar}). This was done using interference filters for each appropriate wavelength of trapped species mounted in front of the CCD camera. Eq. (5-27) can then be used for this steady state analysis to produce a number for the intra species rate collisional parameter ($\gamma_{Rb\text{-}Ar}$ and $\gamma_{Ar\text{-}Rb}$).

The detailed results for each of the dual species collisional loss rate parameters Rb-Ar* $\gamma_{Rb\text{-}Ar}$ obtained are shown in Table 5.4. The dual species trap loss rate Rb-Ar* coefficient was found to be of order $\gamma_{Rb\text{-}Ar} \sim 10^{-11}$ cm^3/s which is an order of magnitude larger than that of the Rb collisional rate coefficient $\beta_{Rb} \sim 10^{-12}$ cm^3/s. This shows that the trap loss rate is higher due to the presence of Ar* atoms but smaller than the Ar* loss rate coefficient $\beta_{Ar} \sim 10^{-10}$ cm^3/s. This suggests that an interaction of Ar* with Rb has a small but notable effect on the Rb MOT population. Furthermore, since we are only at the low end of the Rb intensity regime this collisional parameter sets only a lower limit on the interaction of Rb with Ar* [127]. It is expected with future study to expand upon the

intensity regime of the dual species Rb-Ar* interaction.

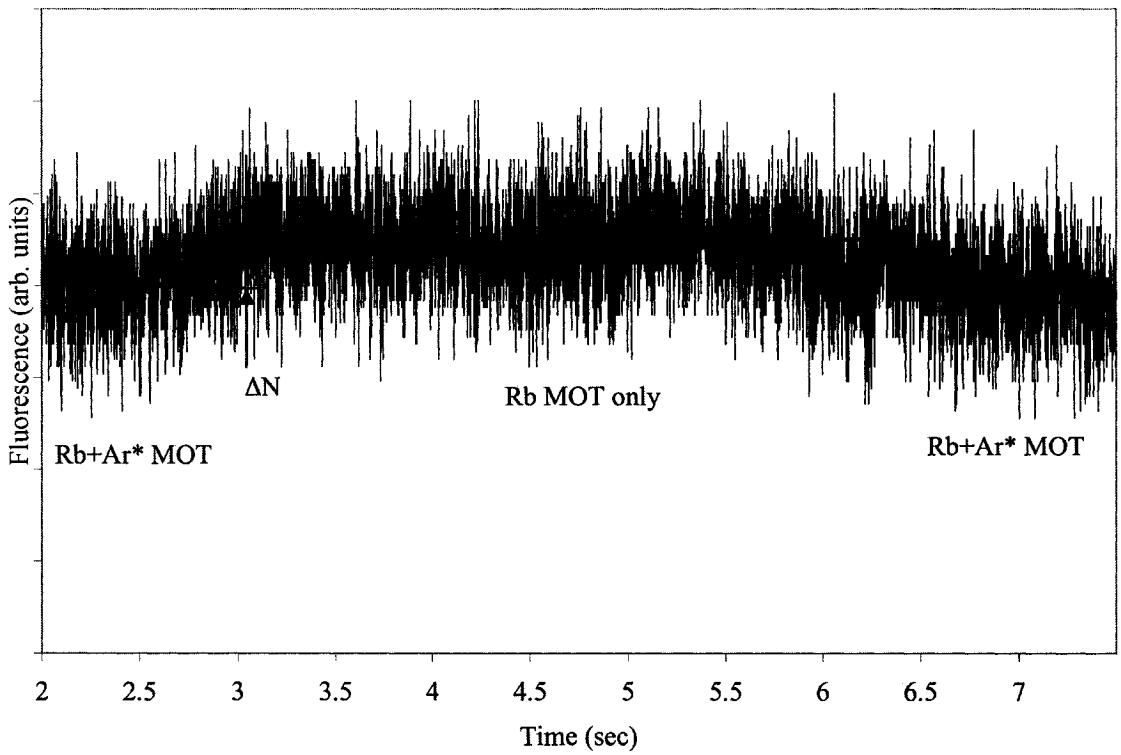

FIG. 5.11. Typical loading and unloading of the Ar* MOT on top of the Rb MOT. Rb fluorescence only in the presence of Ar*, then Ar* is unloaded which gives a larger Rb trap and after that Ar* is reloaded for a reduction in Rb again. The change in the number of atoms ΔN can then be measured by averaging the data points.

TABLE 5.4. Detailed data used in determining the dual species collisional rate constant of the Rb-Ar* interaction.

Data set	ΔN (# of atoms)	Rb reduction (%)	$\gamma_{Rb\text{-}Ar}$ (cm^3/s)
1	$25x10^3$	2.0	$3.1x10^{-11}$
2	$41x10^3$	2.2	$5.1x10^{-11}$
3	$57x10^3$	3.0	$7.1x10^{-11}$
4	$26x10^3$	2.0	$3.4x10^{-11}$
5	$26x10^3$	2.0	$3.4x10^{-11}$
6	$32x10^3$	3.0	$6.3x10^{-11}$
7	$45x10^3$	4.0	$8.8x10^{-11}$
8	$32x10^3$	3.0	$3.4x10^{-11}$
9	$67x10^3$	4.0	$5.0x10^{-11}$
10	$67x10^3$	4.0	$4.4x10^{-11}$
11	$46x10^3$	3.0	$3.1x10^{-11}$
12	$67x10^3$	3.5	$4.5x10^{-11}$
13	$67x10^3$	3.5	$4.5x10^{-11}$
Mean value		3%	$4.8x10^{-11}$ cm^3/s
Standard deviation			$1.6x10^{-11}$ cm^3/s
Statistical error			33%

Investigations to determine the Ar*-Rb interaction loss rate coefficient $\gamma_{Ar\text{-}Rb}$, with the same experimental techniques used to determine $\gamma_{Rb\text{-}Ar}$, have shown no definite evidence in a reduction of trapped Ar* atoms. It is not uncommon that during dual species interactions one collisional process can be twenty times smaller than its counterpart and consequently harder to determine [127]. The major loss mechanisms for the Ar* and Rb interactions are expected to be either PI or AI. During either a PI or AI collision one Rb and one Ar* atom are lost from the MOT. Therefore, if the Rb loss is due to ionization then for each Rb atom lost one Ar* atom is also lost from the MOT. With a 3% Rb trap reduction the ion production yield for a PI and AI interaction is extremely small and is currently below our detection capability. Furthermore, the ion signal tends to disappear in the background noise. The instrumental resolution capabilities of our CEM can add no definite additional information at these low intensity regimes. This might be resolved when laser intensities and MOT sizes are increased and such ion yields would be large enough to emerge from the background noise. It is also possible that the Rb-Ar* interaction loss is due to radiative escape, that is as the two atoms approach each other, on their short range potential, a photon is emitted before they can get close enough for PI or AI to take place. This type of loss would not produce an ion yield. As of now no definite conclusion can be reached.

The experimental setup used was the same as described in section 5.3 for the individual set ups of Rb and Ar*. The systematic error due to laser drift and noise was estimated to be less than 2%. A summary of the experimental parameters is given in Table 5.5.

TABLE 5.5. Summary of the dual species trap experiment and the collisional rate coefficient for the Rb-Ar* interaction.

Trap intensities Ar* Trap intensities Rb	(200-250) mW/cm^2 30 mW/cm^2
Average Gaussian waist w_{Rb} Average Gaussian waist w'_{Rb} Average Gaussian waist w_{Ar}	~0.6 mm ~0.6 mm ~0.6 mm
Typical reduction of Rb with Ar* present	3%
Collisional rate coefficient for Rb-Ar*	$\gamma_{Rb-Ar} = (4.8 \pm 1.6) x 10^{-11} cm^3/s$
Statistical error	33%
Systematic error	<2%

CHAPTER VI

FIRST OBSERVATIONS OF ^{40}AR* & ^{85}RB DUAL MOT ION PRODUCTION

In Chapter 5 it was shown that the main loss mechanisms for ultracold collisions of metastable noble gases was through Penning ionization (PI) Eq. (5-8) and associative ionization (AI) Eq. (5-9). The same process is also presumed to be dominant for the dual species Rb-Ar* interaction as shown in Eq. (5-23) and Eq. (5-24). The PI process results in the loss of a ground state atom and an ionized atom from the MOT, while the AI results in the loss of a molecular ion. These ions can be detected with a channel electron multiplier (CEM), which is mounted in the chamber. Since the CEM cannot differentiate between different ion species, no general insight as to the ratio of PI/AI produced by the MOT is gained. To measure this ratio several groups have used a time of flight (TOF) technique approach. One of the TOF approaches is to use a catalysis laser and CEM in conjunction with a MOT laser-timing scheme. In the instant the MOT laser beam is turned off a catalysis laser beam is turned on. The catalysis laser then moves the atoms into an excited state attractive potential, which accelerates them closer toward an inelastic collision path. A CEM is gated on while the catalysis laser is on as well. The ion count detected by the CEM then reflects the PI and AI ions produced by the MOT. The first peak is for the faster atomic ions, while the second peak, which arrives later at the CEM by a factor of $\sqrt{2}$, represents the heavier molecular ions [174]. Another approach of the

TOF technique is to use electrostatic plates in conjunction with a TOF tube. The electrostatic plates accelerate and focus the ions produced in the MOT through a TOF tube into a CEM. The electric fields are varied accordingly to allow passage and optimization of the individually selected ions by their mass. This technique also requires an on/off MOT laser-timing scheme, also of note is that the TOF tube and electrostatic plates are mounted directly into the vacuum chamber [190, 191]. A third technique to obtaining an ion mass spectrum is to use a negatively biased quadrupole mass spectrometer mounted directly into the MOT chamber. The quadrupole is mounted directly in front of and is in line with the MOT and a CEM at the end of the quadruple to detect the ions. The quadrupole can filter ions at a mass resolution of 1 amu, which is more than sufficient to detect the difference between PI and AI [192-194].

In this experimental work a Stanford Research Systems Residual Gas Analyzer (SRS RGA200) is used in conjunction with an ion optical field plate assembly, which is setup to extract the ions from the MOT, focus them and project them into the RGA. The RGA is able to determine the mass of ions within 1 amu and is thus able to yield a relative relation of PI versus AI.

6.1 THE SRS RGA200 AND ITS ION OPTICAL SETUP

The SRS RGA200 is a residual gas analyzer, which is generally used to measure buffer gas compositions and other background gases in a vacuum chamber environment. It consists of an electronic control unit mounted outside the vacuum chamber and an ionizer, a quadrupole mass filter, and an ion detector mounted inside the vacuum chamber, Fig. 6.1.

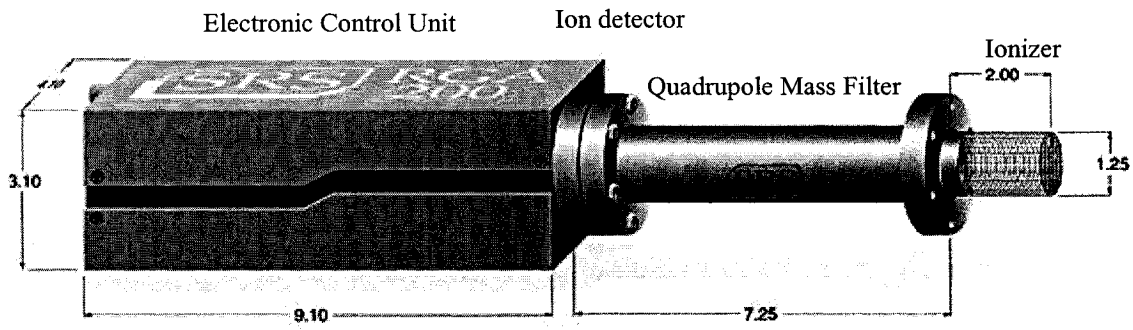

(a)

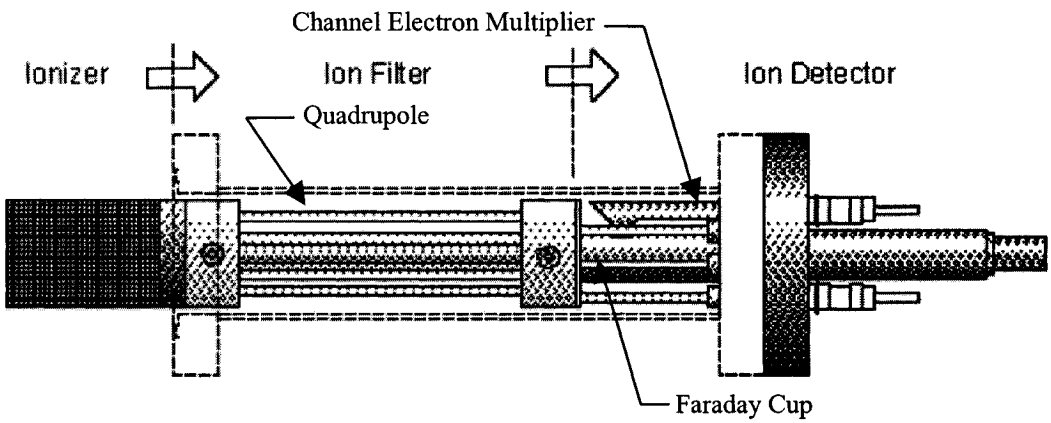

(b)

FIG. 6.1. The SRS RGA200 and its individual components (a). A cross-section of the RGA200 probe as it is mounted in the vacuum chamber (b). Pictures are taken from Ref. [195].

The ionizer is composed of a repeller, a filament, an anode grid, and a focus plate, as depicted in Fig. 6.2. The repeller grid's main functions are to protect the filament and to contain the cloud of electrons within the ionizer by being negatively biased. The filament is the source of an electron cloud that ionizes any atom or molecule caught in the anode grid region. The anode grid's purpose is to propel the ions into the quadrupole mass filter at the proper energy. Before the ions pass through the quadrupole mass filter the focus plate focuses the ions so that they will traverse the quadrupole mass filter and impinge onto the Faraday cup detector at the end of the quadrupole mass filter. The Faraday cup detects the ions that pass successfully through the quadrupole mass filter. This is done by measuring its current directly or an alternate method is by using a CEM that measures the electron current proportional to the ion current, Fig. 6.2 (b).

In the experimental setup that was used, certain modifications had to be made to the RGA200 probe and its electronic control unit to make it suitable for detecting ultracold ions released from a MOT. First, an ion optical setup consisting of several field plates had to be built to focus the ions that were expelled from the MOT, due to ultracold collisions, into the RGA for detection. For that purpose the RGA did not need a negatively charged repeller grid, a filament that emits electrons, and a positively charged anode grid that would deflect any incoming ions. The RGA still needed the focus plate to focus any ions through the quadrupole mass filter and as an additional requirement the ion energy had to be between 2-12 eV at the entrance of the focus plate for them to pass through the quadrupole mass filter and then be detected.

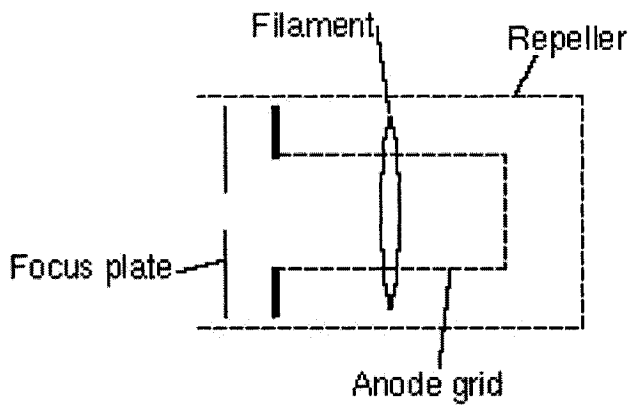

(a)

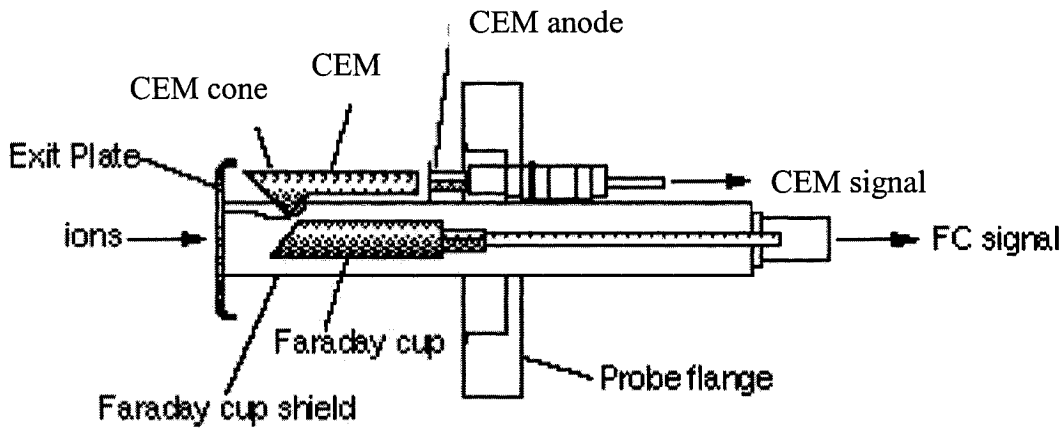

(b)

FIG. 6.2. Detailed schematic of RGA200 head and detector components. The filament, repeller, and the focus plate are at a negative voltage while the anode grid is positively charged (a). A close up view of the detector section with the Faraday cup and the CEM clearly shown (b). Pictures are taken from Ref. [195].

The repeller grid could easily be removed from the RGA200 probe without additional modification necessary to the electronics, however, to turn the filament off and to keep the focus plate still active, modifications to the electronic control units circuit boards had to be made. The focus plate filament and the repeller grid were internally connected to each other. The repeller grid could be unhooked without any further effect, but the filament could not be disconnected without affecting the focus plate. By default a broken or disconnected filament would cause the focus plate not to work. To remedy this situation a modification had to be made to the circuit board and a bypass switch was installed, so that the RGA could still be used in its regular capacity. The switch would then disconnect the filament and still have the focus plate active. As for the anode grid a similar modification had to be made, by lifting two resistors of the circuit board and attaching a switch as well for normal RGA operation [196]. After the modifications the RGA could then be operated without filament, repeller, and anode grid. The focus plate had also the added feature of having its voltage controllable through the computer software; this is useful for fine-tuning the influx of ions into the RGA. The voltage range of an RGA200 focus plate is $0\ V \leq V_{FocusPlate} \leq -150\ V$. Fig. 6.3 shows the RGA200 head with the repeller grid removed as was used for the experiment to measure PI and AI rates.

To extract the ions from the MOT and focus them with the right energy into the RGA a set of three field plates was used. To determine the optimal arrangement of field plates and their potential a computer simulation had to be run, this was done with SIMION, a commercial computer software program that specializes in 3D ion optics simulations. To run a simulation as detailed as possible to the real experimental

environment, the whole 3D MOT chamber had to be modeled in conjunction with the field plate ion optical setup and the RGA focus plate, which was used as the final focus plate. SIMION allowed us to run simulations under different initial conditions for the ions and it was able to determine flight paths and ion energy during the flight toward the RGA [197]. Fig. 6.4 shows a typical simulation run with SIMION, the simulations helped guide the experimental work toward the optimal voltage settings on the field plates. To avoid laser beam clipping the spacing of the field plate was limited inside the MOT.

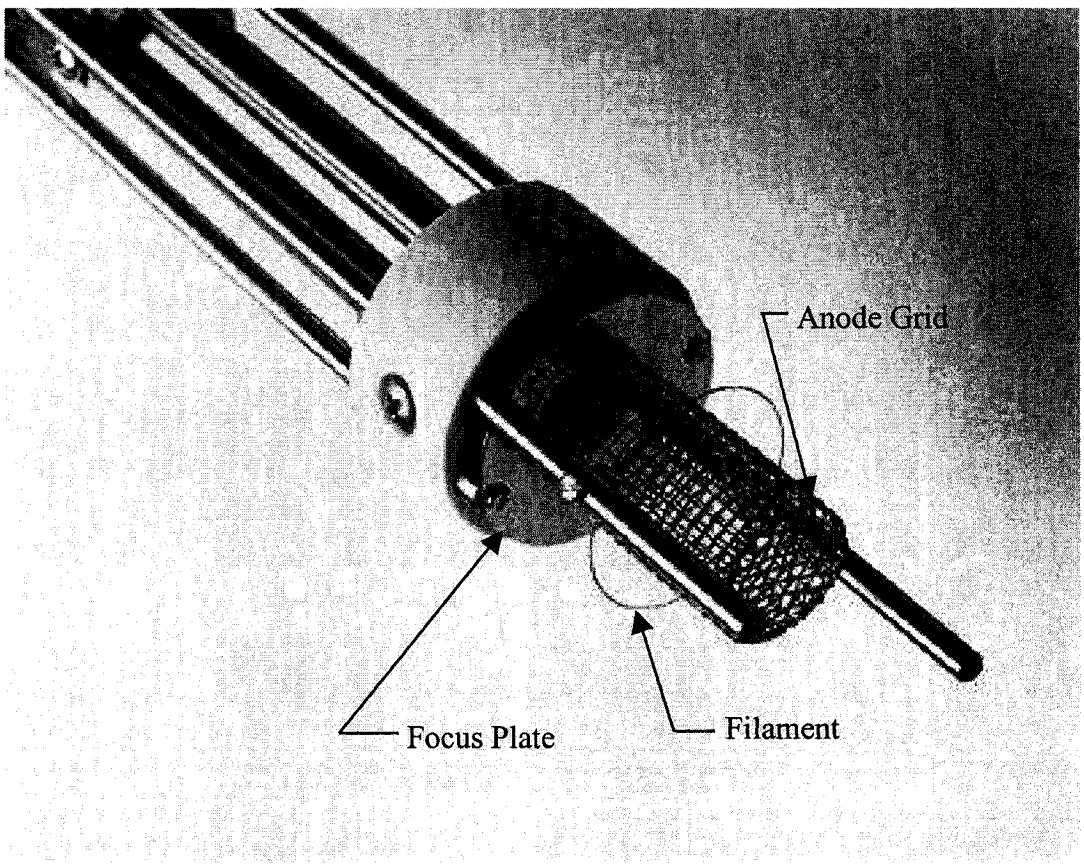

FIG. 6.3. The RGA200 with repeller grid removed. The filament and anode grid were turned off, while the focus plate was still active. Picture is taken from Ref. [195].

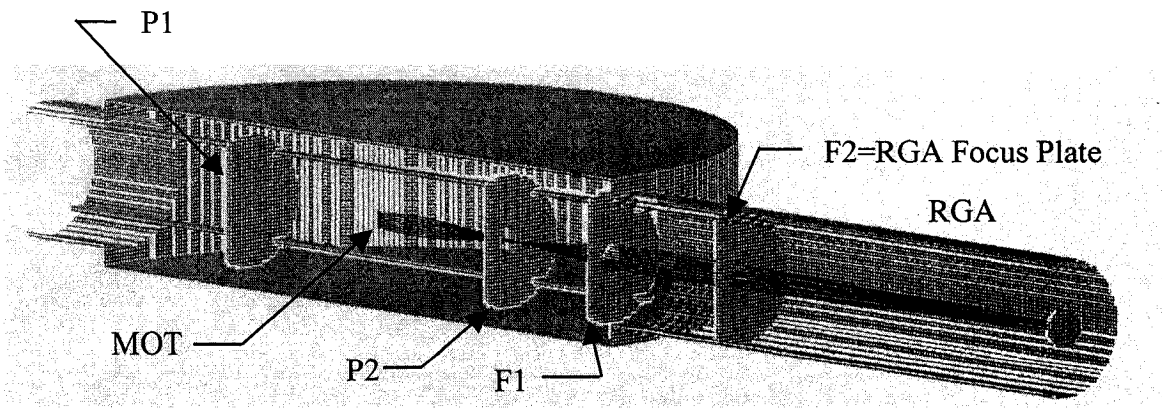

FIG. 6.4. SIMION 3D ion optical simulation of a MOT chamber. The MOT is in the center producing ultracold ions; the ions are then being projected into an RGA. The F2 plate is the RGA focus plate.

The actual field plates were built out of stainless steel with ceramic washers insulating them against the holding rods that connected the assembly through a stainless steel flange with electrical feed-throughs. Each of the three plates of the assembly was connected to one of the feed-throughs by a stainless steel braided and grounded insulated wire (MDC #994100). The grounded insulated wires ensured that the ions would not deflect from their path of flight due to any external electric fields. The field plates were of circular ϕ25 mm stainless steel. Plate P1 was solid, while plates P2 and F1 had a hole of ϕ10 mm drilled in their center to allow passage of the ions. The holes were covered with a 44x44 Mesh/in, ϕ0.0055 in stainless steel grid, the grid had a 57.4% open area to allow for a more uniform electric field. The grid was spot welded to the field plates to minimize contamination of the vacuum system. The field plate assembly was initially

tested with a CEM mounted behind it for rough tuning and testing, Fig. 6.5. After a satisfactory test the CEM was replaced with the SRS RGA200 and the system was fine-tuned. The resulting field plate voltages and the spacing between the plates are listed in Table 6.1, while the inserted picture shows the actual field plate assembly with feed-through flange.

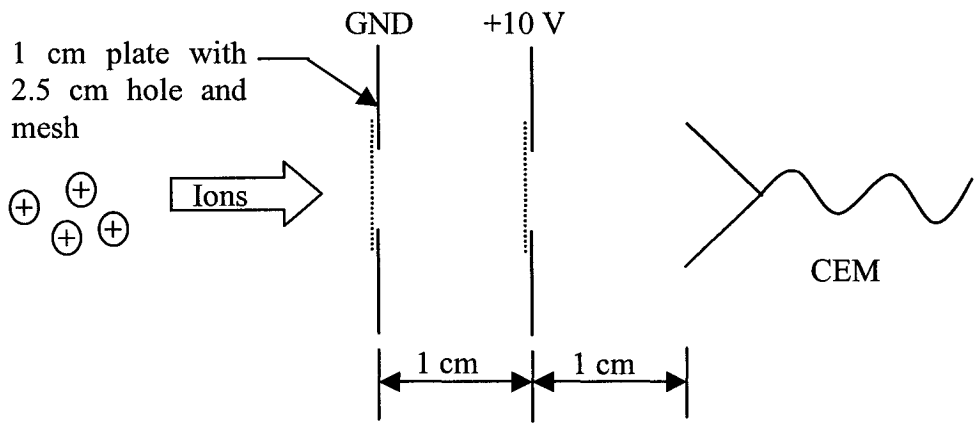

FIG. 6.5. CEM test assembly used to rough tune the field plate assembly. The CEM field plates were made out of the same material and in the same fashion as for the field plate assembly described in the text.

The angular dependence of the MOT could not be experimentally analyzed because of the physical constraints of the electric field plates. It is assumed that the trap is not isotropic due to polarization effects. Simulations with SIMION predict that ions emitted with greater than 1 eV at an angle of 30° or greater to the axis of the ion optics will not make it through the holes. Since for ultracold temperatures the ions produced by

the MOT should have an energy near 0 eV, most ions should be collected by the MOT. SIMION also predicts that at the MOT the electric field is 1 V/mm, and that the electric field cannot in general be assumed uniform between the plates. Table 6.1 showed that the plate spacing between P1 and P2 is 100 mm, and the MOT chamber is only 60 mm wide in the center and is grounded. For the electric field to be uniform the spacing of the ion optics plates would have to be less than 30 mm, which is physically not viable due to laser beam blocking. It is expected that in the future the angular dependence of the ion production will be studied.

TABLE 6.1. Field plate assembly voltages and spacing distances used to obtain PI and AI ionization rates.

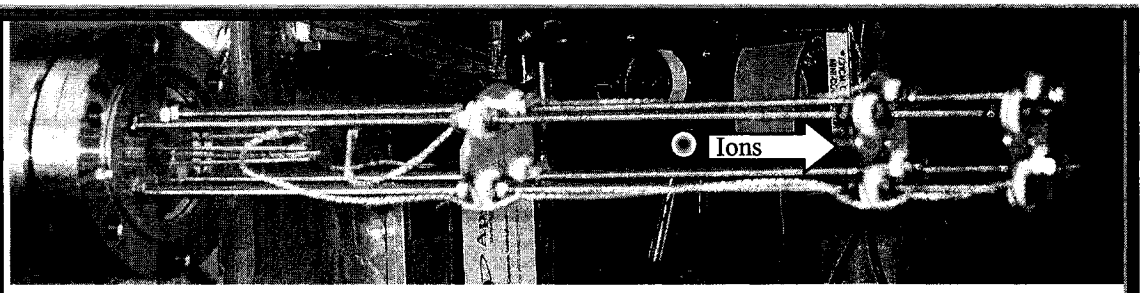

P1	1600 V	Distance between P1&P2	100 mm
P2	-200 V	Distance from P1 to MOT	50 mm
F1	-130 V	Distance from P2 to F1	40 mm
F2(RGA)	-150 V	Distance from F1 to F2(RGA)	50 mm

6.2 IONIZATION RESULTS FOR AN AR* AND A RB-AR* MOT

The first experimental study done with the SRS RGA 200 was to analyze the relative PI/AI rate in Ar*. To obtain the results a software program issued with the RGA 200 from SRS could be used or a specially modified LabView program written for the RGA 200 by SRS could also be employed. The programs allowed for the taking of data in an analog mode or in a histogram mode. The analog mode was used during the systems start up and the systems checking and optimization, while the histogram mode was used for data taking. The histogram would automatically bin the data points per amu for each scan making it a more useful tool for obtaining ion counts per amu.

In analog mode the scan x-axis represents the mass range selected while the y-axis shows the ion current of every mass measured, where the area under each peak represents the ion counts. The scan proceeds at a set scan range from the starting and ending amu selected. Fig. 6.6 shows such a scan to detect Ar^+ and Ar_2^+ ions that are expelled from an Ar* MOT.

In histogram mode the computer displays the individual mass amplitudes for the selected scan range. The RGA head performs a peak-lock for each mass and calculates one amplitude per mass, where the amplitude of the bar displayed represents the ion current measured for each mass. The RGA's histogram mode takes ten measurements per amu. A histogram scan for a dual MOT is shown in Fig. 6.7, where the larger peak is due to PI losses and the smaller peak is due to AI losses.

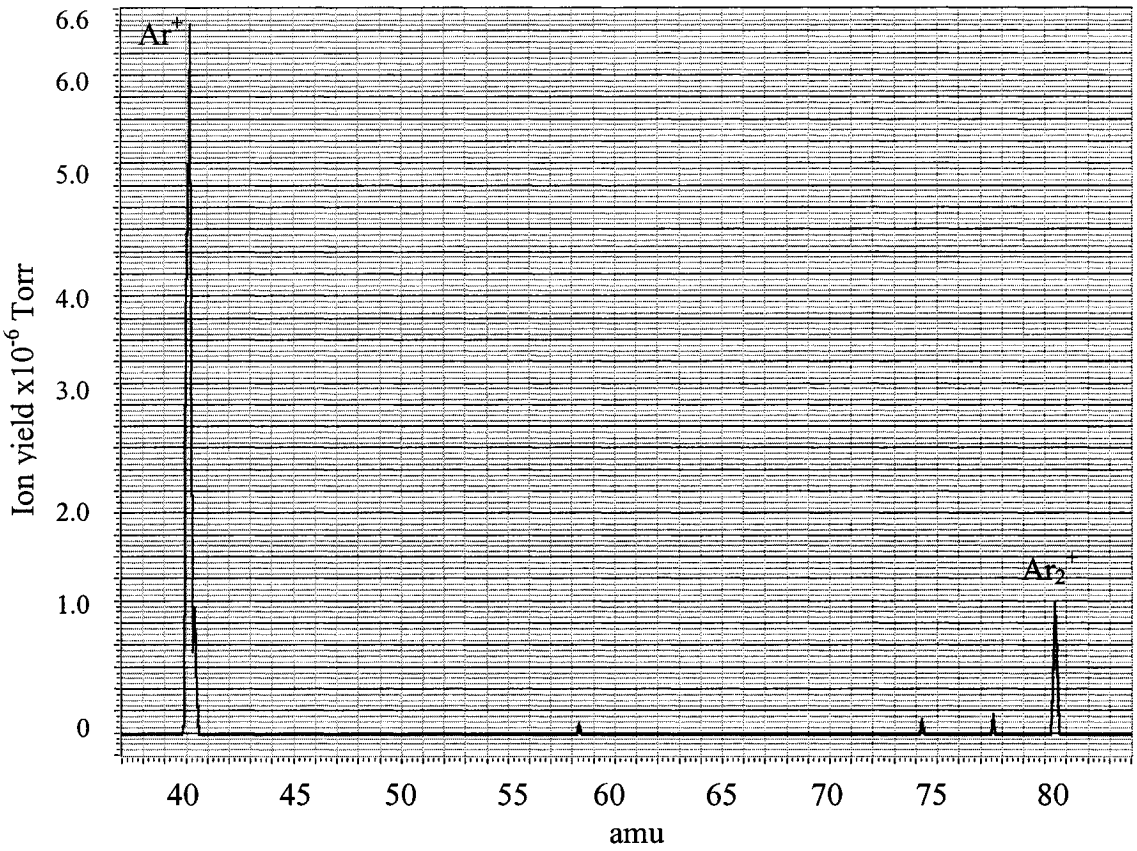

FIG. 6.6. An analog scan to detect ions produced by an Ar* MOT due to ultracold collisions. The first peak shows the PI production while the second smaller peak is the result of AI collisional loss from the MOT.

An analysis of the PI/AI ratio yields a factor of 6.7±3.6, which shows that the PI rate is on average six to seven times larger than the AI rate. This number was obtained by averaging 31 sets of data taken, the statistical error for this number was determined to be 50%. No comparative PI/AI ratio for Ar* exists for comparison at this time. The closest PI/AI ratio that is available is that given for Kr* by H. Katori et. al. [174], they estimated it to be about PI/AI≈10.

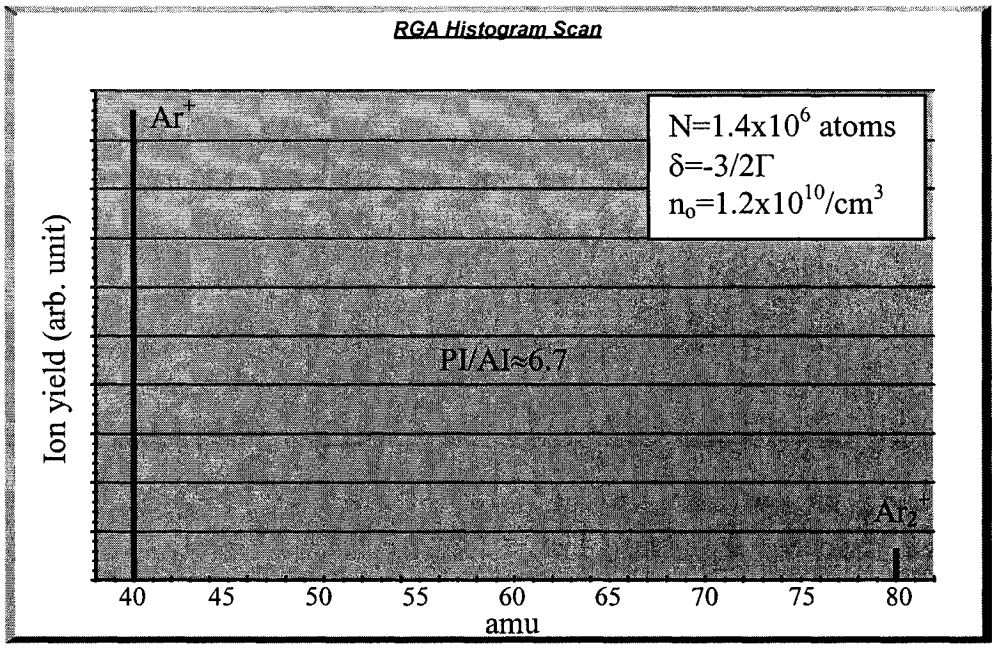

FIG. 6.7. RGA histogram scan of an Ar* MOT. The peaks show the respective PI and AI loss rates. The scale is linear.

For an Ar* MOT the primary loss mechanism is due to ionization losses, that has the two PI and AI channels, as was already discussed in Chapter 5. Those collisions between two Ar* atoms can best be described by a resonant dipole-dipole interaction potential

$$V(r) = -\frac{C_n}{r^n} + \frac{\hbar^2 l(l+1)}{2\mu r^2}, \qquad (6\text{-}1)$$

where μ is the reduced mass, $\hbar$ is the Plank constant, C_n is a dispersion coefficient, l is the angular momentum, r is the inter-nuclear distance, and n is a constant dependent on the character of the collision. For sufficiently low energy a partial s-wave scattering can always take place, therefore l=0 and n=3 is a long-range resonant dipole-dipole

interaction if the atoms collide in the S-P state. When no light is present and all the atoms are in the ground state the collisions will take place in the S-S state which is a van der Waals interaction, with n=6. In the Ar* MOT 45% of the atoms are in the excited P state, the remainder reside in the S ground state. The MOT yields an estimated $400x10^3$ count/sec of ions as measured with the CEM, since during each PI or AI interaction two atoms are lost this gives an approximate loss rate of $\approx 800x10^3$ atoms/sec from the MOT. Comparing this with the MOT loss rate of $\beta_{Ar} n_0 N_{Ar} / 2^{3/2} \approx 1.6x10^6 atoms/\sec$, this shows that about half the ions are detected by the CEM. Since about 67% of this loss is due to PI this is the dominant ionization loss channel.

When looking at the Rb-Ar* collisional interaction no such results could be observed, Fig. 6.8. A possible explanation is that this can be attributed to the fact that most of the atoms are lost due to radiative escape instead of a PI or AI ionization loss channel or detection sensitivity. Since for a heteronuclear reaction Eq. (6-1) can be rewritten with n=6 and l=0,

$$V(r) = -\frac{C_6}{r^6}. \qquad (6\text{-}2)$$

This interaction is a much shorter range van der Waals interaction. During a heteronuclear collision at long range the acceleration of the atoms toward the origin could be much less than for its homonuclear counter part. In that case the arrival time of the atom at the origin would be longer than the excited state lifetime and thus the survivability of the atoms to PI or AI would be drastically reduced. For PI and AI to take place the atoms have to be close ranged to each other.

No matter what the loss mechanism may be a limit can be set on the amount of

ions produced in a dual species RbAr* MOT. This can be estimated by assuming that only 1% of the ions make it through the quadrupole mass filter to the faraday cup [196]. This would mean that roughly 8000 ion/s Ar ions should arrive at the faraday cup, and from those 8000 approximately 2500 ion/s should be due to AI (Ar_2^+) for Ar (this is the smaller peak in Fig. 6.8). Considering the dual species loss rate and assuming that all Rb atoms get converted to ions with approximately the same ratio of PI/AI as that for Ar, about 1500 ions/s Rb^+ (PI) should arrive at the Faraday cup. This peak should be the PI rate for the heteronuclear ionization and should be next to the Ar_2^+ peak in Fig 6.8. Since no peak is present in Fig. 6.8 it can be estimated that the total dual MOT RbAr ion production is much less than 2500 ion/s.

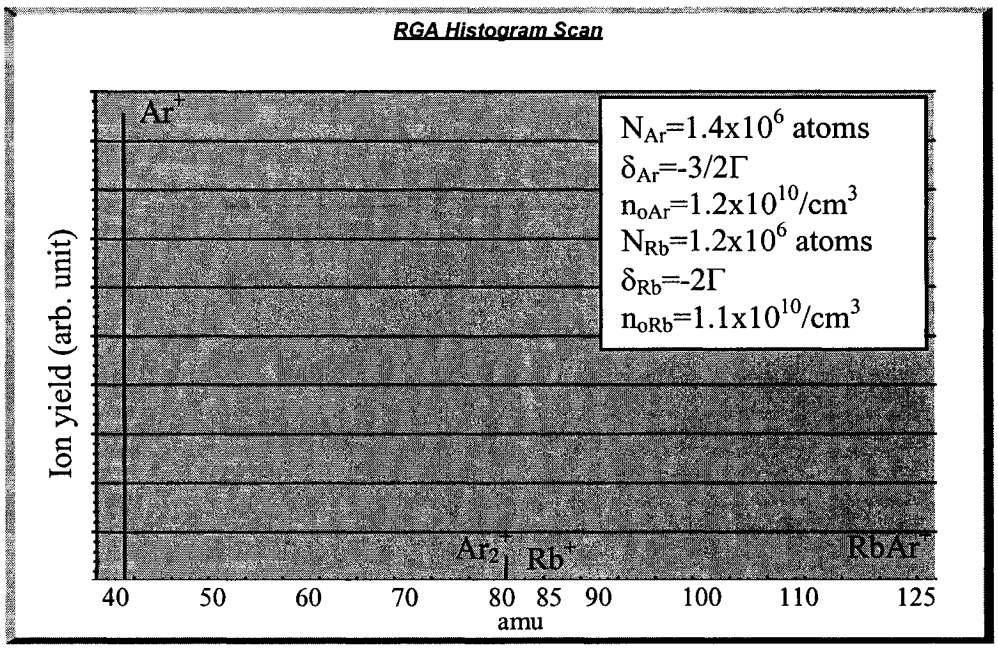

FIG. 6.8. A histogram scan shows no indication of Rb^+ and $RbAr^+$.

When considering the dual MOT loss rate coefficient, it can be written as a superposition of ionization loss and non-ionization losses as follows

$$\gamma_{Rb-Ar} = \gamma_I + \gamma_{NI}. \tag{6-3}$$

When assuming that ionization takes place, but it is just below the noise level, then a dual loss rate coefficient can be estimated to be of the order of $\gamma_I \approx 10^{-12} cm^3/s$. This would means that the majority of the dual trap loss is due to other losses rather than PI and AI. The results obtained with the RGA are still preliminary and future work has to be done to obtain conclusive evidence on the relative ion loss rate of Ar and the dual species MOT. Nevertheless, the new and exciting ability of the RGA and the ion optics to distinguish between different atomic species in a MOT will assist in this work tremendously.

CHAPTER VII

FUTURE DUAL MOT EXPERIMENTS

The development of the first dual species MOT now opens the possibility for a number of new experiments and improvements. The MOT that was built for the experiments described in this thesis is primarily a prototype and a lot of experience was gained in building and using it. Therefore, to conduct any number of further experiments with the dual MOT, ongoing improvements need to be made first to accommodate experimental requirements.

One of the first improvements should be the building of a designated Ar* beam line. This would include a source, as was used in this experiment, a beam bending mechanism, an optical compressor, and a Zeeman slower. The beam bending mechanism as described in Chapter 3 would separate the metastable atoms from any other atoms and ions, this would drastically reduce the MOT's background pressure. The result would be a decrease in the linear loss rate coefficient α and an increase in MOT sizes. An optical compressor could be used to make a more intense beam and prevent metastable loss due to ion radial spread. An optical compressor could be located either before or after the Zeeman slower, or possibly even both ends when needed. Of useful help would also be the switching from a Ti:sapphire laser source to diodes. One master laser could then run several slave lasers with added stability, only having to lock to one laser. Additional refinements can also be made to the RGA/ion optical setup, to obtain a relative ion count

and to extract a dual MOT Rb-Ar signal.

With added MOT stability future work could include optical shielding experiments, photoassociation and production of the RbAr molecule, building of a FORT, and especially continued work on the collisional rate loss constants obtained in this thesis. With a larger laser intensity and a stronger dual MOT an intensity dependence on loss rate coefficient could be obtained. Furthermore, experiments with a FORT could be one way to add more insight into the collisional loss rate dependence on ground and excited state collisions. The confining of molecules in a FORT after formation might also be a possibility and would add new and exciting information on the RbAr complex. The work of the dual MOT does not have to be limited to Rb-Ar*. Rb-Kr* for example, could be used as well since it has similar characteristics as Ar*. Kr* has a trapping transition near Ar* at 811 nm and it could be possible to use the same laser for this task. The work presented here is only the starting point for many innovative experiments waiting to take place.

CHAPTER VIII

CONCLUSION

The first dual species MOT was constructed and was successful at confining simultaneously $1.2x10^6$ ^{85}Rb atoms at a density of $1x10^{10}/cm^3$ with $1.4x10^6$ ^{40}Ar* atoms at a density of $1.2x10^{10}/cm^3$. This resulted in an interaction, which yielded an interspecies loss rate coefficient of $\gamma_{Rb-Ar} = (4.8 \pm 1.6)x10^{-11} cm^3/s$. This loss corresponds to a 3% reduction of ^{85}Rb atoms when the ^{40}Ar* trap was loaded spatially overlapped with the ^{85}Rb trap. The main loss mechanisms for the dual species trap are either PI-AI or of the radiative escape type. For a sole Ar* MOT the main loss mechanism were Penning and associative ionization, showing an interaction ratio of PI/AI=6.7±3.6. Making the Penning ionization channel the main loss channel.

To construct this dual species MOT a diode laser was used for the ^{85}Rb, which was trapped in the form of a vapor in the MOT region. The ^{40}Ar* was trapped with a Ti:sapphire laser, which was also used to slow the atoms in a beam with a Zeeman slower. The Ti:sapphire laser was specifically modified to run within 1 MHz of natural linewidth of the atoms transition, this allowed for establishing a stable Ar* MOT. Since laser sources are only available at a wavelength where the ^{40}Ar* cooling transition is in its metastable state, an rf cavity resonator is needed to excite the atoms to that state. Due to its excitation the atoms would leave the resonator at too high a velocity to be trapped, therefore a Zeeman slower was built to slow them down to a trap capture velocity. To

obtain ionization results a Stanford Research Systems residual gas analyzer (SRS RGA200) was modified to work with an ion optical field plate assembly to collect ions expelled from the MOT. The RGA200's quadrupole mass spectrometer was used to collect and scan for ions within 1 amu, more than sufficient to distinguish between PI and AI rates.

The ability to confine two species from opposite sides of the periodic table opens the door for the production and study of ultracold molecules with a weak van der Waals interaction potential. The capability to cool two species simultaneous can also lead to sympathetic cooling of one species of atoms with another leading to Bose-Einstein condensates. In particular the ability to trap the Rb-Ar complex can also show the way to an Rb-Kr trap or even a Ar-Kr trap. None of these ultracold interactions has as of yet any theoretical interaction loss rate constant for comparison.

REFERENCES

[1] E. Raab, M. Prentiss, A. Cable, S. Chu, and D. E. Pritchard, "Trapping of neutral sodium atoms with radiation pressure," Phys. Rev. Lett. **59**, 2631 (1987).

[2] S. Chu, "The manipulation of neutral particles," Rev. Mod. Phys. **70**, 685 (1998).

[3] C. N. Cohen-Tannoudji, "Manipulating atoms with photons," Rev. Mod. Phys. **70**, 707 (1998).

[4] W. D. Phillips, "Laser cooling and trapping of neutral atoms," Rev. Mod. Phys. **70**, 721 (1998).

[5] J. Weiner, V. S. Bagnato, S. Zilio, and Paul S. Julienne, "Experiments and theory in cold and ultracold collisions," Rev. Mod. Phys., Vol. **71**, 1 (1999).

[6] P. D. Lett, P. S. Julienne, and W. D. Phillips, "Photoassociative spectroscopy of laser cooled atoms," Ann. Rev. Phys. Chem. **46**, 423 (1996).

[7] R. Guckert, X. Zhao, S. G. Crane, A. Hime, W. A. Taylor, D. Tupa, D. J. Vieira, and H. Wollnik, "Magneto-optical trapping of radioactive ^{82}Rb atoms," Phys. Rev. A **58**, 1637 (1998).

[8] C. S. Wood, S. C. Bennet, D. Cho, B. P. Masterson, J. L. Roberts, C. E. Tanner, and C. E. Wieman, "Measurement of Parity Nonconservation and an Anapole Moment in Cesium," Science **275**, 1759 (1997).

[9] M. H. Anderson, J. R. Ensher, M. R. Matthews, C. E. Wieman, and E. A. Cornell, "Observation of Bose-Einstein condensation in a dilute atomic vapor" Science **269**, 198 (1995).

[10] C. C. Bradley, C. A. Sackett, J. J. Tollett, and R. G. Hulet, "Evidence of Bose-Einstein Condensation in an Atomic Gas with Attractive Interactions," Phys. Rev. Lett. **75**, 1687 (1995).

[11] K. B. Davis, M.-O. Mewes, M. R. Andrews, N. J. van Druten, D. S. Durfee, D. M. Kurn, and W. Ketterle, "Bose-Einstein condensation in a gas of sodium atoms" Phys. Rev. Lett. **75**, 3969 (1995).

[12] A. Fioretti, D. Comparat, A. Crubellier, O. Dulieu, F. Masnou-Seeuws, and P. Pillet, "Formation of Cold Cs_2 Molecules through Photoassociation," Phys. Rev. Lett. **80**, 4402 (1998).

[13] T. Takekoshi, B. M. Patterson, and R. J. Knize, "Observation of Optically Trapped Cold Cesium Molecules," Phys. Rev. Lett. **81**, 5105 (1998).

[14] A. N. Nikolov, E. E. Eyler, X. Wang, H. Wang, J. Li, W. S. Stwalley, and P. L. Gould, "Observation of Ultracold Ground-State potassium Molecules," Phys. Rev. Lett. **82**, 703 (1999).

[15] C. Gabbanini, A. Fioretti, A. Lucchesini, S. Gozzini, and M. Mazzoni, "Cold Rubidium Molecules Formed in a Magneto-Optical Trap," Phys. Rev. Lett. **84**, 2814 (2000).

[16] J. P. Shaffer, W. Chalupczak, and N. P. Bigelow, "Photoassociative Ionization of Heteronuclear Molecules in a Novel Two-Species Magneto-optical Trap," Phys. Rev. Lett. **82**, 1124 (1999).

[17] C. I. Sukenik and H. C. Busch, "Simultaneous trapping of rubidium and metastable argon in a magneto-optical trap," Phys. Rev. A **66**, 051402 (2002).

[18] K. Gibble and S. Chu, "Future Slow-Atom Frequencey Standards," Metrologia **29**, 201 (1992).

[19] Ph. Laurent, P. Lemonde, E. Siomon, G. Santorelli, A. Clarion, N. Dimarcq, P. Petit, C. Audoin, and C. Salomon, "A Cold Atom Clock in the absence of gravety," Eur. Phys. J. D **3**, 201 (1998).

[20] W. R. Anderson, C. C. Bradley, J. J. McClelland, and R. J. Celotta, "Minimizing Feature Width in Atom Optically Fabricated Chromium Nanostructures," Phys. Rev. A **59**, 2476 (1999).

[21] M. O.- Mewes, M. R. Andrewa, D. M. Kurn, D. S. durfee, C. G. Townsend, and W. Ketterle, "Output Coupler for Bose-Einstein Condensed Atoms," Phys. Rev. Lett. **78**, 582 (1997).

[22] H. J. Metcalf, and P. van der Straten, "Laser Cooling and Trapping," Springer-Verlag (1999).

[23] D. DeMille, "Quantum computation with trapped polar molecules," Phys. Rev. Lett. **88**, 067901 (2002).

[24] D. Zimmerman, "Laser spectroscopic investigation of alkali-rare gas van der Waals molecules," Tren. In Chem. Phys. **1**, 391 (1991).

[25] C. J. Lee, "Rotationally Resolved Laser Spectroscopy of the $3s^2\Sigma^+ \leftarrow 2p^2\Pi$ transition in $^6Li^{20}Ne$ and $^7Li^{20}Ne$ van der Waals Molecules," Ph.D. Thesis, Old Dominion University (1991).

[26] G. Moe, A. C. Tam, and W. Happer, "Absorbtion Studies of Excimer Transitions in Cs-Noble-gas and Rb-Noble-gas Molecules," Phys. Rev. A **14**, 349 (1976).

[27] R. Grainer, G. Charton, and J. Grainer, "Theoretical and Experimental Studies of the Interatomic Spectrum Induced in the Mixture Rb-Xe," J. Quant. Spectr. Radiat. Transfer **18**, 637 (1977).

[28] I. Doubourg, M. Ferray, J. P. Visticot, and B. Sayer, "Experimental Investigation of the Rb (6S or 4D) Interaction: Determination of Interaction Potentials and Oscillator Strengths," J. Phys. B: At. Mol. Opt. Phys. **19**, 1165 (1986).

[29] D. L. Drumond and A. Gallagher, "Potentials and Continiuum Spectra of Rb-Noble gas molecules," J. Chem. Phys. **60**, 3426 (1974).

[30] M. V. Romalis, E. Miron, and G. D. Cates, "Pressure Broadening of Rb D_1 and D_2 Lines by ^{3}He, ^{4}He, N_2, and Xe: Line Cores and Near Wings," Phys. Rev. A **56**, 4569 (1997).

[31] B. Bussery, Y. Achkar and M. Aubert-Frécon, "Long-range molecular states dissociating to the three or four lowest asymptotes for the ten heteronuclear alkali molecules," Chem. Phys. **116**, 319 (1987).

[32] C. Linton, F. Martin, I. Russier, A. J. Ross, P. Crozet, S. Churassy, and R. Bacis, "Observation and Analysis of the $A^1\Sigma_u^+$ State of $^6Li_2$ from υ=0 the Dissociation Limit," J. Mol. Spec. **175**, 340 (1996).

[33] E. J. Bedford, and F. Engelke, "Laser-induced fluorescence in supersonic nozzle beams: predissociation in the Rb_2 C $^1\Pi_u$ and D $^1\Pi_u$ states," Chem. Phys. Lett. **75**, 132 (1980).

[34] G. Igel-Mann, U. Wedig, P. Fuentealba, and H. Stoll, "Ground-state properties of alkali dimers XY (X, Y=Li to Cs)," J. Chem. Phys. **84**, 5007 (1986).

[35] I. Kovács, "Rotational Structure in the Spectra of Diatomic Molecules," Adam Hilger LTD London (1969).

[36] G. Herzberg, "Spectra of Diatomic Molecules," 2nd ed. Van Nostrand, Reinhold and Co. New York (1950).

[37] J. Pascale, and J. Vandepanque, "Excited Molecular Terms of the Alkali-Rare Gas Atom Pairs," J. Chem. Phys. **60**, 2278 (1974).

[38] J. Pascale, "Oscillator Strengths for S-S and S-D Induced Dipole Transitions in Alkali-Rare Gas Systems," J. Chem. Phys. **67**, 204 (1977).

[39] T. G. Walker, "Estimates of Spin-Exchange Parameters for Alkali-metal-Noble-gas Pairs," Phys. Rev. A **40**, 4959 (1989).

[40] S. H. Patil, "Adiabatic Potentials for the Alkali-Inert Gas Systems in the Ground State," J. Chem. Phys. **94**, 8089 (1991).

[41] J. T. Bahns, P. L. Gould, and W. C. Stwalley, "Formation of cold molecules," Advan. At. Mol. Opt. Phys. **42**, 171 (2000).

[42] W. C. Stwalley and H. Wang, "Photoassociation of Ultracold Atoms: A New Spectroscopic Technique," J. Mol. Spec. **195**, 194 (1999).

[43] A. P. Mosk, M. W. Reynolds, and T. W. Hijmans, "Photoassociation of Spin-Polarized Hydrogen," Phys. Rev. Lett. **82**, 307 (1999).

[44] E. R. I. Abraham, W. I. McAlexander, C. A. Sackett, and R. G. Hulet, "Spectroscopic Determination of the s- Wave Scattering Length of Lithium," Phys. Rev. Lett. **74**, 1315 (1995).

[45] W. I. McAlexander, E. R. I. Abraham, N. W. M. Ritchie, C. J. Williams, H. T. C. Stoof, and R. G. Hulet, "Precise atomic radiative lifetime via photoassociation spectroscopy of ultracold lithium," Phys. Rev. A **51**, 871 (1995).

[46] E. R. I. Abraham, N. W. M. Ritchie, W. I. McAlexander, and R. G. Hulet, "Photoassociative spectroscopy of long-range states of ultracold $^6Li_2$ and $^7Li_2$," J. Chem. Phys. **103**, 7773 (1995).

[47] U. Schlöder, C. Silber, and C. Zimmermann, "Photoassociation of heteronuclear lithium," Appl. Phys. B **73**, 801 (2001).

[48] P. L. Gould, P. D. Lett, P. S. Julienne, and W. D. Phillips, "Observation of Associative Ionization of Ultracold Laser-Trapped Sodium Atoms," Phys. Rev. Lett. **60**, 788 (1988).

[49] M. E. Wagshul, K. Helmerson, P. D. Lett, S. L. Rolston, and W. D. Phillips, "Hyperfine Effects on Associative ionization of Ultracold Sodium," Phys. Rev. Lett. **70**, 2074 (1993).

[50] K. M. Jones, P. S. Julienne, P. D. Lett, W. D. Phillips, and E. C. J. Williams, "Measurement of the atomic Na(3P) lifetime and of retardation in the interaction between two atoms bound in a molecule," Euro. Phys. Lett. **35**, 85 (1996).

[51] V. Bagnato, L. Marcassa, C. Taso, Y. Wang, and J. Weiner, "Two-Color Spectroscopy of Colliding Ultracold Atoms," Phys. Rev. Lett. **70**, 3225 (1993).

[52] V. Bagnato, L. Marcassa, Y. Wang, J. Weiner, P. S. Julienne, and Y. B. Band, "Ultracold photoassociative ionization collisions in a magneto-optical trap: The optical-field-intensity dependence in a radiative dissipative environment," Phys. Rev. A **48**, 2523 (1993).

[53] P. D. Lett, K. Helmerson, W. D. Phillips, L. P. Ratcliff, S. L. Rolston, and M. E. Wagshul, "Spectroscopy of Na_2 by photoassociation of Laser-Cooled Na," Phys. Rev. Lett. **71**, 2200 (1993).

[54] L. P. Ratliff, M. E. Wagshul, P. D. Leti, S. L. Rolston, and W. D. Phillips, "Photoassociative spectroscopy of 1_g, 0_u^+, and 0_g^- states of Na_2," J. Chem. Phys. **101**, 2638 (1994).

[55] E. Tiesinga, C. J. Williams, P. S. Julienne, K. M. Jones, P. D. Lett, and W. D. Phillips, "A Spectroscopic Determination of Scattering Lengths for Sodium Atom Collisions," J. Res. Natl. Inst. Stand. Technol. **101**, 505 (1996).

[56] P. A. Molenaar, P. van der Straten, and H. G. M. Heideman, "Long-Range Predissociation in Two-Color Photoassociation of Ultracold Na Atoms," Phys. Rev. Lett. **77**, 1460 (1996).

[57] K. M. Jonesy, S. Malekiz, L. P. Ratliff and P. D. Lett, "Two-colour photoassociation spectroscopy of ultracold sodium," J. Phys. B: At. Mol. Opt. Phys. **30**, 289 (1997).

[58] H. Wang, P. L. Gould, and W. C. Stwalley, "Photoassociative spectroscopy of ultracold ^{39}K atoms in a high-density vapor-cell magneto-optical trap," Phys. Rev. A **53**, 1216 (1996).

[59] H. Wang, P. L. Gould, and W. C. Stwalley, "Long-range interaction of the $^{39}K(4s)+^{139}K(4p)$ asymptote by photoassociative spectroscopy. I. The 0_g^- pure long-range state and the long-range potential constants," J. Chem. Phys. **106**, 7899 (1997).

[60] H. Wang, J. Li, X. T. Wang, C. J. Williams, P. L. Gould, and W. C. Stwalley, "Precise determination of the dipole matrix element and radiative lifetime of the ^{39}K 4p state by photoassociative spectroscopy," Phys. Rev. A **55**, 1569 (1997).

[61] H. Wang, X. T. Wang, P. L. Gould, and W. C. Stwalleyp, "Optical-Optical Double Resonance Photoassociative Spectroscopy of Ultracold ^{39}K Atoms near Highly Excited Asymptotes," Phys. Rev. Lett. **78**, 4173 (1997).

[62] X. Wang, H. Wang, P. L. Gould, and W. C. Stwalley, "Observation of the pure long-range 1_u state of an alkali-metal dimer by photoassociative spectroscopy," Phys. Rev. A **57**, 4600 (1998).

[63] A. N. Nikolov, E. E. Eyler, X. T. Wang, J. Li, H. Wang, W. C. Stwalley, and P. L. Gould, "Observation of Ultracold Ground-State Potassium Molecules," Phys. Rev. Lett. **82**, 703 (1999).

[64] A. N. Nikolov, J. R. Ensher, E. E. Eyler, H. Wang, W. C. Stwalley, and P. L. Gould, "Efficient Production of Ground-State Potassium Molecules at Sub-mK Temperatures by Two-Step Photoassociation," Phys. Rev. Lett. **84**, 246 (2000).

[65] J. D. Miller, R. A. Cline, and D. J. Heinzen, "Photoassociation Spectrum of Ultracold Rb Atoms," Phys. Rev. Lett. **71**, 2204 (1993).

[66] R. A. Cline, J. D. Miller, and D. J. Heinzen, "Study of Rb_2 Long-Range States of High-Resolution Photoassociation Spectroscopy," Phys. Rev. Lett. **73**, 632 (1994).

[67] J. R. Gardner, R. A. Cline, J. D. Miller, D. J. Heinzen, H. M. J. M. Boesten, and B. J. Verhaar, "Collisions of Doubly Spin-Polarized, Ultracold ^{85}Rb Atoms," Phys. Rev. Lett. **74**, 3764 (1995).

[68] H. M. J. M. Boesten,1 C. C. Tsai, B. J. Verhaar, and D. J. Heinzen, "Observation of a Shape Resonance in Cold-Atom Scattering by Pulsed Photoassociation," Phys. Rev. Lett. **77**, 5194 (1996).

[69] H. M. J. M. Boesten, C. C. Tsai, J. R. Gardner, D. J. Heinzen, and B. J. Verhaar, "Observation of a shape resonance in the collision of two cold ^{87}Rb atoms," Phys. Rev. A **55**, 636 (1997).

[70] C. C. Tsai, R. S. Freeland, J. M. Vogels, H. M. J. M. Boesten, B. J. Verhaar, and D. J. Heinzen, "Two-Color Photoassociation Spectroscopy of Ground State Rb_2," Phys. Rev. Lett. **79**, 1245 (1997).

[71] D. Leonard, and J. Weiner, "Direct two-color photoassociative ionization in a rubidium magneto-optic trap," Phys. Rev. A **52**, 4332 (1995).

[72] C. Gabbanini, A. Fioretti, A. Lucchesini, S. Gozzini, and M. Mazzoni, "Cold Rubidium Molecules Formed in a Magneto-Optical Trap," Phys. Rev. Lett. **84**, 2814 (2000).

[73] A. Fioretti, D. Comparat, A. Crubellier, O. Dulieu, F. Masnou-Seeuws, and P. Pillet, "Formation of Cold Cs_2 Molecules through Photoassociation," Lett. **80**, 4402 (1998).

[74] T. Takekoshi, B. M. Patterson, and R. J. Knize, "Observation of cold ground-state cesium molecules produced in a magneto-optical trap," Phys. Rev. A **59**, 5 (1999).

[75] D. Comparat, C. Drag, A. Fioretti, O. Dulieu, and P. Pillet, "Photoassociative Spectroscopy and Formation of Cold Molecules in Cold Cesium Vapor: Trap–Loss Spectrum versus Ion Spectrum," J. Mol. Spec. **195**, 229 (1999).

[76] C. M. Dion, C. Drag, O. Dulieu, B. Laburthe Tolra, F. Masnou-Seeuws, and P. Pillet, "Resonant Coupling in the Formation of Ultracold Ground State Molecules via Photoassociation," Phys. Rev. Lett. **86**, 2253 (2001).

[77] G. Zinner, T. Binnewies, and F. Riehle, "Photoassociation of Cold Ca Atoms," Phys. Rev. Lett. **85**, 2292 (2000).

[78] H. Wang, and W. C. Stwalley, "Ultracold photoassociative spectroscopy of heteronuclear alkali-metal diatomic molecules," J. Chem. Phys. **108**, 5767 (1998).

[79] N. Herschbach, P. J. J. Tol, W. Vassen, and W. Hogervorst, "Photoassociation Spectroscopy of Cold He(2^3S) Atoms," Phys. Rev. Lett. **84**, 1874 (2000).

[80] A. Gallagher, and D. E. Pritchard, "Exoergic Collisions of Cold Na*-Na," Phys. Rev. Lett. **63**, 957 (1989).

[81] P. S. Julienne, and J. Vigué, "Cold collisions of ground- and excited-state alkali-metal atoms," Phys. Rev. A **44**, 4464 (1991).

[82] P. S. Julienne, K-A Suominen, and Y. Band, "Complex-potential Model of Collisions of Laser-cooled Atoms," Phys. Rev. A **49**, 3890 (1994).

[83] P. Pillet, A. Chubellier, A. Bleton, O. Dulieu, P. Nosbaum, I. Mourachko, and F. Masnou-Seeuws, "Photoassociation in a Gas of Cold Alkali Atoms: I. Perturbative Quantum Approach" J. Phys. B. At. Mol. Opt. Phys. **30** 2801 (1997).

[84] K. A. Suominen, "Theories for Cold Atomic Collisions in light Fields," J. Phys. B. **29** 5981 (1996).

[85] P. S. Julienne, "Ultra-cold collisions of atoms and molecules," Scattering and Invese Scattering in Pure and Applied Science, Academic Press (2002).

[86] M. Marinescu, and H. R. Sadeghpour, "Long-range potentials for two-species alkali-metal atoms," Phys. Rev. A **59**, 390 (1999).

[87] R. Côté, A. Dalgarno, Y. Sun, and R. G. Hulet, "Photoabsorption by Ultracold Atoms and the Scattering Length," Phys. Rev. Lett. **74**, 3581 (1995).

[88] W. I. McAlexander, E. R. I. Abraham, and R. G. Hulet, "Radiative lifetime of the 2P state of lithium," Phys. Rev. A **54**, 5 (1996).

[89] R. Côté, and A. Dalgarno, "Mechanism for the production of vibrationally excited ultracold molecules of $^7Li_2$," Chem. Phys. Lett. **279** 50 (1997).

[90] H. R. Thorsheim, J. Weiner, and P. S. Julienne, "Laser-Induced Photoassociation of Ultracold Sodium Atoms," Phys. Rev. A **58**, 2420 (1987).

[91] Y. B. Band, and P. S. Julienne, "Ultracold-molecule production by laser-cooled atom Photoassociation," Phys. Rev. A **51**, 4317 (1995).

[92] S. J. Park, S. W. Suh, Y. S. Lee, and G.-H. Jeung, "Theoretical Study of the Electronic States of the Rb_2 Molecule," J. Mol. Spec. **207**, 129 (2001).

[93] A. J. Kerman, J. M. Sage, S. Sainis, T. Bergman, and D. DeMille, "Production of Ultracold, Polar RbCs* Molecules via Photoassociaiton," Phys. Rev. Lett. **92**, 033004 (2004).

[94] H. Wang, "Progress Towards Making Ultracold Heteronuclear RbCs Molecules via Photoassociation," Bull. Am. Phys. Soc. **48**, J1.025 (2003).

[95] P. S. Julienne, K. Burnett, Y. B. Band, and W. C. Stwalley, "Stimulated Raman molecule production in Bose-Einstein condensates," Phys. Rev. A **58**, 797 (1998).

[96] R. Wynar, R. S. Freeland, D. J. Han, C. Ryu, and D. J. Heinzen, "Molecules in a Bose-Einstein Condensate," Science **287**, 1016 (2000).

[97] J. Stenger, S. Inouye, M. R. Andrews, H.-J. Miesner, D. M. Stamper-Kurn, and W. Ketterle, "Strongly Enhanced Inelastic Collisions in a Bose-Einstein Condensate near Feshbach Resonances," Phys. Rev. Lett. **82**, 2422 (1999).

[98] S. J. J. M. F. Kokkelmans, H. M. J. Vissers, and B. J. Verhaar, "Formation of a Bose condensate of stable molecules via a Feshbach resonance," Phys. Rev. A **63**, 031601 (2001).

[99] K. Honda, Y. Takasu, T. Kuwamoto, M. Kumakura, Y. Takahashi, and T. Yabuzaki, "Optical dipole force trapping of a fermion-boson mixture of ytterbium isotopes," Phys. Rev. A **66**, 021401 (2001).

[100] G. Roati, F. Riboli, G. Modugno, and M. Inguscio, "Fermi-Bose Quantum Degenerate ^{40}K-^{87}Rb Mixture with Attractive Interaction," Phys. Rev. Lett. **89**, 150403 (2002).

[101] G. Modugno, M. Modugno, F. Riboli, G. Roati, and M. Inguscio, "Two Atomic Species Superfluid," Phys. Rev. Lett. **89**, 190404 (2002).

[102] G. Modugno, G. Roati, F. Riboli, F. Ferlaino, R. J. Brecha, and M. Inguscio, "Collapse of a Degenerate Fermi Gas," Science **297**, 2240 (2002).

[103] G. Modugno, G. Ferrari, G. Roati, R. J. Brecha, A. Simoni, and M. Inguscio, "Bose-Einstein Condensation of Potassium Atoms by Sympathetic Cooling," Science **294**, 1320 (2001).

[104] C. J. Myatt, E. A. Burt, R. W. Ghrist, E. A. Cornell, and C. E. Wieman, "Production of Two Overlapping Bose-Einstein Condensates by Sympathetic Cooling," Phys. Rev. Lett. **78**, 586 (1997).

[105] Z. Hadzibabic, C. A. Stan, K. Dieckmann, S. Gupta, M.W. Zwierlein, A. Görlitz, and W. Ketterle, "Two-Species Mixture of Quantum Degenerate Bose and Fermi Gases," Phys. Rev. Lett. **88**, 160401 (2002).

[106] F. Schreck, L. Khaykovich, K. L. Corwin, G. Ferrari, T. Bourdel, J. Cubizolles, and C. Salomon, "Quasipure Bose-Einstein Condensate Immersed in a Fermi Sea," Phys. Rev. Lett. **87**, 080403 (2001).

[107] A. G. Truscott, K. E. Strecker, W. I. McAlexander, G. B. Partridge, and Randall G. Hulet, "Observation of Fermi Pressure in a Gas of Trapped Atoms," Science **291**, 2570 (2001).

[108] H. Engler, I. Manek, U. Moslener, M. Nill, Yu.B. Ovchinnikov, U. Schlöder, U. Schünemann, M. Zielonkowski, M.Weidemüller, and R. Grimm, "Optical traps for quantum gases," Appl. Phys. B **67**, 709 (1998).

[109] M. -O. Mewes, G. Ferrari, F. Schreck, A. Sinatra, and C. Salomon, "Simultaneous magneto-optical trapping of two lithium isotopes," Phys. Rev. A **61**, 011403 (1999).

[110] F. Schreck, G. Ferrari, K. L. Corwin, J. Cubizolles, L. Khaykovich, M.-O. Mewes, and C. Salomon, "Sympathetic cooling of bosonic and fermionic lithium gases towards quantum degeneracy," Phys. Rev. A **64**, 011402 (2001).

[111] S. G. Crane, X. Zhao, W. Taylor, and D. J. Vieira, "Trapping an isotopic mixture of fermionic ^{84}Rb and bosonic ^{87}Rb atoms," Phys. Rev. A **62**, 011402 (2000).

[112] I. Bloch, M. Greiner, O. Mandel, T. W. Hänsch, and T. Esslinger, "Sympathetic cooling of ^{85}Rb and ^{87}Rb," Phys. Rev. A **64**, 021402 (2001).

[113] W. Stüptitz, G. Wokurka, F. Strauch, P. Kohns, and W. Ertmer, "Simultaneous cooling and trapping of ^{85}Rb and ^{87}Rb in a magneto-optical trap," Opt. Lett. **19**, 1571 (1994).

[114] T. Loftus, J. R. Bochinski, and T. W. Mossberg, "Simultaneous multi-isotope trapping of ytterbium," Phys. Rev. A **63**, 053401 (2001).

[115] V. Wippel, C. Binder, K. Rumpf, L. Windholz, "Interaction between Na and Li atoms in a two-species MOT," unpublished, l.windholz@iep.tu-graz.ac.at (2001).

[116] M. Mudrich, S. Kraft, K. Singer, R. Grimm, A. Mosk, and M. Weidemüller, "Sympathetic Cooling with Two Atomic Species in an Optical Trap," Phys. Rev. Lett. **88**, 253001 (2002).

[117] A. Mosk, S. Kraft, M. Mudrich, K. Singer, W. Wohlleben, R. Grimm, and M. Weidemüller, "Mixture of ultracold lithium and cesium atoms in an optical dipole trap," Appl. Phys. B **73**, 791 (2001).

[118] U. Schlöder, H. Engler, U. Schünemann, R. Grimm, and M. Weidemüller, "Cold inelastic collisions between lithium and cesium in a two-species magneto-optical trap," Eur. Phys. J. D **7**, 331 (1999).

[119] L. G. Marcassa, G. D. Telles, S. R. Muniz, and V. S. Bagnato, "Collisional losses in a K-Rb cold mixture," Phys. Rev. A **63**, 013413 (2000).

[120] M. S. Santos, P. Nussenzveig, A. Antunes, P. S. P. Cardona, and V. S. Bagnato, "Hyperfine-changing collision measurements in trap loss for mixed species in a magneto-optical trap," Phys. Rev. A **60**, 3892 (1999).

[121] M. S. Santos, P. Nussenzveig, L. G. Marcassa, K. Helmerson, J. Flemming, S. C. Zilio, and V. S. Bagnato, "Simultaneous trapping of two different species in a vapor-cell magneto-optical trap," Phys. Rev. A **52**, 4340 (1995).

[122] Y. E. Young, R. Ejnisman, J. P. Shaffer, and N. P. Bigelow, "Heteronuclear hyperfine-state-changing cold collisions," Phys. Rev. A **62**, 055403 (2000).

[123] G. D. Telles, L. G. Marcassa, S. R. Muniz, S. G. Miranda, A. Antunes, C. Westbrook, and V. S. Bagnato, "Inelastic cold collisions of a Na/Rb mixture in a magneto-optical trap," Phys. Rev. A **59**, 23 (1998).

[124] J. P. Shaffer, W. Chalupczak, and N. P. Bigelow, "Trap loss in a two-species Na-Cs magneto-optical trap: Intramultiplet mixing in heteronuclear ultracold collisions," Phys. Rev. A **60**, 3365 (1999).

[125] J. Goldwin, S. B. Papp, B. DeMarco, and D. S. Jin, "Two-species magneto-optical trap with ^{40}K and ^{87}Rb," Phys. Rev. A **65**, 021402 (2002).

[126] G. Ferrari, M. Inguscio, W. Jastrzebski, G. Modugno, G. Roati, and A. Simoni, "Collisional Properties of Ultracold K-Rb Mixtures," Phys. Rev. Lett. **89**, 053202 (2002).

[127] G. D. Telles, W. Garcia, L. G. Marcassa, V. S. Bagnato, D. Ciampini, M. Fazzi, J. H. Müller, D. Wilkowski, and E. Arimondo, "Trap loss in a two-species Rb-Cs magneto-optical trap," Phys. Rev. A **63**, 033406 (2001).

[128] I. Dubourg, M. Ferray, J. P. Visticot, and B. Sayer, "Experimental invetstigation of the Rb (6S or 4D) –rare gas interaction: determination of interaction potentials and oscillator strengths," J. Phys. B: At. Mol. Phys. **19**, 1165 (1986).

[129] M. G. Kozlov, and V. V. Yashchuk, "Estimate of P- and P, T-odd effects in diatomic van der Waals molecules," JETP Lett. **64**, 709 (1996).

[130] N. R. Newbury, and C. Wieman, " Resource Letter TNA-1: Trapping of neutral atoms," Am. J. Phys. **64**, 18 (1996).

[131] J. G. C. Tempelaars, "Trapping Metastable Neon Atoms," Ph.D. Thesis, Technische Universiteit Eidenhoven, (2001).

[132] M. S. Walhout, "Studdies of laser-cooled and magneto optically trapped xenon," Ph.D. Thesis, University of Maryland, (1994).

[133] C. Wieman, and G. Flowers, "Inexpensive laser cooling and trapping experiment for undergraduate laboratories," Am. J. Phys. **63**, 317 (1994).

[134] C. Savage "Introduction to Light Forces, Atom Cooling, and Atom Trapping," Aust. J. Phys. **49**, 745 (1996).

[135] R. Grimm, M. Weidemüller, and Y. Ovchinnikov, "Optical dipole traps for neutral atoms," Adv. in At. Mol. and Opt. Phys. **42**, 95 (2000).

[136] A. Aspect, E. Arimondo, R. Kaiser, N. Vansteenkiste, and C. Cohen-Tannoudji, "Laser Cooling below the One-Photon Recoil Energy by Velocity-Selective Coherent Population Trapping," Phys. Rev. Lett. **61**, 826 (1988).

[137] M. S. Shahriar, P. R. Hemmer, M. G. Prentiss, P. Marte, J. Mervis, D. P. Katz, N. P. Bigelow, and T. Cai, "Continuous polarization-gradient precooling-assisted velocity-selective coherent population trapping," Phys. Rev. A **48**, 4035 (1993).

[138] J. Kawanaka, M. Hagiuda, K. Shimizu, and H. Takuma, "Generation of an Intense Low-Velocity Metastable-Neon Atomic Beam," Appl. Phys. B **56**, 21 (1993).

[139] M. Jacka, J. Kelly, B. Lohmann, and S. Buckman, "Electron Collisions with Metastable Helium*," Aust. J. Phys. **49**, 515 (1996).

[140] W. Rooijakkers, W. Hogervorst, and W. Vassen, "An intense collimated beam of metastable helium atoms by two-dimensional laser cooling," Opt. Comm. **123**, 321 (1996).

[141] L. G. Meiners, and D. B. Alford, "Simple low-cost microwave plasma source," Rev. Sci. Instrum. **57**, 164 (1986).

[142] C. Y. Chen, K. Bailey, Y. M. Li, T. P. O'Conner, Z.-T. Lu, X. Du, L. Young, and G. Winkler, "Beam of metastable krypton atoms extracted from a rf-driven discharge," Rev. of Sci. Instrum. **72**, 271 (2001).

[143] W. W. Macapine, and R. O. Schildknecht, "Coaxial Resonators with Helical Inner Conductor," Proceedings of the IRE, 1959 (1959).

[144] W. D. Phillips and H. Metcalf, "Laser Deceleration of an Atomic Beam," Phys. Rev. Lett. **48**, 596 (1982).

[145] J. V. Prodan, W. D. Phillips and H. Metcalf, "Laser Production of a Very Slow Monoenergetic Atomic Beam," Phys. Rev. Lett. **49**, 1149 (1982).

[146] V. S. Bagnato, A. Aspect, and S. C. Zilio, "Study of a laser deceleration of an atomic beam by monitoring the fluorescence along the deceleration path," Opt. Comm. **72**, 76 (1989).

[147] T. E. Barrett, S. W. Dapore-Schwartz, M. D. Ray, and G. P. Lafyatis, "Slowing Atoms with σ^- Polarized Light," Phys. Rev. Lett. **67**, 3483 (1991).

[148] A. Witte, T. Kisters, F. Riehle, and J. Helmcke, "Laser cooling and deflection of a calcium atomic beam," J. Opt. Soc. Am. B **9**, 1030 (1992).

[149] P. A. Molenaar, P. van der Straten, H. G. M. Heideman, and H. Metcalf, "Diagnostic technique for Zeeman-compensated atomic beam slowing: technique and results," Phys. Rev. A **55**, 605 (1997).

[150] W. Rooijakkers, W. Hogervorst, and W. Vassen, "Laser deceleration and trapping of metastable helium atoms," Opt. Comm. **135**, 149 (1997).

[151] F. Lison, P. Schuh, D. Haubrich, and D. Meschede, "High-brilliance Zeeman-slowed cesium atomic beam," Phys. Rev. A **61**, 013405 (1999).

[152] U. D. Rapol, A. Wasan, and V. Natarajan, "Loading of a Rb magneto-optic trap from a getter source," Phys. Rev. A **64**, 023402 (2001).

[153] K. B. MacAdam, A. Steinbach, and C. Wieman, "A narrow-band tunable diode laser system with grating feedback, and a saturation absorption spectrometer for Cs and Rb," Am. J. Phys. **60**, 1098 (1992).

[154] A. S. Arnold, J. S. Wilson, and M. G. Boshier, "A simple extended-cavity diode laser," Rev. Sci. Instrum. **69**, 1236 (1998).

[155] R. T. Newell, "A Portable Magneto-Optical Trap," M.S. Thesis, University of Wisconsin-Madison, (1998).

[156] R. Kowalski, S. Root, S. D. Gensemer, and P. L. Gould, "A frequency-modulated injection-locked diode laser for two-frequency generation," Rev. Sci. Instrum. **72**, 2532 (2001).

[157] C. J. Myatt, N. R. Newbury, and C. E. Wieman, "Simplified atom trap by using direct microwave modulation of a diode laser," Opt. Lett. **18**, 649 (1993).

[158] P. Feng, and T. Walker, "Inexpensive diode laser microwave modulation for atom trapping," Am. J. Phys. **63**, 905 (1995).

[159] S. E. Park, H. S. Lee, T. Y. Kown, and H. Cho, "Dispersion-like signals in velocity-selective saturation-absorption spectroscopy," Opt. Commun. **192**, 49 (2001).

[160] K. L. Corwin, Z.-T. Lu, C. F. Hand, R. J. Epstein, and C. E. Wieman, "Frequency-stabilized diode laser with the Zeeman shift in an atomic vapor," Appl. Opt. **37**, 3295 (1998).

[161] C. I. Sukenik, H. C. Busch, and M. Shiddiq, "Modulation-free laser frequency stabilization and detuning," Opt. Comm. **203**, 133 (2002).

[162] D. W. Preston, "Doppler-free saturation absorption: Laser spectroscopy," Am. J. Phys. **64**, 1432 (1996).

[163] C. I. Sukenik, and H. C. Busch, "A rf discharge cell for saturation absorption spectroscopy of metastable argon," Rev. Sci. Instrum. **73**, 493 (2002).

[164] W. Vassen, C. Zimmerman, R. Kallenbach, and T. Hänsch, "A frequency-stabilized titanium sapphire laser for high-resolution spectroscopy," Opt. Comm. **75**, 435 (1990).

[165] M. W. Hamilton, "An introduction to stabilized lasers," Contemp. Phys. **30**, 21 (1989).

[166] J. R. Ensher, "The First Experiments with Bose-Einstein Condensation of ^{87}Rb," Ph.D. Thesis, University of Colorado at Boulder (1998).

[167] M. R. Matthews, "Two-Component Bose-Einstein Condensation," Ph.D. Thesis, University of Colorado at Boulder (1999).

[168] M. Mitsunaga, M. Yamashita, and H. Inoue, "Absorption imaging of electromagnetically induced transparency in cold sodium atoms," Phys. Rev. A **62**, 013817 (2000).

[169] D. Boiron, A. Michaud, J. M. Fournier, L. Simard, M. Sprenger, G. Grynberg, and C. Salmon, "Cold and dense cesium clouds in far detuned dipole traps," Phys. Rev. A **57**, 4106 (1998).

[170] B. P. Anderson, and M. A. Kasevich, "Spatial observation of Bose-Einstein condensation of ^{87}Rb in a confining potential," Phys. Rev. A **59**, 938 (1998).

[171] W. Ketterle, K. B. Davis, M. A. Joffe, A. Martin, and D. E. Pritchard, "High Densities of Cold Atoms in a Dark Spontaneous-Force Optical Trap," Phys. Rev. Lett. **70**, 2253 (1993).

[172] M. Walhout, U. Sterr, C. Orzel, M. Hoogerland, and S. L. Rolston, "Optical Control of Ultracold Collisions in Metastable Xenon," Phys. Rev. Lett. **74**, 506 (1995).

[173] H. Katori, H. Kunugita, and T Ido, "Quantum statistical effect on ionizing collisions of ultracold metastable Kr isotopes," Phys. Rev. A **52**, 4324 (1995).

[174] H. Katori, and S. Shimizu, "Laser-Induced Ionizing Collisions of Ultracold krypton Gas in the $1s_5$ Metastable State," Phys. Rev. Lett. **73**, 2555 (1994).

[175] F. Bardou, O. Emile, J. M. Courty, C. I. Westbrook, and A. Aspect, "Magneto-optical trapping of metastable helium: Collisions in the presence of resonant light," Europhys. Lett. **20**, 681-686 (1992).

[176] D. Hoffmann, P. Feng, R. S. Williamson III, and T. Walker, "Excited-State Collisions of Trapped ^{85}Rb Atoms," Phys. Rev. Lett. **69**, 753 (1992).

[177] T. Walker, D. Sesko, and C. Wieman,"Collective Behavior of Optically Trapped Neutral Atoms," Phys. Rev. Lett. **64**, 408 (1990).

[178] L. Marcassa, V. Bagnato, Y. Wang, C. Tsao, and J. Weiner, "Collisional losss rate in a magneto-optical trap for sodium atoms: Light-intensity dependence," Phys. Rev. A **47**, 4563 (1993).

[179] R. L. Cavasso-Filho, A. Scalabrin, D. Pereira, and F. C. Cruz, "Observing negligible collision trap losses: The case of alkaline-earth metals," Phys. Rev. A **67**, 021402 (2003).

[180] L.G. Marcassa, R.A.S. Zanon, S. Dutta, J. Weiner, O. Dulieu, and V.S. Bagnato, "Direct measurement of fine structure changing collisional losses in cold trapped ^{85}Rb," Eur. Phys. J. D **7**, 317 (1999).

[181] S. D. Gensemer, V. Sanchez-Villicana, K. Y. N. Tan, T. T. Grove, and P. L. Gould, "Trap-loss collisions of ^{85}Rb and ^{87}Rb: Dependence on trap parameters," Phys. Rev. A **56**, 4055 (1997).

[182] C. D. Wallace, T. P. Dinneen, K. –Y. N. Tan, T. T. Grove, and P. L. Gould, "Isotopic Difference in Trap Loss Collisions of Laser Cooled Rubidium Atoms," Phys. Rev. Lett. **69**, 897 (1992).

[183] D. Hoffmann, P. Feng, R. S. Williamson, III, and T. Walker, "Excited-State Collisions of Trapped ^{85}Rb Atoms," Phys. Rev. Lett. **69**, 753 (1992).

[184] H. Katori, and F. Shimizu, "Laser Cooling and Trapping of Argon and Krypton Using Diode Laser," Jpn. J. Appl. Phys. **29**, 2124 (1990).

[185] H. Katori, and F. Shimizu, "Lifetime measurement of the $1s_5$ Metastable State of Argon and Krypton with a Magneto-Optical Trap," Phys. Rev. Lett. **70**, 3545 (1992).

[186] H. C. Mastwijk, J. W. Thomsen, P. van der Straten, and A Niehaus, "Optical Collisions of Cold Metastable Helium Atoms," Phys. Rev. Lett. **80**, 5516 (1992).

[187] F. Shimizu, K. Shimizu, and H. Katori, "Laser cooling and trapping of Ne metastable atoms," Phys. Rev. A **39**, 2758 (1989).

[188] M. Walhout, H. J. L. Megens, A. Witte, and S. L. Rolston, "Magneto-optical trapping of metastable xenon: Isotope-shift measurements," Phys. Rev. A **48**, 879 (1993).

[189] Y. B. Band. And P. S. Yulienne, "Optical-Bloch-equation method for cold-atom collisions: Cs loss from optical traps," Phys. Rev. A **46**, 330-343 (1992).

[190] M. Pieksma, M. Cizek, J. W. Thomsen, P. van der Straten, and A. Niehaus, "Energy distributions of He^+ and He_2^+ ions formed in ultracold $He(2^3S_1)$+$He(2^3P_2)$ collisions," Phys. Rev. A **66**, 022703 (2002).

[191] G. Woestenenk, H. C. Mastwijk, J. W. Thomsen, P. van der Straten, M. Pieksma, M. van Rijnbach, and A. Niehaus, "Collisions between ultracold metastable He atoms," Phys. Res. B **154**, 194-203 (1999).

[192] H. C. Mastwijk, "Cold Collisions of Metastable Helium Atoms," Ph.D. Thesis, University of Utrecht (1997).

[193] H. C. Mastwijk, M. van Rijnbach, J. W. Thomsen, P. van der Straten, and A. Niehaus, "Photo induced collisions with laser cooled He* atoms," Eur. Phys. J. D **4**, 131-137 (1998).

[194] H. C. Mastwijk, J. W. Thomsen, P. van der Straten, and A. Niehaus, "Optical Collisions of Cold, Metastable Helium Atoms," Phys. Rev. Lett. **80**, 5516 (1998).

[195] Stanford Research Systems Residual Gas Analyzer (SRS RGA200) information and pictures can be found at www.thinksrs.com (2003).

[196] Personal communiqué and instruction on modifications to a RGA200 with G. A. Brucker, gab@thinksrs.com Stanford Research Systems technical support (2003).

[197] SIMION 7.0 "3D Ion Optics Software" by Ion Source Software is available at the following website www.srv.net/~klack/simion.html (2003).

APPENDIXES

A. OPTICAL BLOCH EQUATIONS

The Optical Bloch equations are defined as follows

$$\frac{d\rho_{gg}}{dt} = \Gamma\rho_{ee} + \frac{i}{2}\left(\Omega^*\tilde{\rho}_{eg} - \Omega\tilde{\rho}_{ge}\right) \tag{A-1}$$

$$\frac{d\rho_{ee}}{dt} = -\Gamma\rho_{ee} + \frac{i}{2}\left(\Omega\tilde{\rho}_{ge} - \Omega^*\tilde{\rho}_{eg}\right) \tag{A-2}$$

$$\frac{d\tilde{\rho}_{ge}}{dt} = -\left(\frac{\Gamma}{2} + i\delta\right)\tilde{\rho}_{ge} + \frac{i}{2}\Omega^*\left(\rho_{ee} - \rho_{gg}\right) \tag{A-3}$$

$$\frac{d\tilde{\rho}_{eg}}{dt} = -\left(\frac{\Gamma}{2} - i\delta\right)\tilde{\rho}_{eg} + \frac{i}{2}\Omega^*\left(\rho_{gg} - \rho_{ee}\right). \tag{A-4}$$

Where ρ_{ij} are the density matrix elements, Ω is the Rabi frequency as defined in the text by Eq. 2-6, and $\Gamma=1/\tau$ is the spontaneous decay rate or linewidth. The term $\tilde{\rho}_{ij} \equiv \rho_{ij}e^{i\delta t}$ where δ is the detuning [22].

VITA

2004	Naval Research Lab, Washington DC Postdoctoral position
2004-2000	Old Dominion University, Norfolk VA Physics Department
1999-1997	Naval Intelligence Officer, US Navy
1996	Evergreen Engineering, Eugene OR
1994-1900	University of Colorado, Boulder CO Aerospace Engineering Department
1990-1987	Gonzaga University, Spokane WA Mechanical Engineering